Alma Mater Studiorum · Università di Bologna

School of Science
Department of Physics and Astronomy
Master Degree Programme in Astrophysics and Cosmology

Very-High Energy γ-ray observations of the Geminga pulsar with the LST-1 of CTA

Graduation Thesis

Supervisor:
Prof. Cristian Vignali

Co-supervisors:
Dr. Roberta Zanin
Dr. Rubén López-Coto

Submitted by:
Giulia Brunelli

Academic Year 2022/2023
Graduation date II

"Stars!
Awareness turned over at the thought of all those stars above him – an infinite volume. A man must be half mad to imagine he could rule even a teardrop of that volume."

- Frank Herbert, *Dune Messiah*

Abstract

The Very-High Energy (VHE) range of γ rays has been inaccessible for many years because of the strict limitations of the operating instruments; thanks to the huge improvements in technology, we are finally able to properly explore the VHE universe. In this context, a key role was played by ground-based facilities, which are not as constrained as space telescopes are. Among them, noteworthy are the Imaging Atmospheric Cherenkov Telescopes (IACTs) that, since the first detection of the Crab Nebula at TeV energies in 1989, had proved the technique to be extremely efficient in searching for both Galactic and extragalactic VHE γ-ray sources. The current generation of these instruments includes MAGIC, H.E.S.S. and VERITAS, three arrays that have been operating for almost two decades and exponentially increasing the number of known sources over a short span of years. Nowadays, more than 250 sources populate the TeV sky, and the number is expected to rise with time thanks to the next-generation facility for ground-based γ-ray astronomy, the Cherenkov Telescope Array Observatory (CTAO), which will see its first light in a few years. The CTAO will consist of two arrays, one in the Northern Hemisphere with 13 telescopes and the other in the Southern one including 51 antennas, composed of IACTs with three different designs, allowing it to cover the wide energy range between 20 GeV and 300 TeV. The telescope design tailored for the lowest energy range is the largest one of the three, the Large-Sized Telescope (LST), with a 23-meter diameter; the first one of the Northern Array, dubbed LST-1, is already operative and has been taking sky data since 2019. LSTs can also be repointed to any direction in the sky within 20 seconds and this, along with their low-energy threshold, makes them excellent instruments for studying extragalactic sources, transients and pulsars.

Pulsars are amongst the most common Galactic sources of γ-ray emission: *Fermi*-LAT has detected more than 150 γ-ray pulsars since its launch in 2008. The detection of VHE emission from these compact objects was one of the most unexpected discoveries of the last few years. Up to now, only three pulsars (the Crab, the Vela, and Geminga) have been observed at these energies, and the mechanism responsible for the TeV emission is still unclear.

The object of study of this thesis is Geminga (PSR J0633+1746), the archetype of a middle-aged radio-quiet γ-ray pulsar. It has a period of 237 ms, a period derivative of $1.1{\cdot}10^{-14}$ s/s, a characteristic age of 300 ky and, with its distance lower than 300 pc, it is also one of the closest known pulsars to Earth. It was recognised as a γ-ray source since its first detection in 1972, but it was identified as a pulsar only twenty years later due to the absence of any kind of radio pulses. Its γ-ray light curve is characterised by the presence of two peaks, known as P1 and P2. In 2020, the MAGIC Collaboration detected Geminga above 15 GeV, making it the third VHE pulsar ever discovered by IACTs. This result is striking since we would not expect such energetic emission from

a middle-aged pulsar. With 80 hours of observations, they detected P2 at a significance of 6.3σ and found out the emission is best fitted by a power law. After performing a joint likelihood fit with the *Fermi*-LAT data, they ruled out both the power law with exponential and sub-exponential cut-off models, connected to the presence of curvature radiation, in favour of the simple power law, highlighting the possible presence of an Inverse Compton component.

Geminga was detected also by LST-1 at the end of 2022 and, for this thesis, 21 hours of LST-1 good-quality observations with a zenith cut at 25° were analysed. The results of this study were satisfying and compatible with those of MAGIC. The second peak of the light curve, P2, was detected at an 8σ significance, while the significance of the first one (P1) was 2σ. Then, a fit of P2 data with a power law spectral model was performed and the best-fit result was compatible with the one of MAGIC. A more complete analysis of the emission mechanism at the basis of the γ-ray emission required a joint likelihood fit of LST-1 and *Fermi*-LAT data at lower energies. The joint fit also included the MAGIC sample from the 2020 study. The final result allowed the rejection of the power law with an exponential cutoff model in favour of the power law with a sub-exponential cutoff, meaning that the classic models for the VHE γ-ray emission, the so-called Outer Gap models, cannot explain the VHE γ rays of Geminga. More complicated and modified versions of these models that locate the acceleration of particles even farther from the neutron star surface, hence preferring a softer sub-exponential cutoff rather than an exponential, are favoured, even though they still cannot fully explain the observations from $\sim$100s of MeV to $\sim$10s of GeV. These results highlighted the limitations of the present theories, which mainly rely on the assumption of curvature radiation, and the need for more observations and deeper studies to understand if additional mechanisms, such as the Inverse Compton scattering, are in place.

Moreover, what has been found proves that the LST-1 has excellent low-energy performance: with one-fourth of MAGIC's observation time and only one telescope, a stronger signal detection was obtained. This is a crucial result for the science verification of the instrument and of the Northern Array of CTAO, which will include four LSTs in total, since it shows that LSTs are truly able to consistently improve the performance of current-generation instruments and, in the near future, to increase the number of known VHE pulsars.

Contents

Chapter 1

Introduction to the Very High Energy γ-ray band

In 1989 the Whipple telescope detected the first source at TeV energies, the Crab Nebula [1], and paved the way for future Very High Energy γ-ray observations. In the following decades, studies in the VHE regime of γ-ray astronomy showed striking results and more advanced facilities were developed to detect new sources in the unexplored electromagnetic band. Nowadays, there has been a significant improvement in the technologies for the detection of VHE photons, even though the observations' statistics in the VHE band are still poor when compared to the data acquired in other spectral ranges at lower frequencies.

In this Chapter, introduction to the most important characteristics of the TeV domain is presented, including a brief description of the interaction of γ rays with the atmosphere, which is the basic concept at the basis of the development of ground-based facilities discussed in Chapter 2.

1.1 γ-ray astronomy

Table 1.1: Energy sub-bands of the γ-ray domain.

Name	**Energy range**
Low Energies (LE)	0.5 - 30 MeV
High Energies (HE)	30 MeV - 50 GeV
Very High Energies (VHE)	50 GeV - 100 TeV
Ultra High Energies (UHE)	100 TeV - 100 PeV
Extremely High Energies (EHE)	$>$ 100 PeV

The conventional "division line" between X-rays and γ rays is assumed to be the electrons' rest-frame energy, $E = m_e c^2 \simeq 0.5$ MeV, the minimum value for the energy of γ rays produced via electron-positron annihilation. Inside this broad window, one can define several sub-bands depending on the energy range (Table 1.1). Their limits are conventional, there is no strict division between the sub-ranges.

Due to the previous definition, radiation in the γ-ray band is always connected to non-thermal processes and the most important ones are listed in the following section.

1.1.1 Emission mechanisms for γ rays

γ-ray photons can be produced through several emission processes:

- **Synchrotron**

  Synchrotron radiation is emitted whenever an ultra-relativistic charged particle, such as an electron, interacts with a magnetic field that accelerates it. The spectrum of the emitted radiation is characterised by a fundamental quantity called the *critical frequency*

  $$\nu_C \propto \gamma^2 B \tag{1.1}$$

  where B is the magnetic field and γ the Lorentz factor of the particle[1]. This represents the frequency at which most of the emission occurs, and after reaching this value the spectrum tends to decay and become negligible. Even though the typical emission is observed in the radio band, synchrotron photons are important for the VHE range since they can be up-scattered through Inverse Compton in the process called Synchrotron Self Compton (see below).

  A particular kind of synchrotron radiation is **curvature radiation**, for which electrons emit radiation while moving along the curved magnetic field lines instead of following a helicoidal orbit. This mechanism is thought to be the basis of the γ-ray emission of pulsars (see Chapter 3).

- **Inverse Compton (IC) scattering**

  It is the process by which an ultra-relativistic electron interacts with a photon and transfers part of its energy to upscatter it at a much higher frequency. The maximum energy a photon of energy E can reach through IC scattering is

  $$E_{max} \propto 4\gamma^2 E \tag{1.2}$$

  where γ is the Lorentz factor of the electron. The computations required to obtain eq. (1.2) are reported in [2]. Depending on the origin of the photon field, Inverse Compton can be classified as external IC, if the photon field interacting with the

[1] $\gamma = (1-\beta^2)^{-1/2} = (1 - v^2/c^2)^{-1/2}$ where v is the velocity of the particle.

electrons is of external origin with respect to them, or Synchrotron Self-Compton (SSC), if electrons interact with the photons they previously emitted through synchrotron radiation. If electrons are sufficiently energetic, it is possible to obtain VHE γ-ray photons. Blazars are a typical environment where Inverse Compton emission is observed, see §1.3.

- **Neutral pion decay**

  Neutral pions π^0 can be produced when cosmic rays interact with atoms and molecules of the Interstellar Medium (ISM) through two important mechanisms: proton-proton (pp) collisions and interaction of protons with radiation fields (pγ)[2]. Pions have a short lifetime ($\tau = 1.78 \cdot 10^{-16}$ s) and they decay, for the vast majority of times, into two photons:

  $$\pi^0 \longrightarrow \gamma + \gamma$$

  If the primary pion is energetic enough, the products will be γ-ray photons. This phenomenon is particularly relevant for extensive air showers (see § 1.2).

- **Bremsstrahlung**

  It is a free-free emission process in which a charged particle gets deflected because of the interaction with an electric field. This is not usually relevant for the VHE emission since particles reach energies at most in the X-ray or LE γ-ray domain (in some cases even HE γ rays); however, if particles are deflected by Ultra-High Energy cosmic rays, emission in the VHE band could be produced.

1.2 Extensive atmospheric showers

When γ rays enter the atmosphere, they interact with matter via pair production generating pairs of electrons and positrons that in turn emit other photons via bremsstrahlung. In this way, the cascade of photons and electrons and positrons builds the electromagnetic extensive atmospheric (or air) shower. From its study and the modelling of its parameters, the primary photons' energy and position in the sky can be recovered.

The problem is that, at the same time when a γ-ray photon enters the atmosphere, a several orders of magnitude higher number of cosmic rays is entering and producing particle showers. In particular, among the products of hadronic showers, neutral pions decay into two γ-ray photons (as reported in § 1.1.1) that can start other electromagnetic showers. This means that there is always a significant background due to cosmic rays when studying γ rays indirectly through the showers they produce in the atmosphere.

In both cases, hadronic and electromagnetic, the cascade of particles produces a shower front travelling at the speed of light and lasting a few nanoseconds. However, the

[2] pp: $p + p \longrightarrow p + p + \pi^0$ pγ: $p + \gamma \longrightarrow p + \pi^0$

morphology of the shower and the produced particles are significantly different in the two cases (Figure 1.1). In general, hadronic showers show a more complex structure, not only do produce leptons and tend to be less collimated in the direction of the initiating hadron, mainly because of the different interaction mechanisms leading to particle generation. Another significant difference is related to the timing of the development of the showers: the electromagnetic ones tend to develop faster than the hadronic ones.

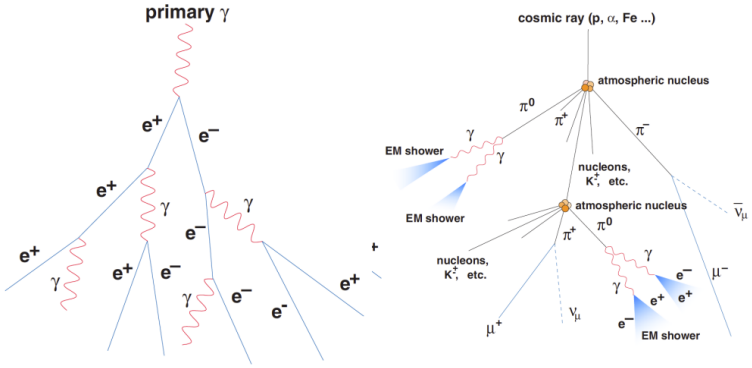

Figure 1.1: Schematic structure of an electromagnetic, on the left, and a hadronic shower, on the right. Taken from [3].

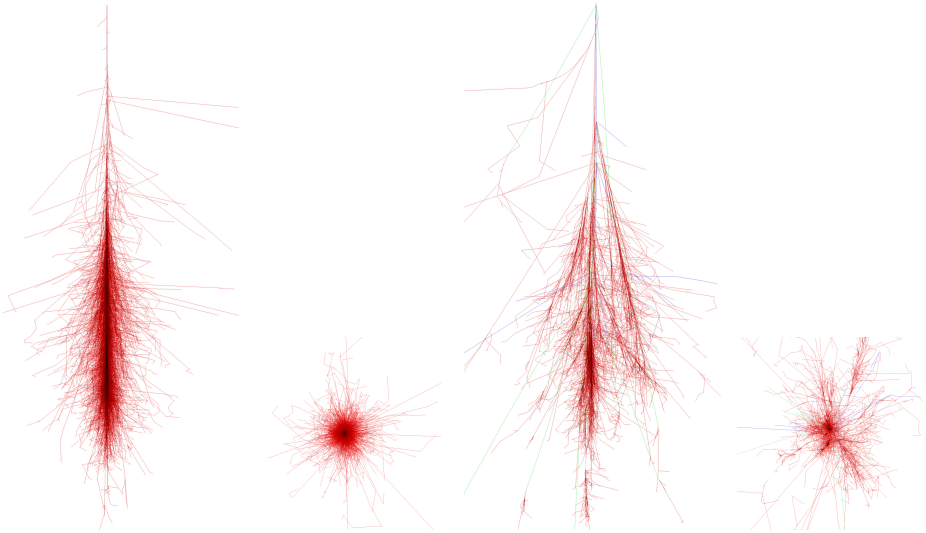

(a) **(b)**

Figure 1.2: `corsika`-simulated electromagnetic **(a)** and hadronic **(b)** showers as seen from the x-z (left) and x-y (right) planes. In both cases, the energy of the primary particle is 100 GeV. Source: `https://www.iap.kit.edu/corsika/`

Simulations have become more accurate in recreating the morphology of both electromagnetic and hadronic showers and nowadays can be considered as an essential tool for the analysis. One of the most commonly used software libraries is called `corsika` [4] and two examples of simulated showers are shown in Figure 1.2.

1.2.1 Electromagnetic shower models

To explain the development and morphology of electromagnetic showers, Heitler proposed a very simple model based on its scale invariance property.

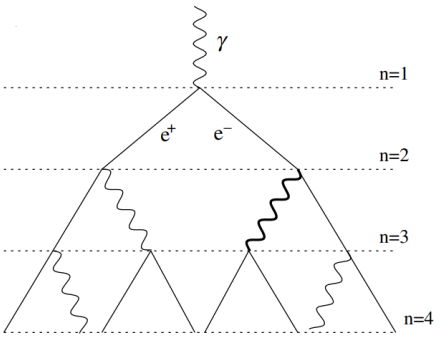

Figure 1.3: Scheme of an electromagnetic shower, where n represents the number of the crossed splitting lengths. Photons split via pair production, while electrons (e^-) and positrons (e^+) via bremsstrahlung. Taken from [5].

As one can see from the scheme in Figure 1.3, every element of the shower splits (via either pair production or bremsstrahlung, depending on its nature) after crossing the so-called *splitting length* d that is related to the radiation length in the atmosphere [5]:

$$d = \lambda_T \ln 2 \tag{1.3}$$

Every time a particle interacts and splits, the products will have an energy equal to half of it. The shower develops thanks to the particle splitting until the energy of the electrons (positrons) reaches a threshold value, called *critical energy* E_c: for energies lower than E_c, the ionization losses of electrons (positrons) start to dominate over the bremsstrahlung emission. In the air, $E_c = 86$ MeV [6]. Once this condition is met, the shower gets to its maximum extension.

After crossing n splitting lengths (i.e. at the n^{th} generation), the total number of particles in the shower will be 2^n and each one of them will carry an energy of $E_0/2^n$, where E_0 is the primary γ-ray energy. Taking this into consideration, it is possible to determine the number of generations corresponding to the shower maximum n_{max} and the atmospherical penetration depth at the maximum X_{max} as:

$$n_{max} = \frac{\ln(E_0/E_c)}{\ln 2} \tag{1.4a}$$

$$X_{max} = \lambda_T \ln\left(\frac{E_0}{E_c}\right) \tag{1.4b}$$

To better model the lateral development of the shower, Moliere's theory on multiple Coulomb scatterings must be included in the treatment (more details in [7]).

Even though Heitler's model is quite simplistic and does not take into account several effects that could influence the shower when travelling inside the atmosphere, some of its predictions, such as the logarithmic behaviour of X_{max} as a function of the energy, have been confirmed by simulations.

1.2.2 Hadronic shower models

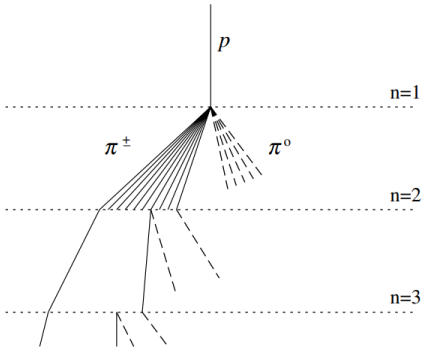

Figure 1.4: Scheme of a hadronic shower, where the dashed lines represent the neutral pions that generate the hadron-induced electromagnetic showers. Taken from [5].

Due to their elaborated inner structure, hadronic showers are way more complicated to model when compared to their electromagnetic counterparts and it is not possible to obtain analytic expressions for their characteristic parameters. In this case, simulations become a crucial tool to build the models.

However, some approximated analytical models have been developed to flank simulations. One example is the model by Matthews, treated in [5], which can be seen as a generalization of Heitler's model for electromagnetic showers. The main points of Matthews-Heitler's model are:

- at every interaction, the hadron will produce a certain number of sub-particles and one-third of them will be neutral (i.e. neutral pions, π^0), while the remaining two-thirds will be charged (i.e. positive and negative pions, π^+ and π^-);
- the energy of the primary particle is equally distributed between its products;

- while neutral pions immediately decay into electromagnetic sub-showers, the charged ones keep interacting with atmospheric atoms until they reach a given value of energy, the *decay energy* E_d, below which they decay into muons;
- to describe the interaction between a cosmic ray nucleus and the atmosphere, one can use the superposition theory, according to which every nucleon with the atomic number A can be treated as an ensemble of A independent protons, each one of them initiating a hadronic shower;
- by adopting the superposition assumption, one can find an approximated expression of the shower depth and find out that it is strongly dependent on the mass of the primary particle: the heavier the nucleus and the less penetrating (i.e. the smaller X_{max}) will be.

1.2.3 Cherenkov radiation

Cherenkov radiation is emitted whenever a charged particle travels inside a medium at a speed larger than that of light in the medium.

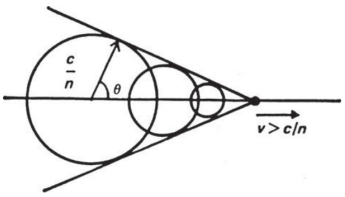

Figure 1.5: Geometrical representation of the Cherenkov radiation, where ϑ is the angle of emission of the beam with respect to the particle's direction of motion, which is defined by the vector of the speed $\mathbf{v}$. Taken from [2].

The emission occurs due to the fact that the electromagnetic field produced by the moving charged particle polarizes the medium it is crossing. During the interactions, electrons are not excited nor ionized, they are just displaced from their original positions when following the waveform of the pulse. If the particle travels at a speed $v < c/n$ (where n is the refraction index in the medium), then the dipoles are formed only around the charged particle and electrons immediately go back to their original place, the polarization is symmetric and no large-scale effect can be observed. Instead, if $v > c/n$, the polarization is asymmetric and the contributions from different points of the trajectory arrive in phase at the observer as a narrow coherent light pulse.

From simple considerations reported in [8], one can derive the *Cherenkov relation* for the angle of emission of the beam with respect to the direction of motion:

$$\cos\vartheta = \frac{c}{nv} = \frac{1}{\beta n} \tag{1.5}$$

where $\beta = v/c$. This equation shows why the emission of Cherenkov radiation is usually considered the equivalent of a sonic boom in the air (Figure 1.5).

1.2.3.1 Cherenkov light in the atmosphere

From Eq. 1.5, it is easy to understand that the maximum aperture of the Cherenkov cone is achieved for $\beta \longrightarrow 1$. Recalling the value of the refraction index in the air at sea level, $n = 1.00029$, one can find the maximum beam angle of Cherenkov light: $\vartheta_{max,air} \simeq 1.3°$.

Instead, by defining $\vartheta_{min} = 0°$, one can obtain the threshold energy for particles in order to produce a Cherenkov beam inside air:

$$E_{th} = \frac{m_{part}c^2}{\sqrt{1-\beta_{min}^2}} = \frac{m_{part}c^2}{\sqrt{1-n^{-2}}} \tag{1.6}$$

$E_{th,e^-} = 21$ MeV for electrons and $E_{th,\mu} = 4.3$ GeV for muons [9, 10]. Since in the air $E_c = 86$ MeV (see § 1.2.1), all the secondary particles of the electromagnetic (and hadronic) shower can produce Cherenkov light when travelling towards the ground.

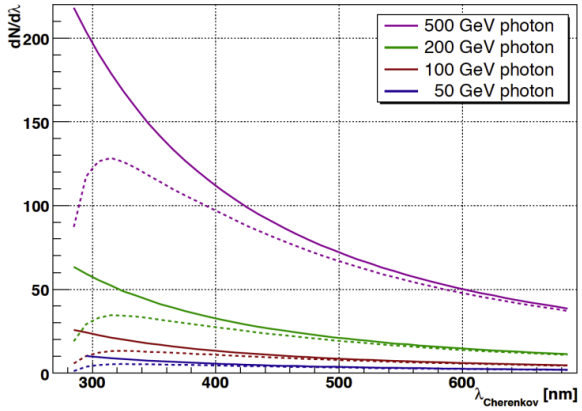

Figure 1.6: Spectrum of the Cherenkov light emitted at 10 km of altitude by γ-ray photons of different energy (solid lines) and the corresponding spectrum detected at 2200 m a.s.l. (dashed lines). Taken from [3].

The number of photons produced in an extensive shower per unit path length and wavelength can be defined as:

$$\frac{d^2N}{dxd\lambda} = \frac{2\pi\alpha z^2}{\lambda^2}\left(1 - \frac{1}{\beta^2 n^2(\lambda)}\right) \tag{1.7}$$

where $\alpha = 1/137$ is the fine-structure constant, λ is the wavelength of the emission, and $n(\lambda)$ is the refraction index that depends on wavelength [11]. However, the observed

spectrum (Figure 1.6, dashed lines) is not the same as the emitted one (Figure 1.6, solid lines) because of the interaction of the optical light with the atmosphere. In particular, Mie and Rayleigh scattering, and absorption by molecules such as CO_2, O_3 and water vapour are the most relevant processes that contribute to the attenuation of Cherenkov radiation in the atmosphere. The characteristic feature of the observed spectrum is the *hump*, located at around 300-350 nm independent of the energy of the original photon. The presence of the hump is the reason why Cherenkov light is commonly observed as a blue beam of optical-UV light.

1.3 The VHE γ-ray sky

As of September 2023, about 250 sources, more or less one-half Galactic and the other extragalactic, make up the current picture of the VHE γ-ray sky.

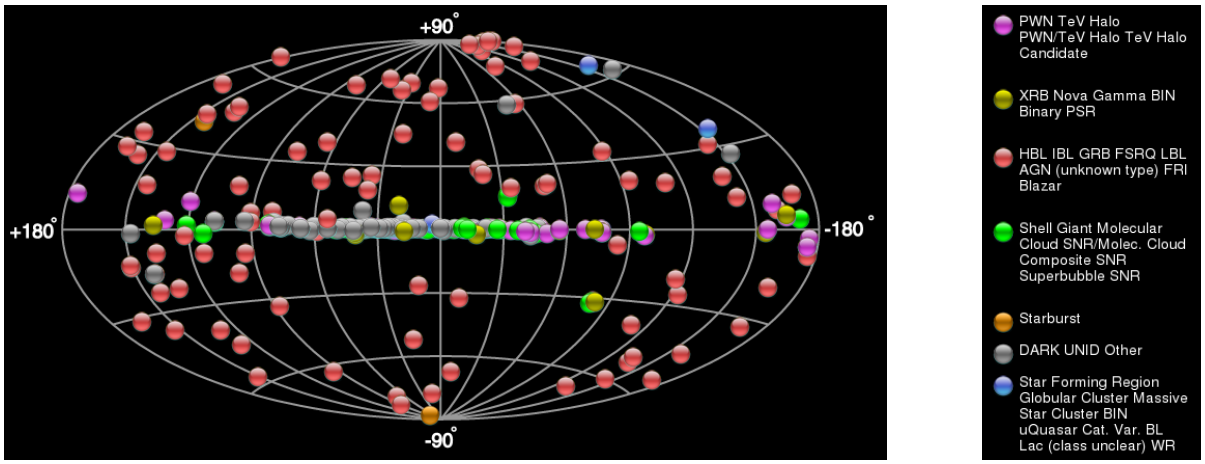

Figure 1.7: The TeV sky as of September 2023. Source: `http://tevcat.uchicago.edu/`.

The known classes of γ-ray emitting sources are:

- **Pulsars**

  Pulsars are quickly rotating highly-magnetized ($B \simeq 10^{11} - 10^{13}$ G) neutron stars; they were discovered thanks to the detection of a radio pulse with a highly regular period in time. The pulsed emission, whose energy is mainly provided by rotation (see § 3.1), is concentrated inside two narrow beams that can be observed only when they intercept the line of sight since the magnetic field and rotational axis are not aligned, at least in most cases.

  Pulsars are usually detected in the radio band, but an increasing number of them is being detected in the γ rays. Some of them have been observed also in the TeV

domain, even though the mechanism at the basis of the VHE emission is still not well understood. More details on the topic are reported in Chapter 3 of the present work.

- **Pulsar Wind Nebulae (PWNe)**

  Pulsars, especially the young ones, are able to create strong relativistic particle winds that can interact with the surrounding Supernova Remnant or medium producing the bubbles known as Pulsar Wind Nebulae. The accelerated particles can radiate in the entire electromagnetic spectrum, including the TeV domain: synchrotron emission is responsible for the low energy part of the spectrum, while Inverse Compton is the main mechanism at the basis of the high energy radiation. The most known PWN is the Crab Nebula. More details on their emission mechanisms can be found in [12].

- **Supernova Remnants (SNRs)**

  The life of a massive star ($M \gtrsim 10\ M_{\odot}$) ends with a Supernova (SN) explosion, during when the star's core collapses into a compact object, either a neutron star or a black hole, while the outer layers are expelled into the ISM surrounding the star to build the Supernova Remnant. The most common SNRs are the *shell-like remnants* that show a ring-like morphology and whose emission comes only from the ejecta of the Supernova explosion. A smaller number of SNRs, instead, is classified as *composite remnants* because they show a mixed morphology between shell-like SNRs and PWNe [13].

  Supernova Remnants are crucial sources for multimessenger studies and a significant number of them were found to be emitting γ rays in the VHE band, such as the Vela [14] and Cassiopea A [15]. Their TeV emission could be connected to the origin of cosmic rays since SNRs are considered one of the possible Galactic accelerators up to PeV energies (the so-called PeVatrons), even though this model still needs to be proved.

- **γ-ray binaries**

  They are binary systems composed of a compact object, either a neutron star or a black hole, and a massive star, usually a Be type, for which most of the emission is observed in the γ rays. Almost ten γ-ray binaries have been discovered to be TeV emitters and one example is HESSJ0632+057 [16]. The origin of the VHE emission of these objects is still unclear, but some models have been developed to explain it. One of them predicts that the compact object is a pulsar producing a relativistic wind that interacts with the massive star's stellar wind to accelerate particles. Another possibility could be the "microquasar scenario" for which the compact object is a stellar black hole accreting matter from the companion and its jets would be the origin of the TeV photons.

- **Novae**

  Novae are sudden outbursts coming from binary systems made of a white dwarf and a companion star, caused by a runaway thermonuclear explosion on the compact object's surface after it has accreted a critical amount of matter from the companion. The first detection of γ-rays coming from a Novae event took place in 2010 with *Fermi*-LAT [17] and nowadays around 20 Galactic novae have been detected at these energies. In 2021, a VHE outburst from the nova RS Ophiuchi was observed from both MAGIC [18] and H.E.S.S. [19]. The origin of the VHE emission, however, remains unclear.

- **Galactic Centre**

  The Galactic Centre has been detected in the TeV domain by several facilities and it is currently considered a steady TeV source of γ rays [20]. Additionally, H.E.S.S. Collaboration was also able to prove that the Galactic Centre is a source of PeV emission [21], even though it seems it is not enough to explain the origin of cosmic rays and their acceleration up to PeV energies.

- **Active Galactic Nuclei (AGN)**

  AGN are the most important extragalactic source in the γ-ray sky. They are galaxies that host a supermassive black hole ($M \simeq 10^6 - 10^9\ M_\odot$) at their centre that emits non-stellar radiation. AGN can be classified into families based on their spectral features, which are determined mainly by the viewing angle of the observer, according to the so-called Unified Model [22]. For the VHE band, the most relevant class is that of *Blazars*, i.e. AGN observed with a very small viewing angle with respect to the relativistic jets. Blazars show a strong γ-ray emission, as discovered with the Compton Gamma Ray Observatory (CGRO) [23], and can produce photons even in the VHE regime, as observed for example by MAGIC in 2011 [24] and many others.

- **Starburst galaxies**

  They are galaxies with a more prominent star formation rate with respect to usual late-type galaxies. Hence, also the supernova rate is higher, allowing the production of stronger shocks that can accelerate particles and emit VHE photons. Only two starburst galaxies have been detected in the TeV domain: M82, detected in 2009 by VERITAS at energies above 700 GeV [25], and NGC253, detected by H.E.S.S. above 220 GeV [26].

- **Gamma Ray Bursts (GRBs)**

  GRBs are one of the most extreme extragalactic γ-ray events in the sky and their discovery in the 1970s was completely unexpected. They are short and intense

bursts of γ-ray emission and can be classified into two families, following the bimodality of the distribution of the duration [27]: Short GRBs, which last less than two seconds, and Long GRBs, which have a duration longer than two seconds. It is thought that the different duration of the burst could be connected to a different kind of progenitor: Short GRBs would be produced after the merger of two compact objects, while Long GRBs would be produced by the collapse of massive stars [28].

The prompt emission of a Gamma Ray Burst is followed by an afterglow at lower energies, ranging from X-rays to infrared, but some models predict a VHE emission during the prompt phase. In 2019, MAGIC Collaboration was able to perform the first detection of a GRB's afterglow in the TeV domain [29].

Chapter 2

Detection of VHE γ rays

It is well known that the transmission coefficient through Earth's atmosphere changes depending on the wavelength of the incident electromagnetic radiation. As one can see from Figure 2.1, γ rays are entirely absorbed by the atmosphere and, consequently, space telescopes are needed to observe light emitted in the high-energy band. However, these instruments are limited when studying the most energetic γ rays because of the strict constraints in mass and volume of the scientific payload for space missions.

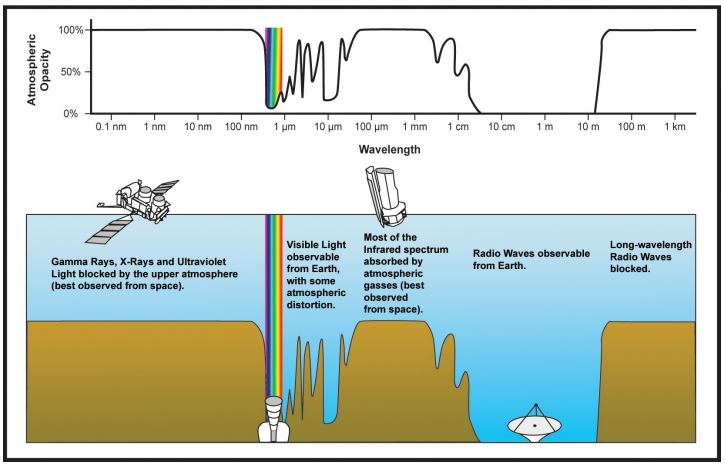

Figure 2.1: Atmospheric opacity as a function of the wavelength of electromagnetic radiation. Image created by NASA and of public domain, available at: `https://commons.wikimedia.org/atmospheric-opacity.jpg`

In this Chapter, the different techniques for γ-ray detection are presented, as well as the description of LST-1, the instrument adopted for the observations of the object of study of this present work.

2.1 Space telescopes

Classical γ-ray telescopes detect photons of different energies depending on the physical process at the basis of their interaction with matter[1]:

- **Compton effect**: a photon with energy E_γ collides with an electron at rest. As a consequence, the electron is scattered with an angle θ with respect to the trajectory of the incident photon, while the photon loses some energy and its wavelength decreases to $\lambda' < \lambda$ such that:

$$\Delta\lambda = \lambda - \lambda' = \frac{h}{m_e c}(1 - \cos\theta) \tag{2.1}$$

  Compton telescopes are the most used for energies between 1 MeV and 30 MeV, where Compton scattering is the dominating process for the interaction of γ rays with matter. They are made of two layers: in the first, the incident photon undergoes the Compton effect with an electron of the material, and then it is absorbed by the second level. From the photon's position and the energy in each layer, it is possible to define the *event circle* in the sky from where the original γ ray comes from. One example of a Compton telescope is COMPTEL on board the Compton Gamma Ray Observatory (CGRO).

- **Pair production**: it is the process by which a photon annihilates into an electron-positron pair as a result of its interaction with matter. The minimum energy for this to happen is twice the electron's rest-frame energy $E_{min} = 2m_e c^2$ because of the energy conservation principle.

  γ-ray detectors based on pair production are composed of several conversion layers to allow the production of pairs by the incoming photons and the reconstruction of their original position in the sky. To reconstruct the energy, instead, these telescopes are equipped with calorimeters that convert the energy of the pair into a measurable temperature variation. Examples of pair-production telescopes are *Fermi*-LAT or the detector EGRET on board CGRO.

The main issue with pair production telescopes is that calorimeters have a small effective area, which results in a meagre detection rate at energies higher than 100 GeV, even for strong sources. In other words, the calorimeter's dimensions are too small to contain photons of higher energies. Thus, the statistic of VHE photons detection with space telescopes, on average, is very poor. Much larger collecting areas would be needed to conduct comprehensive studies of such electromagnetic band. Nevertheless, *Fermi*-LAT was able to obtain significant results at $\sim$1 TeV by integrating $\sim$15 years of data.

[1] In this section the photoelectric absorption is not mentioned since it is the dominant process for energies lower than 1 MeV, so it is not of much interest for γ rays.

For this reason, since the first attempts in the 1970s, a new ground-based technique has been developed: by using the atmosphere as a calorimeter, it is possible to indirectly detect γ rays by studying the electromagnetic showers they produce via pair-production mechanism when interacting with atoms inside the atmosphere (see § 1.2).

2.2 Ground-based facilities

By analysing the extensive atmospheric showers, one can retrieve information on the primary γ ray that initiated them. The secondary relativistic particles can be detected in two complementary ways: either through direct detection or by studying the Cherenkov light they emit when crossing the atmosphere. For the first method, Surface Arrays (SAs) and Water Cherenkov Detectors (WCDs) are available, while for the second one Imaging Atmospheric Cherenkov Telescopes (IACTs) are employed.

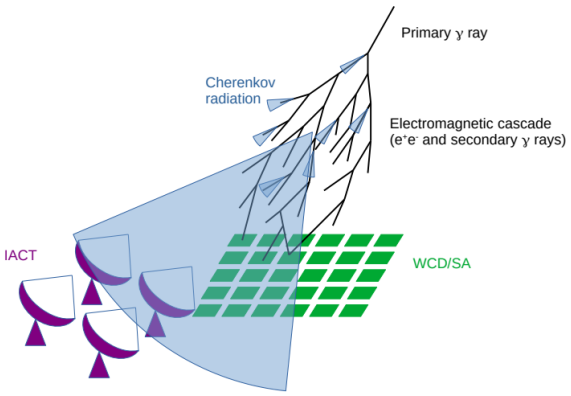

Figure 2.2: Mechanism for the ground-based detection of γ rays, for both IACTs (purple) and SAs/WCDs (green). Image taken from [30].

A shower initiated by a TeV γ ray tends to reach its maximum at around 10 km of altitude a.s.l. and produces a *light pool* on the ground with a radius of $\sim$120 m [30]. If the IACT is placed inside the light pool of the shower, then it can detect the Cherenkov emission produced by the particles (Figure 2.2). Conversely, a SA or a WCD must be placed at a high altitude above sea level to be able to catch the shower particles.

Even though the two families adopt the same methods for the reconstruction of the primary γ ray and have similar problems with the cosmic ray background, the two approaches are significantly different and must be analysed separately to understand their capabilities and limitations.

2.2.1 Particle detectors

Since both SAs and WCDs aim at directly studying the secondary particles and, as previously reported, the typical altitude of a TeV electromagnetic extensive shower is around 10 km above sea level, these facilities must be placed at high locations.

Surface Arrays are arrays of dense-packed scintillators distributed over a large area in order to maximise the sky coverage and contain the whole shower inside. Scintillators are widely used detectors for X-ray and γ-ray astronomy and the basic principle of functioning is the conversion of the energy deposited by the incident photon (or charged particle) onto the organic or inorganic material of the instrument into optical-UV photons, in such a way that the final amount of optical light is proportional to the initial energy deposit.

On the other hand, Water Cherenkov Detectors are made of closely-packed water tanks with photodetectors (usually Photomultiplier Tubes, PMTs) at their bottom. When the highly-relativistic particles of the shower enter the tanks, they travel faster than light inside the water ($\vartheta_{max,water} \simeq 41°$) and produce a Cherenkov beam that is detected by the PMTs. Photomultiplier Tubes are widely employed in γ-ray astronomy because they are quite simple detectors that can provide a high temporal resolution, which is a crucial property since they must study the ns-long beam of Cherenkov light emitted by particles.

Nowadays two main operating facilities directly detect the particles in the shower:

- **High Altitude Water Cherenkov (HAWC)** experiment, [31], located at ∼4100 m a.s.l. on the Sierra Negra in Mexico. It can be considered as the successor to the MILAGRO experiment and it is made of 300 water tanks distributed over an area of about 22000 m^2. Its sensitivity is 100 GeV - 100 TeV (Figure 2.3b).

- **Large High Altitude Air Shower Observatory (LHAASO)**, [32], located at ∼4400 m a.s.l. on Mount Haizi in Daocheng (China). It includes four separate facilities: an array of electromagnetic particle detectors and muon detectors, with an area of 1.3 km^2 (KM2A), a WCD array with an area of 78000 m^2 (WCDA), 18 wide field-of-view air Cherenkov telescopes (WFCTA) and an electron-neutron detector array covering an area of 10000 m^2 (ENDA). For γ rays, the operating energy range is between ∼200 GeV and 1 PeV(Figure 2.3b).

2.2.2 Imaging Atmospheric Cherenkov Telescopes

Cherenkov telescopes consist of mirror dishes, which can be segmented if the diameter is large, that collect the photons produced by particles and are coupled to a pixelized camera where the light reflected by the dish is converted into an electronic signal to produce the final image of the shower by combining spatial and temporal information. To enhance the imaging capabilities of these telescopes, the camera is usually made of

thousands of pixels coupled to photodetectors such as either PMTs or Silicon Photomultipliers (SiPMs). The typical Field of View of a current-generation IACT camera is about 4-5°.

One of the common optical designs for the mirror is the Davies-Cotton layout, an empirical solution that was originally developed for solar concentrators, because it has a better off-axis performance when compared to a parabolic design. The main drawback of this layout, however, is that it is not isochronous: due to the particular configuration of the mirror facets, the photons' arrival times at the camera are different. This effect is usually negligible in the case of small diameters (lower than ∼10-15 m) but, if the mirror size is larger, then a parabolic design must be adopted.

Another essential component of the IACT system is the *trigger*. The camera pixels, during observations, are always exposed to a non-negligible signal that represents the Night Sky Background (NSB) and it is necessary to evaluate if a detected signal is significant or if it is just background noise. The trigger system is designed to be able to make this discrimination. Basically, the signal will be registered only if the number of counts in a certain amount of neighbouring pixels is larger than a previously decided threshold value. In this regard, the signal coming from the PMTs is split into two identical copies: one is sent to the DAQ, which is equipped with a buffer to store it until the trigger makes its decision, and the other goes to the trigger system to be analysed.

The main issue with IACTs is that the image obtained with a single telescope is not always sufficient to reconstruct the shower's parameters with high accuracy. For this reason, the *stereoscopic technique* was developed: several IACTs are placed together into an array so that they can observe the same shower, and then the images are combined to provide a better reconstruction of the parameters and reduce the background influence. The currently operating stereoscopic IACT facilities are:

- **High Energy Stereoscopic System (H.E.S.S.)** experiment, [33], an array of one 28 meters and four 12-meter telescopes located in Namibia. The first telescope has performed observations since 2002, while the array started operating in 2004 and in 2012 the 28-m telescope was added. The operating energy range is between 30 GeV and ∼100 TeV (Figure 2.3b).

- **Major Atmospheric Gamma-ray Imaging Cherenkov (MAGIC)** experiment, [34, 35], an array of two 17 meters telescopes located in La Palma (at the same location of CTAO's Northern Array). The first telescope has been providing data since 2004, while the stereoscopic system started being operative in 2009. The sensitivity of MAGIC goes from 60 GeV up to 20 TeV (Figure 2.3b).

- **Very Energetic Radiation Imaging Telescope Array System (VERITAS)** experiment, [36], an array of four 12-meter telescopes located in Arizona. The first telescope of the array detected its first light in 2005. The sensitivity of the stereoscopic system is from 50 GeV to 50 TeV (Figure 2.3b).

2.2.3 Comparison between the techniques

The average performance of the two techniques can be compared and the most relevant parameters are reported in Table 2.1.

Table 2.1: Comparison between the typical performances of the two ground-based techniques for γ-ray detection. Taken from [30].

	IACT	**SA/WCD**
Energy threshold	$\sim$ tens of GeV	$\sim$ TeV
Duty cycle	$\sim 10\%$	$\sim 100\%$
Field of View	$\sim$ tens of deg^2	$\sim$ sr

The differences in the energy threshold are related to the method for the detection: while IACTs are able to study all the components of the shower (head, core, tail)[2], WCDs/SAs are limited to the tail. The only way to lower the energy threshold would be to build new facilities at higher altitudes, but it does not sound simple anyways.

Instead, for what concerns the duty cycle, i.e. the daily amount of time during which the instrument can work, WCDs/SAs are way better than IACTs because they can operate also during the day. IACTs, being optical telescopes, are strongly sensitive to the sky background and, even during the night, they are limited by the atmospherical conditions and by the contamination of the moonlight.

The last relevant property that must be mentioned is the Field of View (FoV). Because of the different designs of the facilities, IACTs can be considered pointing instruments (they only point a region of the sky inside a limited FoV), while WCDs/SAs can survey a large portion of the sky (large FoV because they do not point a particular region).

Keeping all these features in mind, it is evident why both instruments are needed to gain a better knowledge of the VHE band. The two families are complementary to each other and only by combining their results together it is possible to obtain complete studies of the sources of interest.

2.3 The Cherenkov Telescope Array Observatory

The Cherenkov Telescope Array Observatory (CTAO) is the upcoming facility for ground-based detection of γ rays through IACT arrays. The aim behind the development of the CTAO is to significantly advance the performances of current instruments in the TeV domain and study unexplored energy ranges that could return crucial information for both physics and astrophysics.

[2]The head is the fraction of light emitted at the highest altitudes, usually above 10 km, the tail is the light emitted at the lowest altitudes, below 6 km, and the core is the light emitted in between.

To improve the sensitivity in the VHE range, CTAO has the goal to increase the current IACTs' field of view by at least a factor of two and to achieve an arcminute angular resolution and an energy resolution in the TeV band of the order of 10%. The results of simulations for CTAO's future performance are shown in Figure 2.3; these curves also highlight the need of combining the data from different facilities since particle arrays, such as LHAASO, show better performances than CTAO's arrays for energies of the order of hundreds of TeV.

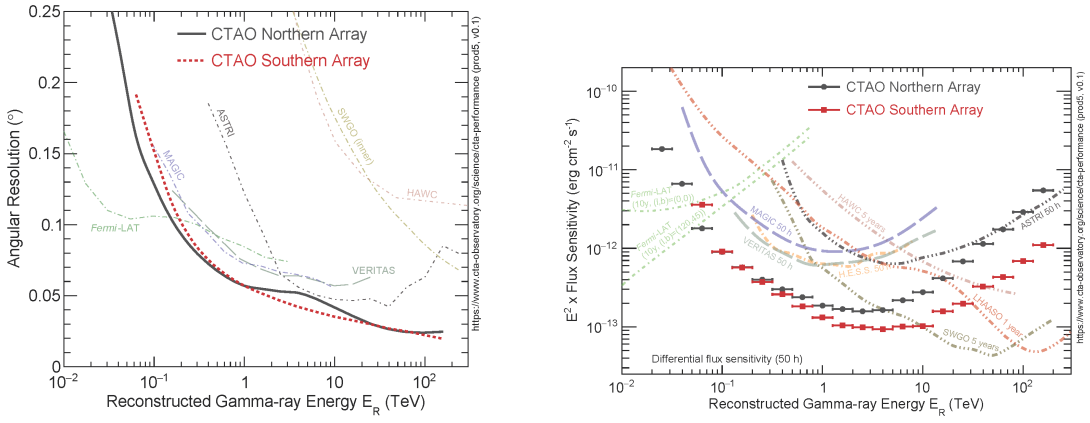

(a) Simulated angular resolution.

(b) Simulated sensitivity.

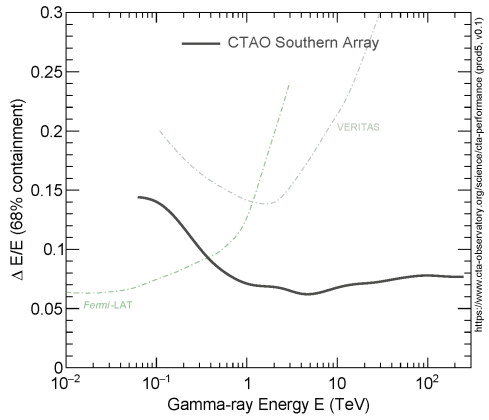

(c) Simulated energy resolution.

Figure 2.3: Simulated angular resolution **(a)** and sensitivity **(b)** of CTAO's Northern (in black) and Southern (in red) arrays, compared to the same curves for current instruments. The simulated energy resolution for the Southern Array is shown in **(c)**. Source: `https://www.cta-observatory.org/`.

Not only the performance of current instruments will be advanced, but CTAO will cover the energy range from down 20 GeV up to around 300 TeV. The upper boundary

is significantly higher than the present one, around a few tens of TeV, implying it will be able to improve the knowledge of this still-not-well-known energy range. The lower boundary is probably even more relevant: γ rays interact via pair production with the Extragalactic Background Light in the optical-IR (i.e. the universe is opaque to γ rays), but this effect starts becoming negligible at 20 GeV. With this threshold, CTAO will be capable of recovering the emission at redshift up to $z \simeq 4$.

The last property that must be mentioned is the improved capability in the detection of transient phenomena, a significant component of the study of the early universe. CTAO's telescopes will be able to react to alerts for transient events from other facilities in the world within about one minute.

To accomplish the proposed goals, three telescope designs have been developed: Large-Sized, Medium-Sized and Small-Sized telescopes. Each one of them has been optimized for the study of a particular sub-band of CTAO's energy coverage: LSTs for the Sub-TeV domain (20 - 150/200 GeV), MSTs for the core TeV energies (0.2 - 5 TeV) and SSTs for the Multi-TeV regime (5-300 TeV).

To reach the largest sky coverage possible, two arrays have been planned to be built, one in the Northern and the other in the Southern Hemisphere. The preliminary design of CTAO is known as the Alpha Configuration (Figure 2.4):

a) The Northern Array will be located in the Observatorio Roque de los Muchachos in La Palma and will include 4 LSTs and 9 MSTs covering an area of $\sim$0.25 km^2;

b) The Southern Array will be located in the Atacama desert, near ESO Paranal Observatory, and will include 14 MSTs and 37 SSTs covering an area of $\sim$3 km^2. In this configuration, no LST will be placed here, even though the future locations of four LSTs and three additional SSTs have already been decided.

The two arrays will not be similar in the number of telescopes and design since they will be focused on two different purposes. The Milky Way is better viewed from the Southern Hemisphere and, for this reason, the Southern Array will be specialised in the search for Galactic sources. On the other hand, the Northern Array will study mainly extragalactic and cosmological sources, as well as transient phenomena.

2.4 The Large-Sized Telescope

The Large-Sized Telescope (LST) is one of the three telescope designs developed for CTAO. Its performance peak is located at the lowest energy range of the VHE band, from 20 GeV to 150-200 GeV: at such low energies, γ-ray events generate very faint Cherenkov light beams, thus large collecting surfaces are required to detect the emission and discriminate it between the background signal.

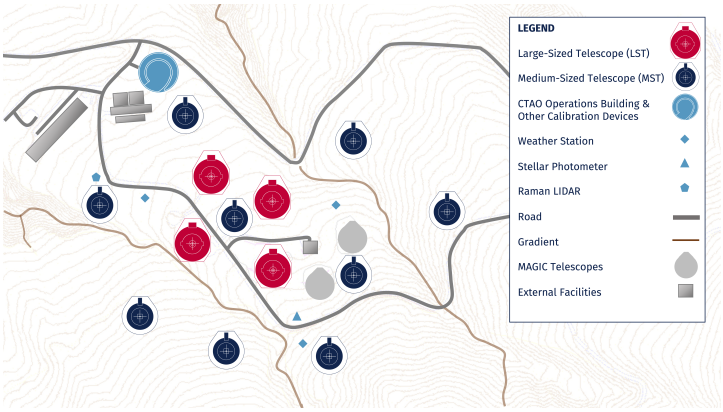

(a) Northern Array.

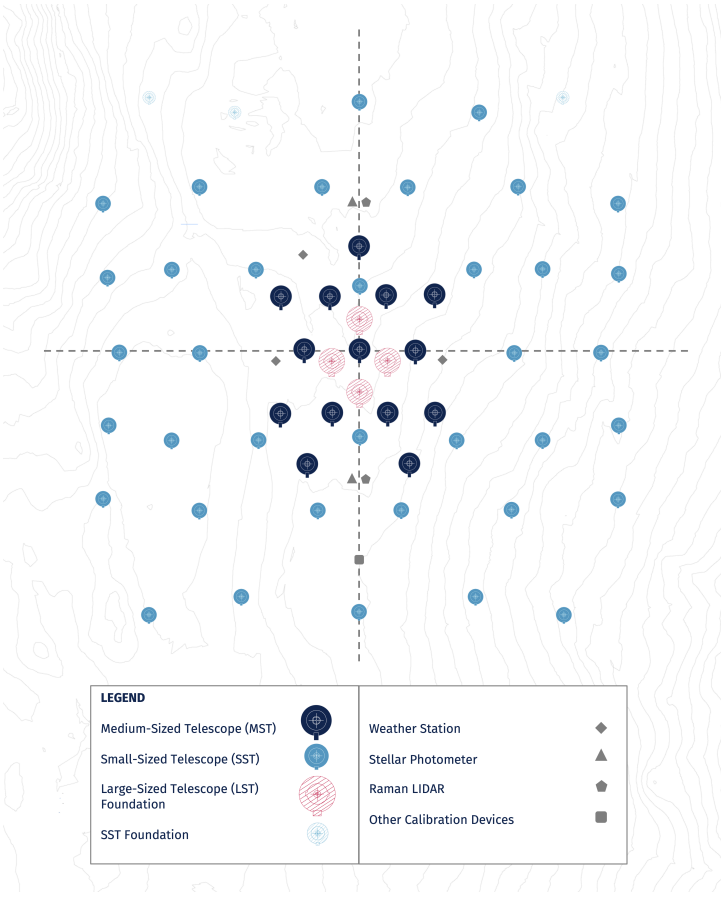

(b) Southern Array.

Figure 2.4: Alpha configuration of CTAO's Northern **(a)** and Southern **(b)** Arrays. Source: `https://www.cta-observatory.org`

LSTs will build the core of the Northern Array and the first one of them, LST-1 (Figure 2.5), has already been built and has been providing data since November 2019. The construction of the other three telescopes is ongoing.

Two main properties drove the design of the LST: the fast repositioning of the telescope for reaction to transient phenomena and the high sensitivity to γ rays at the low edge of the VHE range [37]. Indeed, the total weight of about 100 tonnes allows the repositioning of the telescope to any position of the sky in about 20 s from the alert.

The reflective system is made of a single parabolic segmented dish (Table 2.2) made of 198 mirror facets, which can be moved with the Active Mirror Control system. Thanks to the manufacturing technique, the absolute reflectivity of the segments in the optical range between 330 and 500 nm is above 85% [38].

The mirror is coupled to a PMT-based highly pixelized camera (Table 2.2) made of 265 modules, each one of them divided into 7 channels for a total of 1855 pixels. The PMTs convert the light collected by the dish into a signal that can be analysed by the readout electronics, which is based on the same system as MAGIC, the Domino Ring Sampler version 4 (DRS4). The light signal, after the sampling, is converted by an Analog-to-Digital Converter into a digital signal. The camera readout has two channels with different amplification, high gain and low gain channels so that the wide dynamic range from 1 to 3000 photoelectrons is covered [39].

Table 2.2: Main parameters of the Large-Sized Telescope. Taken from [38].

Mirror dish	Optical design	Parabolic
	Diameter	23 m
	Focal length	28 m
	Mirror area	368 m^2
Camera	Sensors	PMTs
	Number of pixels	1855
	FoV	4.5°

When the other three LSTs of the Northern Array will be operative, their cameras will be connected to each other in order to obtain an online coincidence trigger that will be able to suppress accidental triggers by a factor of 100 [38]. This property is crucial to improve the final quality of the data and reduce the contribution of the background, which is particularly relevant in the optimisation range of LST.

Currently, there are some ongoing projects for the development of a LST camera based on SiPMs, one example is reported in [40]. The replacement would bring several improvements: a higher-duty cycle, better robustness and a higher granularity of the camera that allows having a better angular resolution of the images. However, SiPMs have a higher quantum efficiency in the optical-NIR band compared to PMTs and this

Figure 2.5: LST-1 prototype at the Observatorio del Roque de los Muchachos, in La Palma. Source: `https://www.flickr.com/LST`.

implies they are more sensitive to background photons. Moreover, SiPM cameras would have, as already reported, a higher number of pixels, which allows having a better angular resolution and increases the capability of discriminating between hadronic and electromagnetic showers but implies a higher power consumption and data output.

2.4.1 LST analysis pipeline

LST acquires data at a rate of the order of 10^4 events/s (10 kHz), even though not all of them are associated with the showers. During the observations, in addition to the physical events (the so-called *cosmics*), the data acquisition (DAQ) system also registers interleaved events, useful for the calibration, of two types:

- Pedestal events (rate$\sim$100 Hz): they represent a measure of the background noise to which the camera is exposed when pointing to a certain region of the sky;
- Flatfield events (rate$\sim$100 Hz), acquired when the camera is uniformly illuminated.

Once the DAQ system has the events, it is essential to reduce the volume of the data files. The pipeline for the data reduction chain is made of several levels, defined by the model that will be adopted in the future for CTAO data [41], and one can divide it into two main parts:

a) low-level analysis (more details in § 4.2), for which the software library `cta-lstchain` [42] has been developed. By using it, the camera's raw data, which usually include hundreds of thousands of numbers per event, are converted into files including the list of the candidate γ-ray events, with a few associated parameters;

b) high-level analysis (more details in § 4.3) using the open-source Python package `gammapy` [43] developed for γ-ray data analysis (for CTAO in particular, but it is used also for other facilities), from which it is possible to obtain the final science products such as Spectral Energy Distributions (SEDs) or light curves.

Chapter 3

γ-ray pulsars and Geminga

The discovery of pulsars in 1967 by Jocelyn Bell Burnell [44] is one of the milestones of astrophysics. First detected in the radio band, researchers were not sure where the extremely regular periodic signal came from and they even hypothesized it was artificial or of extraterrestrial origin. However, in the same year, Franco Pacini theorised that a rotating and magnetized neutron star could produce radiation [45], thus these compact objects were later proposed as the origin of the pulsed emission. This hypothesis was then confirmed by the association of a pulsar with the Crab Nebula [46]. The Crab was also the first identified γ-ray pulsar: the discovery of its emission at high energies occurred in 1971 [47], then it was identified as a pulsar thanks to the association with its SNR. Nowadays, almost 300 pulsars are known to be γ-ray emitters[1].

In this Chapter, a general introduction to pulsars and γ-ray pulsars is presented, along with the most important discoveries about the object of study, the Geminga pulsar, and its emission in the VHE.

3.1 Basic theory on pulsars

Pulsars are fastly rotating and highly magnetized neutron stars that emit radiation concentrated inside two narrow cones. Their emission can be detected only if the light cones intercept the observer's line of sight (the so-called *lighthouse effect*) and it consists of pulses with a regular period in time.

3.1.1 Neutron stars

The life of a star is ruled by the balance between the gravitational force, which tends to drive it towards a collapse, and the thermonuclear reactions, opposing gravity. In the case of low-mass stars ($M < 10\ M_{\odot}$), the chain reactions inside the core can only reach the

[1] `https://stanford.edu/list-of-detected-gamma-ray-pulsars`

production of carbon-oxygen, and electron degeneracy pressure is the only way to prevent a gravitational collapse. The ending stage of their life is a white dwarf, whose equilibrium can be sustained only if its mass is below the Chandrasekhar limit ($M_{ch} = 1.4\ M_\odot$). For massive stars ($M \gtrsim 10\ M_\odot$), instead, the thermonuclear chain can reach iron, the last element that can be produced through nuclear fusion, but electron degeneracy is not sufficient to support the core against the collapse. With the temperatures at play, the mass defect between protons and neutrons can be overcome, and free protons start to capture electrons to build neutrons via β processes: $p^+ + e^- \longrightarrow n + \nu_e$. The remnant of the collapse of a massive star will be a degenerate core mainly composed of neutrons, thus a Neutron Star (NS). If the mass of the NS is below the Oppenheimer-Volkov limit, around 2-3 $M_\odot$, neutron degeneracy can counterbalance gravity, otherwise no degenerate state can win over the gravitational force, and the core collapses into a black hole.

Neutron stars are the densest objects in the universe, with average values of radius and mass of $R \simeq 10$ km and $M \simeq 1.5 - 2\ M_\odot$ that lead to densities of the order of $\rho \sim 10^{14}$ g/cm^3. Other two characteristic features are the high rotational speed and high magnetic field, due to the conservation of angular momentum and magnetic flux during the collapse. NSs can show pulsed emission at different wavelengths, from radio to γ rays, and they can be classified based on the primary mechanism supporting the emission: neutron stars primarily fueled by rotation are known as *Rotation-Powered Pulsars* (RPPs), those mainly supported by their magnetic fields are classified as *Magnetars*, then *Isolated Neutron Stars* (INSs) are powered by the latent heat of the neutron star's matter, and *Accretion-Powered Neutron Stars* by the accretion from a companion [48]. In this work, the focus will be on Rotation-Powered Pulsars only and, from now on, they will simply be addressed as Pulsars.

3.1.2 Period and classification of pulsars

Two parameters can be used to classify pulsars into families: their period P and its derivative $\dot{P}$. P tends to slowly increase with the age of the pulsar since radiation is emitted at the expense of rotation. The neutron star fastly rotates around its axis and so does its magnetic field, generating a strong electric field responsible for the production of the light cones and, as more and more energy is radiated away, the slower the rotation will be (i.e. the longer the period will be). The P-$\dot{P}$ plot, which can be seen as the counterpart of the Hertzsprung-Russell diagram for non-degenerate stars, is reported in Figure 3.1, where the two main families of pulsars are clearly visible.

Ordinary pulsars are the ones with periods usually ranging between $\simeq$0.1 and $\simeq$1 s and period derivatives clustered around $\dot{P} \sim 10^{-15}$ s/s. They usually enter the diagram from the upper-left corner and, as they age, they move towards the bottom-right part following their contour line of magnetic field. The evolution continues for 10^6-10^7 years until the period increases to values larger than 1 s and the rotation becomes so slow that it cannot support the emission anymore, making the pulsar unobservable.

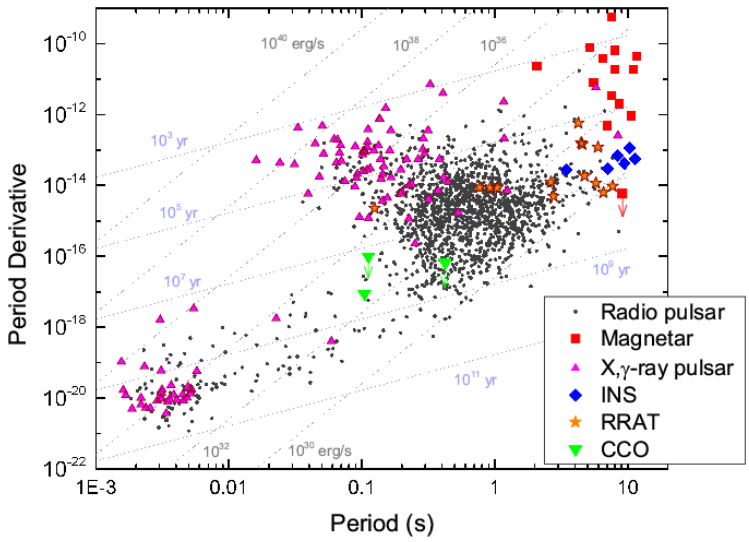

Figure 3.1: P and $\dot{P}$ diagram for different types of pulsars, listed in the legend. RRAT stands for Rotating Radio Transient, a peculiar family of pulsars discovered in recent years, which shows single isolated radio pulses with high variability. CCO stands for Central Compact Object, a kind of pulsar observed mainly in the soft X-rays and linked to SNRs. The plot also shows the contour lines for characteristic age and spin-down power. Taken from [48].

Nevertheless, there is an exception regarding pulsars inside binary systems. If these objects start accreting matter from the companion, the rotational speed will increase and they will be able to emit radiation again, even if their magnetic field is low ($B \sim 10^8$ G), due to the angular momentum conservation. These pulsars are known as *Millisecond Pulsars* (MSP), because of the period of the order of milliseconds despite their old age, or *recycled pulsars*, and they are located in the bottom-left corner of Figure 3.1.

The upper-right corner of Figure 3.1 is populated by magnetars, characterised by extreme magnetic fields of the order of $B \sim 10^{14} - 10^{15}$ G and a much slower rotational speed when compared to ordinary pulsars.

The period and its derivative are useful to estimate three characteristic parameters of pulsars: spin-down power, age, and magnetic field. To do so, however, one must adopt the *oblique rotator* model (developed by Pacini [45] and Gold [49]) for which the magnetic field axis of the neutron star is not aligned with the rotational one.

3.1.2.1 Spin-down power

Assuming that the pulsed emission is fueled by rotation, i.e. the neutron star emits radiation at the expense of its rotational energy, then one can define the spin-down power (or spin-down luminosity) as:

$$-\frac{dE_{rot}}{dt} = \dot{E} = I_{NS}\Omega\dot{\Omega} = I_{NS}4\pi^2\frac{\dot{P}}{P^3} \tag{3.1}$$

where I_{NS} is the pulsar moment of inertia, $\Omega = 2\pi/P$ the angular frequency and $\dot{\Omega}$ its derivative. The typical values for the spin-down power of pulsars lie in the range $\dot{E} \sim 10^{30} - 10^{38}$ erg/s.

3.1.2.2 Characteristic age

The oblique rotator model predicts the following relation: $\dot{\Omega} = -k\Omega^n$, where n is called *braking index* (in the case of dipole emission, as predicted by the model, $n \simeq 3$) and k is a proportionality constant.

Introducing the initial spin period of the pulsar P_0, it is possible to define the age of the pulsar as:

$$\tau = \frac{P}{(n-1)\dot{P}}\left[1 - \left(\frac{P_0}{P}\right)^{n-1}\right] \tag{3.2}$$

with $n \neq 1$. Assuming that the emission is of dipole origin, i.e. $n = 3$, and that $P_0 \ll P$ one can infer the characteristic age of the pulsar:

$$\tau_c = \frac{P}{2\dot{P}} \tag{3.3}$$

However, one must remember this is not the exact age of the pulsar and usually τ_c overestimates the real value. For example, in the case of the Crab pulsar, the characteristic age is $\tau_c \simeq 1240$ yr, but the supernova explosion is dated to 1054 AD, leading to a real age of 969 yr; the discrepancy increases even more for younger pulsars. More details on the topic can be found at [50].

3.1.2.3 Surface magnetic field

Assuming again that the radiation is of dipole origin, one can obtain the expression for the surface magnetic field as a function of P and $\dot{P}$:

$$B \simeq (10^{39}P\dot{P})^{1/2} \simeq 3.2 \cdot 10^{19}(P\dot{P})^{1/2} \tag{3.4}$$

The accurate computations to obtain the relation are reported in [51].

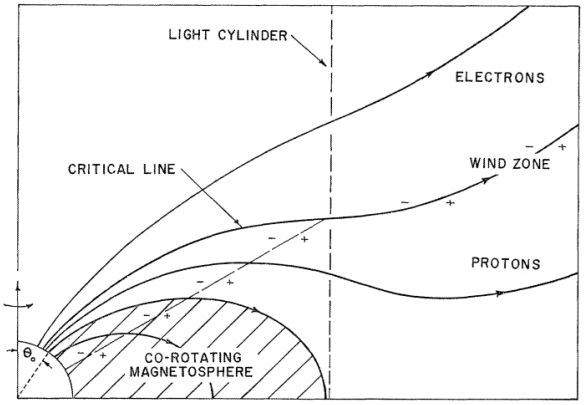

Figure 3.2: Close-up of the pulsar magnetosphere and all its components. Taken from [52].

3.1.3 Magnetosphere

The oblique rotator models, such as the one by Pacini, predicted that the neutron star, because of its strong gravitational field, must be surrounded by a vacuum region. Goldreich and Julian in 1969 [52] were able to prove that the previous conclusion was wrong and that pulsars are surrounded by a region filled with plasma, the *magnetosphere*. To simplify the computations, they assumed that the magnetic field axis is aligned to the rotational one, even if it is not true for most pulsars.

The neutron star can be seen as a perfect conductor and the charges on its surface are able to induce an electric field that is parallel to the magnetic field and, thus, perpendicular to the star surface. The strength of the field is high enough to strip charges from the surface despite the gravitational attraction of the neutron star, and they are free to escape and build the magnetosphere, also known as the *near zone* (Figure 3.2). Because of the neutron star rotation, the magnetic field lines follow its motion and tend to co-rotate with it at the same speed Ω; this is the reason why this region is known as the *co-rotating magnetosphere*. Because Ω cannot be larger than the speed of light, the co-rotating magnetosphere is bounded by the *light cylinder*, an imaginary cylindrical surface defined by:

$$R_{LC} \cdot \Omega = c \tag{3.5}$$

By substituting the definition of Ω, one can obtain $R_{LC} \simeq 5 \cdot 10^9 \ P$ (cm), where P is the period of rotation of the neutron star. All the particles that stream along the magnetic field lines of the co-rotating magnetosphere are forced to rigidly rotate with the neutron star, but if the magnetic field line crosses the light cylinder, then particles are able to escape the rigid motion. All the lines that do not close within the light cylinder constitute the *open magnetosphere*.

Inside the co-rotating magnetosphere, the space-charge density of particles, later

renamed as *Goldreich-Julian density*, is:

$$\rho_{GJ} = \frac{\mathbf{\Omega} \cdot \mathbf{B}}{2\pi c} \quad \longrightarrow \quad n_{GJ} = 7 \cdot 10^{-2} B_z P^{-1} \quad \mathrm{cm}^3 \tag{3.6}$$

where B_z is the parallel component of the magnetic field B to the rotational axis (expressed in G). In the open magnetosphere, instead, because particles can escape the motion, the charge density decreases and a strong electric field can be produced; as a consequence, particle acceleration can take place.

Outside of the magnetosphere, the space is filled by the pulsar wind. This region, also known as the *wind zone*, is located between the light cylinder and the termination shock of the supernova cavity around the pulsar. Inside, the most important sources of the magnetic field are the currents produced by the charges escaping outside the light cylinder through the open field lines. A particular line which is reported in Figure 3.2 is the *critical line*: the electric potential along this line is the same as the one of the ISM outside of the shell of the SNR; electrons tend to escape following higher-latitude lines, while protons along lower-latitude lines [52].

Because of the assumption of Goldreich and Julian model, the neutron star emits as a dipole and this implies there are two magnetic field components, one toroidal and the other poloidal. In the wind zone, the toroidal component dominates over the poloidal one, while the opposite is true for the magnetosphere.

3.2 γ-ray pulsars

SAS-2 was the first telescope, in the early 1970s, to observe γ-ray emission from pulsars. Not only it detected both the Crab [53] and the Vela [54] pulsars, but it was able to recover γ-ray emission from an unidentified source [55] that later on was recognised to be Geminga.

The knowledge of γ-ray pulsars improved step by step during the decades. In the same years as the first SAS-2 results, the Polar Cap model (see § 3.2.1) for the high-energy emission of pulsars was proposed. Once COS-B was launched and the first data were published, different models (Slot Gap and Outer Gap models, see § 3.2.1) came out to explain the newly observed features, such as the high yield of γ-ray emission in both the Crab and the Vela pulsars.

The following operative satellite was EGRET, on board the Compton Gamma Ray Observatory, and the main result it found was that most γ-ray pulsars show double-peaked light curves and a power law spectrum with a high energy cutoff. Still, it was not possible to clearly discriminate between the different models, which predict different kinds of cutoffs, because of the limited sensitivity at the highest energies of the instrument that did not allow to fully explore the range where the cutoffs should be observed. The

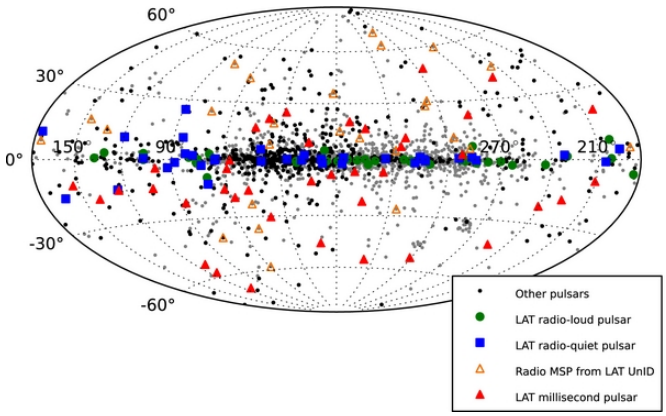

Figure 3.3: Galactic distribution of the pulsars discovered by *Fermi*-LAT during the Second Pulsar Catalog, divided by category. Taken from [56].

presence of two peaks in the light curve was an important feature in testing how the models for γ-ray emission could reproduce it. In general, Polar Cap models prefer to have nearly aligned rotators, while the opposite is true for Outer Gap models; the Slot Gap model, instead, could be adapted to several inclination angles of the magnetic axis with respect to the rotation one.

The turning point for γ-ray pulsars was the launch of *Fermi*-LAT in 2008. In the first year of operations, it detected approximately 50 pulsars and, among them, some Millisecond Pulsars, which were not expected to be γ-ray emitters given their age. The spectra of all the discovered pulsars could be fitted with a power law with an exponential cutoff, meaning that the Polar Cap model (that predicts a super-exponential cutoff, see § 3.2.1) should be probably ruled out. The Second Pulsar Catalog of 2013 [56] collected $\sim$120 γ-ray pulsars (Figure 3.3) and identified three main classes of objects: young radio-quiet, young radio-loud and millisecond pulsars. Moreover, it reinforced the results of the previous Catalog. More details on the history of γ-ray pulsars are reported in [57].

3.2.1 Models for the γ-ray emission

As previously reported, particle acceleration takes place in the outer magnetosphere, but the specific site location changes from model to model (Figure 3.4). The most popular theories are:

- **Polar Cap (PC) model**

  It was proposed for the first time by Sturrock in 1971 [59]. According to this model, particle acceleration takes place near the neutron star surface (at a distance lower than one stellar radius) and close to the magnetic poles. The accelerated charges move along the open magnetic field lines and they emit γ rays thanks to curvature

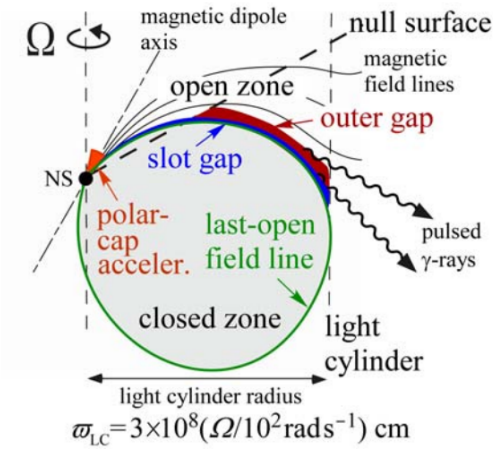

Figure 3.4: Schematic representation of the magnetosphere and the possible regions where acceleration can take place. The acceleration of particles for the Polar Cap model takes place very close to the neutron star surface, in the polar regions of the magnetic field. In both the case of the Slot Gap and Outer Gap models, particles are accelerated far from the neutron star, inside the outer region of the magnetosphere. Taken from [58].

radiation. This model predicts a spectrum of the γ-ray radiation characterised by a power law emission with a sharp super-exponential cutoff at energies of a few GeV. Recent observations tend to rule out the PC model in most of the cases because the predicted sharp cutoff has not been observed (one example for the Crab pulsar is shown in Figure 3.5) and, moreover, the model has some problems explaining both the origin of the double-peak pulse profiles of most pulsars and the separation between the two peaks (Figure 3.6).

- **Slot Gap (SG) model**

  As previously reported, the results of COS-B led to the development of new models to explain the observed γ-ray emission. The first one was the Slot Gap model, theorised by Aarons in 1983 [61]. It was developed as an extension of the Polar Cap model, based on the previous studies by Scharlemann et al. [62], who were able to prove that a large potential gap could be present close to the last open magnetic field lines (Figure 3.4). Aarons proposed that particle acceleration could happen in this region. When compared to the PC model, in this scenario, particle cascades are produced at a larger distance from the neutron star surface and can reach higher energies.

- **Outer Gap (OG) model**

  The Outer Gap model was proposed by Cheng et al. in 1986 [63]. They proved that a low-latitude vacuum gap can exist and its boundaries are defined by the

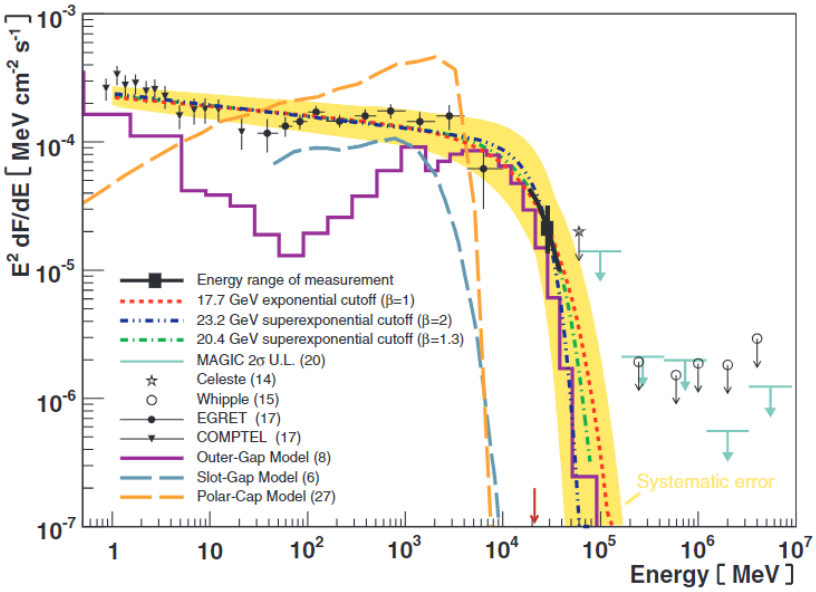

Figure 3.5: Crab pulsar spectrum, taken from [60]. In the plot are reported the flux points from different facilities, along with the three best-fit functions (blue, red, and green lines) and PC, OG, and SG models curves (orange, purple, and blue lines). From this spectrum, it is clear that the Polar Cap model cannot explain the emission from the Crab.

last closed field line, the so-called *null surface* (defined by the equation $\mathbf{\Omega} \cdot \mathbf{B} = 0$ and where the Goldreich-Julian density changes sign), the light cylinder, and an open magnetic field line which is limited by pair creation (Figure 3.4). In this case, emission takes place far from the surface, where the magnetic field is weaker than around the polar caps, and the model predicts a power law trend with an exponential cutoff. The OG model and its extensions can reproduce the typical double-peaked profile of the vast majority of γ-ray pulsars (Figure 3.6). This is one of the reasons why they are the most promising theories to explain the γ-ray emission from pulsars, even though they are not able to fully explain all the features of the γ-ray pulsars' spectra.

- **Wind model**

  Another possibility is that the acceleration takes place in the wind zone outside of the pulsar magnetosphere, according to the model by Aharonian that was developed to explain the emission of the Crab pulsar above tens of GeV [65]. The mechanism at the basis of the VHE emission would be the Inverse Compton scattering by the "cold" ultra-relativistic wind: the X-ray photons, either produced by the magnetosphere or by the neutron star surface, are upscattered by the ultra-relativistic electrons and positrons of the wind. This model, however, still has some

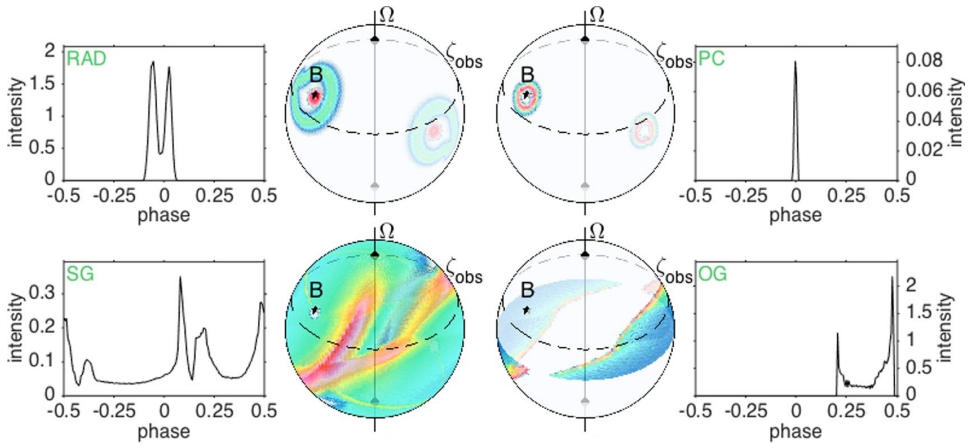

Figure 3.6: Predictions on the pulse profile for different theoretical models (Polar Cap, Slot Gap, and Outer Gap). RAD stands for "radio model", the classical theory to describe radio emission. Taken from [64].

problems with the definition of the extension of the acceleration region, but some variations (such as a slower and continuous acceleration instead of a quick one) could be applied to fit the observed data.

All the previously listed models are purely analytical and they were the most commonly adopted ones due to the limitations in terms of computational time of the simulated models. In the last decade, thanks to the huge improvements in technology, Particle-in-Cell (PIC) simulations have been able to prove the existence of some regions where the electric field is screened and where particle acceleration can take place. These regions are known as *current sheets*, since particle flow along them, and the ones crossing the spin equator of the neutron star are dubbed *separatrixes* due to the fact they separate the magnetic field lines of the two opposite poles. These models are still time-consuming and new technologies are needed to improve them.

In order to carry out a complete study on the VHE emission from pulsars, good quality data of up to 100 GeV, or more, are needed. For now, this can only be accomplished for two main γ-ray pulsars, the Crab and the Vela, even though for the latter the results are yet to be published. Nevertheless, with the development of the CTAO, more pulsars will be observed and, likely, the number of sources that can be analysed in depth in the VHE will increase.

3.3 Geminga

Geminga (RA=06h 33m 54.15s, DEC=+17° 46' 12.91"), also known as PSR J0633+1746, is a radio-quiet γ-ray pulsar located in the Gemini constellation at a distance of $\simeq$ 157

pc, according to Caraveo et. al. [66], or of $\simeq 250$ pc, as obtained by Faherty et. al. [67]; the two measurements were performed independently with two different instruments, even though they were both based on parallax observations. Its period is P=237 ms, with a derivative of $\dot{P} = 1.1 \cdot 10^{-14}$ s/s, and the estimated characteristic age is ∼300 ky, making it one of the most interesting examples of a close middle-aged γ-ray pulsar.

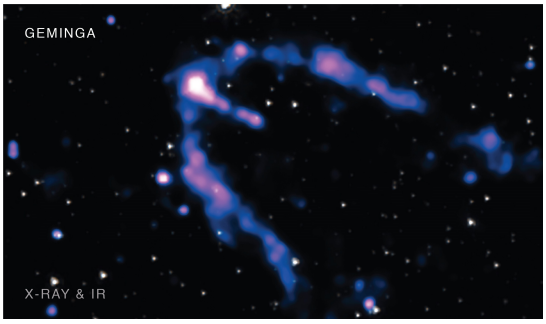

Figure 3.7: Picture of Geminga obtained by combining X-ray data from Chandra (the blue-purple emission, with lighter colours pointing at a higher intensity in the X-rays) and IR data from Spitzer (the background stars of the field of view). Source: `https://www.nasa.gov/chandra/images`

3.3.1 History of the detection

Geminga was first detected in 1972 by SAS-2 as a strong but unidentified γ-ray source called γ195+5 [55]. Due to the instrument limitations, it was not sure if the emission came from a compact or an extended object. Only many years later and thanks to the observations carried out by more advanced satellites, researchers were able to prove the emission was coming from a compact source [68, 69]. Still, the nature of this object was unknown.

For a decade, no clear multiwavelength counterpart was found. A first hint of an X-ray counterpart came from the detection of a nearby source detected both by UHURU and HEAO-1, even though no strong associations with γ195+5 had been found. Indeed, in the latter case, the confidence error box was of the order of 1.4 deg^2 and the X-ray counterpart was compatible only at 9% with the γ-ray source [70]. Finally, in 1983, the instruments on board Einstein Telescope registered the signal coming from a soft X-ray source, identified as 1E0630+178, compatible with the position of the object observed by its predecessors (the 90% confidence regions were of the order of 3") and without any optical counterpart [71]. From the studies of the thermal emission, the distance was estimated to be of the order of hundreds of pcs, one kpc at most.

After the detection of this possible X-ray counterpart of Geminga, a more accurate search for the optical one began. The first candidate, named G, was found with the Canada-France-Hawaii Telescope (CFHT), but it was soon discarded in favour of two

fainter objects dubbed G' and G''. The study of the colours of these optical sources was fundamental in identifying the counterpart of Geminga: while G and G' did not show any particular characteristic, G'' seemed to be bluer than the others. Additional studies on the colour of G'' confirmed that it was the best candidate for the optical counterpart of Geminga. Because of the analogies with the Vela pulsar in the luminosity values of the optical, X-ray and γ-ray bands, researchers proposed that 1E0630+178 could be a pulsar, even though they did not detect any radio signal [72].

The combined results of ROSAT, operating in the X-ray band, and EGRET, focused on the γ rays, proved once and for all that 1E0630+178 was a neutron star and the X-ray counterpart of Geminga, which became the first radio-quiet pulsar discovered through its high energy emission. ROSAT detected a soft X-ray pulsed emission with a period of 237 ms [73] and, thanks to EGRET observations [74], the most accurate measurements of the period and its derivative were obtained: $P = 237.0974531$ ms and $\dot{P} = 1.0976 \cdot 10^{-14}$ s/s. From these, the estimates for the characteristic age, magnetic field and spin-down power could be obtained: $\tau \sim 3 \cdot 10^5$ yr, $B \sim 1.6 \cdot 10^{12}$ G, and $\dot{E} \sim 3.5 \cdot 10^{34}$ erg/s.

In the same years, the study of the proper motions of G'' allowed Caraveo et al. to constrain the distance of Geminga to $d = 157^{+59}_{-34}$ parsecs. Furthermore, by combining the information on the proper motions and the γ-ray observations, it was also possible to confirm that the object G'' was indeed the optical counterpart of Geminga [66].

Focusing in particular on the X-ray and γ-ray emission, it was possible to observe the change of the pulse profile with the energy, as Figure 3.8 depicts. In the soft X-rays, where the emission is linked to thermal radiation, the pulse is single and broad. When the emission becomes harder, transitioning towards a non-thermal synchrotron, the pulse tends to split in two. In the γ-rays, instead, the two peaks are well defined and separated by a $\Delta\Phi \simeq 0.5$ and the emission can be explained with curvature radiation.

The last electromagnetic band where Geminga was detected is that of the VHE γ rays. The very first results by VERITAS [76] and MAGIC [77] Collaborations resulted in a non-detection of any emission above 100 and 50 GeV, respectively. However, ground-based facilities, such as HAWC [78], discovered a TeV halo around Geminga. The breakthrough happened in 2020 when MAGIC Collaboration detected a pulsed emission in the energy range 15-75 GeV, and Geminga became the third VHE pulsar ever discovered by IACTs[2]. The results of this paper are presented in § 3.3.2.

After forty years since the first detection of this pulsar, no radio signal has been detected from it. A recent study of its pulsed radio emission yielded an upper limit for the average flux density of 0.4-4 mJy at a frequency of 111 MHz [80]. This makes Geminga a classic example of a radio-quiet γ-ray pulsar. For more details on the history of the detection, refer to [81].

[2]A preliminary result on a fourth VHE pulsar, PSR B1706-44, has been obtained by H.E.S.S. Collaboration in 2019, but the significance of the signal was below the 5σ threshold usually adopted for the detection of a source (§ 4.3.1). Source: [79].

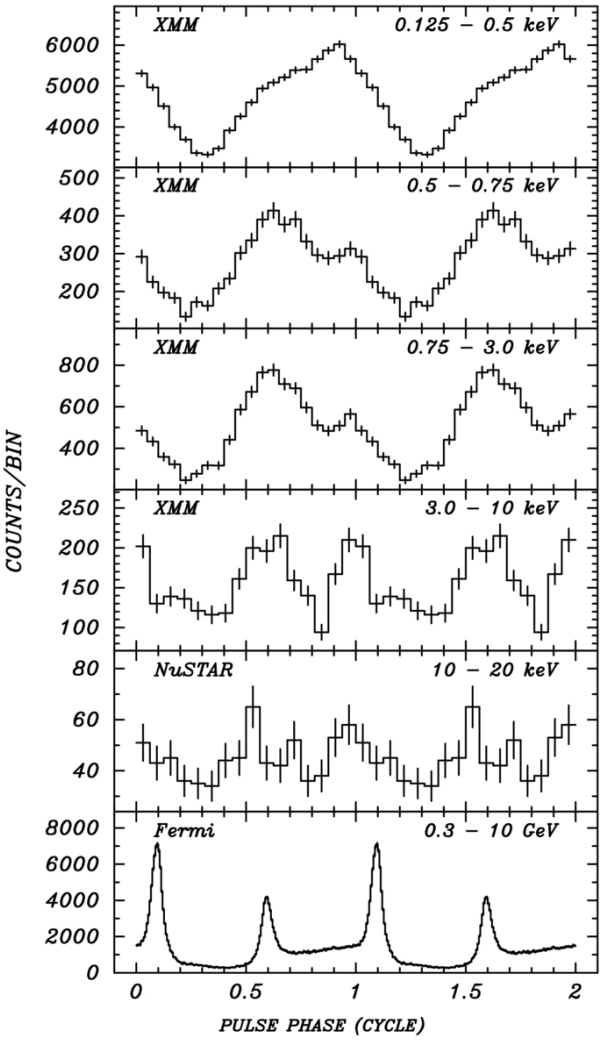

Figure 3.8: Geminga pulse profile in three ranges of the soft X-rays (detected with XMM-*Newton*), in the hard X-rays (detected with NuSTAR), and in the γ rays (detected with *Fermi*-LAT). It is clear how the pulse profile and location change depending on the energy range, which is linked to different emission mechanisms. Taken from [75].

3.3.2 Current picture of the γ-ray emission

The γ-ray emission from Geminga is characterised by a two-peaked light curve, where the first peak is known as P1 and the second as P2, with a phase separation of the order of 0.5. The first spectra obtained after EGRET detected the γ-ray pulsed emission featured a sharp cutoff at energies of the order of 2 GeV that was interpreted as evidence of curvature radiation [82]. In addition, they also observed that the luminosity ratio P1/P2 was decreasing when energy increased. Similar conclusions were found by analysing the very first *Fermi*-LAT data, but better results were obtained when a larger data sample was fitted with a power law with a sub-exponential cutoff model [83]. Also, the decreasing trend of P1/P2 with energy was observed. The Second Pulsar Catalog of 2013 reinforced these results, implying that acceleration probably takes place in the outer gap sites rather than near the magnetic poles.

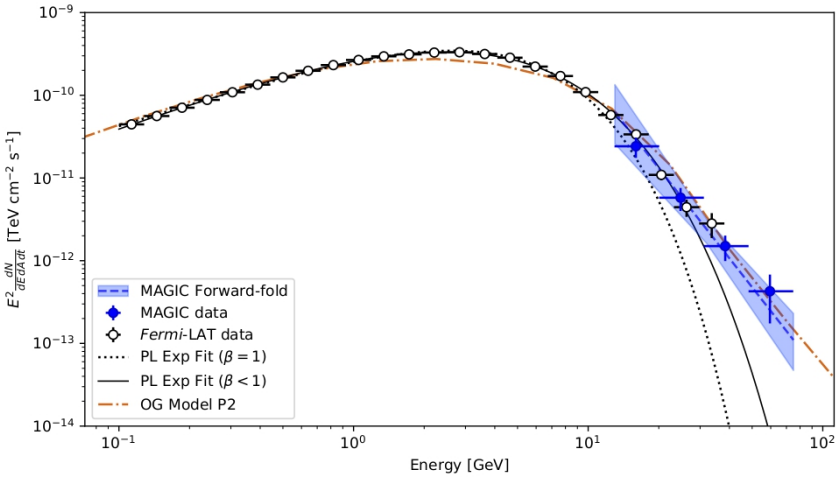

Figure 3.9: P2 spectrum of Geminga including MAGIC (blue points) and *Fermi*-LAT (black points) observations. In the plot, are also reported the best-fit results for the different spectral models that have been tested: the power law on MAGIC only (blue dashed line with the associated error region), the power law with exponential cutoff (black dotted line) and the power law with sub-exponential cutoff (solid black line). The orange dashed line, instead, represents the modified Outer Gap model compared to the observations.

As reported in § 3.3.1, MAGIC Collaboration detected Geminga for the first time in the VHE in 2020 [84]. They observed the pulsar for a total of 80 hours of good-quality data with a cut in the zenith at 25° to keep the energy threshold as low as possible. They were able to detect P2 in the energy 15-75 GeV energy interval with a significance of 6.3σ, while P1 was not detected because the significance of the signal was only 0.3σ. Then, they performed a fit of P2 data using a power law spectral model that returned a best-fit value of the index of $\Gamma = 5.62 \pm 0.54$. To carry out a more detailed statistical study of the possible spectral models, they also performed a joint likelihood fit of MAGIC

and *Fermi*-LAT data and they were able to rule out both the power law with exponential and sub-exponential cutoff. From the joint fit of MAGIC and *Fermi*-LAT data above 10 GeV, they also found that the log-parabola spectral model is not preferred over the simple power law.

Lastly, they compared their observation with the theoretical predictions of a modified version of the Outer Gap model. Curves with a different inclination angle between the magnetic field and the rotational axis, a different magnetic dipole, and a different viewing angle were tested. The most compatible curve is shown in Figure 3.9 along with the other tested models. The main issue with the OG solution they used is that it under-predicts the *Fermi*-LAT flux at energies of a few GeV.

All in all, MAGIC Collaboration's results proved that the best model to fit the data in the energy range [15, 75] GeV was a power law, highlighting the presence of Inverse Compton scattering and proving that classical pulsar models (§ 3.2.1) should be modified to explain the VHE emission of Geminga. However, more studies are needed to shed light on the process at its basis.

Chapter 4

LST-1 data analysis of Geminga observations

In this Chapter, the process of the LST-1 data analysis, both at the low and high level, is discussed in detail, starting from the selection of the sample and going through the data reduction chain. The main software libraries that have been employed are version v0.9.13 of `cta-lstchain` [85], version v0.20.1 of `gammapy` [86], and version v0.9.3 of `PINT` [87], a recently developed Python package for high-precision pulsar timing analysis.

4.1 Observations and data selection

Geminga was first observed by LST-1 at the end of December 2022, and regular daily observations were performed in the following months. The telescope was programmed to take data with the *wobble mode* [88], a technique commonly used by IACTs that has the main advantage of allowing the telescope to observe at the same time the source (located at the centre of the *ON region*) and the background (inside the *OFF region*[1]). For LST-1, as for other IACTs, the wobble mode consists of pointing the telescope in such a way that the source is located at $\sim 0.4^\circ$ from the centre (Figure 4.1). Then, every $\sim$20 minutes, the position of the source is rotated to another part of the camera and the observation begins again. In this way, it is possible to reduce the potential inhomogeneities of the camera.

The analysed sample of observations starts on the 20th of December 2022 and ends on the 24th of March 2023, for a total amount of 41.50 hours of collected data, corresponding to 146 wobble runs. A run can be considered the standard unit of measure for observations, equivalent to a pointing of $\sim$20 minutes. Every run can be divided into sub-runs, which include $\sim$53000 events, i.e. between $\sim$6 and $\sim$10 seconds of observations.

[1] Usually, more than one OFF region is used to better estimate the background signal.

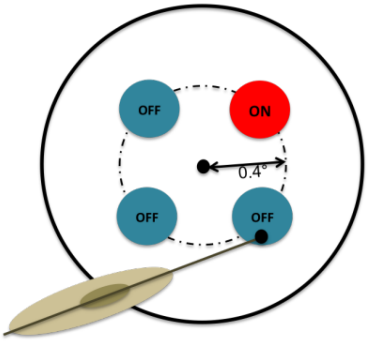

Figure 4.1: Example of the setup of a wobble mode with three OFF regions. Taken from [89].

4.1.1 Data selection process

For the selection of good-quality data, the standard `cta-lstchain` procedure, which starts from the datacheck files of the DL1 stage, has been adopted. These files are produced after the stage where the raw data coming from the camera are converted into DL1 and their purpose is to allow the users to inspect the quality of the observations before starting the data reduction chain. They consist of five tables:

- `runsummary`, including one row for each run of the selected day with the values of different parameters related to it, such as the ID, time duration, altitude of the telescope, and others;
- `pixwise_runsummary`, with one row for each run containing the information on some pixel-wise run-averaged quantities. Examples of quantities of this table are the fraction of all pulses brighter than 10 p.e. (or 30 p.e.) in cosmics (or pedestals), the mean pixel charge (in p.e.) in the flatfield events, or the standard deviation of the pixel charge in interleaved flatfield events (in p.e.);
- `cosmics`, `flatfield`, and `pedestals`, which are made of one row per each sub-run and include the same information as the `runsummary`, but related to the three different kinds of events.

All the DL1 datacheck files missing one or more of the tables were excluded by the analysis since it was not possible to thoroughly study the quality of the acquired data during those runs. When these tables are missing it means, in general, that some problems with the data acquisition were present; for example, the `flatfield` events can be missing if the calibration box is not working properly.

The main steps of the data quality selection process can be summarised as follows:

1. Select only the runs related to the object of interest by picking out the wobble pointings at a certain angular distance from the source position;

2. Apply a zenith angle cut depending on the energy threshold requested by the analysis (see § 4.1.1.1 for more information on how the zenith cut affects the data sample);

3. Study the Moon and Sun position to check if there is some contamination of the signal caused by their light;

4. Remove the runs with both too high Night Sky Background and Moon contamination by applying a cut in the camera-averaged pedestal charge standard deviation, which is the parameter used to study the level of background;

5. Remove the runs for which telescope or weather problems were noticed by applying cuts on the cosmics rates and the average pixel rates;

6. Check the behaviour of other parameters, such as the rate of interleaved events or the intensity of the muon rings[2], to see if some other problems are present.

For the data analysis of Geminga, standard values of the cuts were adopted. In particular:

- an angular distance within the range 0.35°-0.45° to select the wobble runs;
- a maximum pedestal charge standard deviation of 2 photoelectrons (p.e.) because the FoV around Geminga is not particularly bright. The standard value is taken as 2 p.e. and not zero because some background signal must always be included in the selection. For brighter fields, higher values must be adopted depending on the value of the NSB;
- a cosmics rate above 3000 events/s (Figure 4.2);
- an average pixel rate of the cosmics events with pulses above 10 p.e. of 30 events/s (Figure 4.3a) and of 4 events/s for pulses above 30 p.e. (Figure 4.3b). These are additional parameters used to assess the quality of the data and to check if additional problems with the telescope are present.

No particular problems appeared when the muon rings and the interleaved events were analysed (Figure 4.4). Concerning the mean zenith angle of the observations, a cut at 25° was chosen; more details are reported in § 4.1.1.1. After applying all these cuts, the sample was reduced to 23.48 hours of good-quality data.

[2]The typical image on the camera of a muon shower is a ring [90].

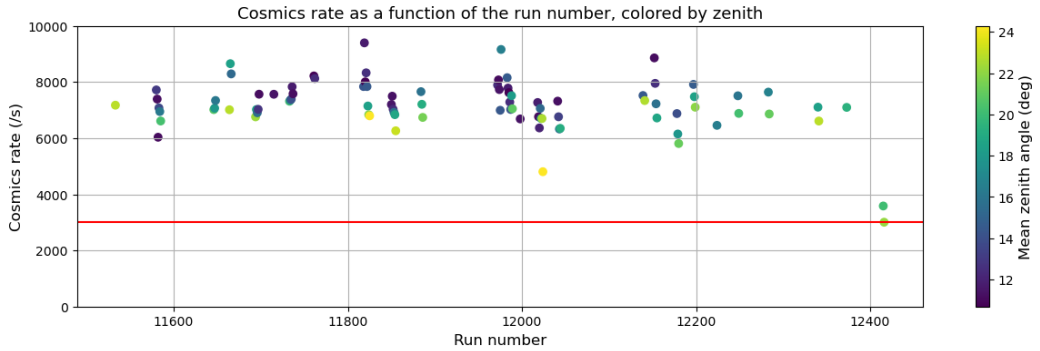

Figure 4.2: Cosmics rates as a function of the run number, coloured by mean zenith angle. The selected cut of 3000 events/s is highlighted in red. The last runs show a lower rate due to their shorter duration caused by some errors of the telescope, and they were excluded with the following cuts.

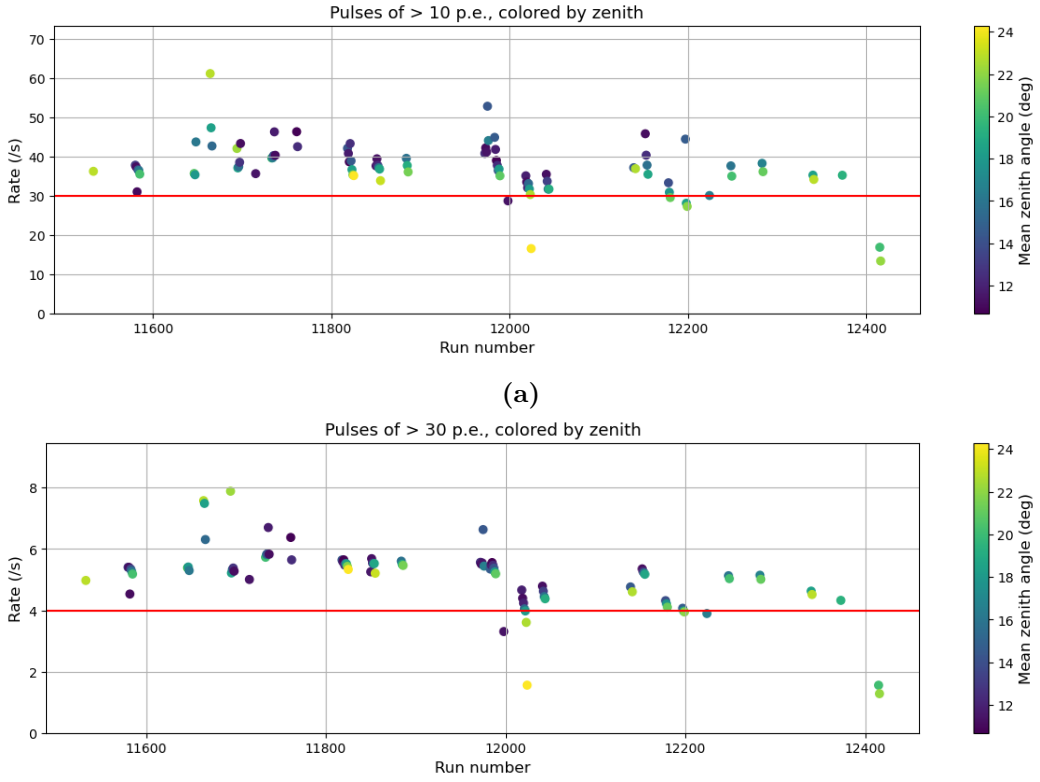

Figure 4.3: Average pixel rate for pulses above 10 p.e. **(a)** and above 30 p.e. **(b)** as a function of the run number, coloured by mean zenith angle. In red it is highlighted the selected cut of 30 events/s for **(a)** and of 4 events/s for **(b)**.

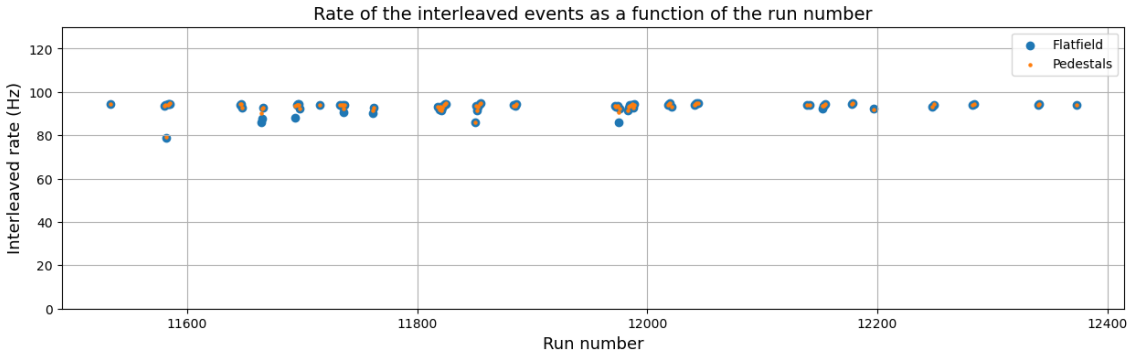

Figure 4.4: Rate of the interleaved events (flatfield events in blue and pedestals in orange) as a function of the run number. Both are correctly distributed around 100 events/s (100 Hz).

4.1.1.1 Zenith cut

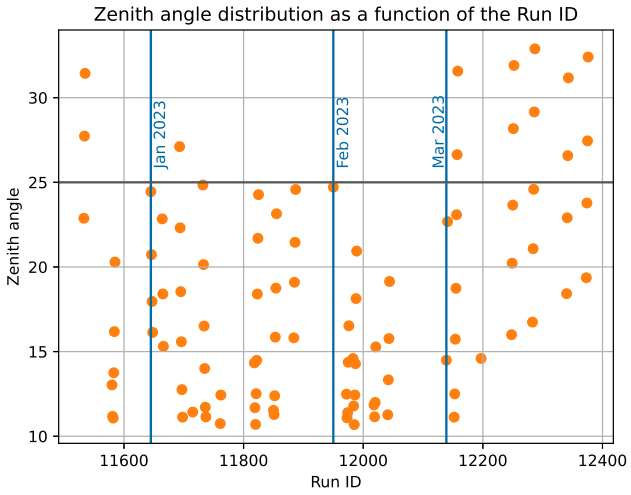

Figure 4.5: Distribution of the mean zenith angle as a function of the run number before the cut in zenith. The vertical lines pinpoint the month of the observations, the horizontal line highlights the 25° zenith cut subsequently applied to the data.

The most important cut for the data selection process is the one in the zenith angle, mainly because it affects the γ-ray events that IACTs collect from the ground. If a shower is observed at a large zenith distance, i.e. closer to the horizon, then the particles must cross a larger portion of the atmosphere and this implies that the shower maximum shifts at higher altitudes from the ground and the radius of the Cherenkov pool increases, leading to a lower photon density. Conversely, the geometrical radius is smaller for low

zenith showers, but the photon density is higher. All in all, the effect is an increase in the energy threshold of the detected particles with increasing zenith angles.

In particular, the dependence on the rate on the zenith angle goes like $\cos^{\alpha}(zd)$, where α is a generic exponent usually dependent on the considered zenith range, and this is why the slight decrease in the rates as the zenith angle increases is an expected trend.

For the study of Geminga, a first cut at 35° in zenith was applied. After studying the mean zenith angle distribution of the data (Figure 4.5), it was clear that cutting at 25° would not affect the results since the number of runs above that value was not particularly significant. Moreover, by lowering the zenith angle of the observations, the energy threshold of the observations would also be reduced.

4.1.2 Additional issues

After completing the standard quality selection process, the data sample had to be further reduced because of two extra issues that have been encountered: a humidity patch on the camera cover and a time mismatch problem in March 2023 data.

4.1.2.1 Humidity patch on the camera

The first issue was the presence of a humidity patch on the plexiglass cover of the LST-1 camera, which affected all the runs from the 20th to the 26th of February 2023. Figure 4.6 shows the evolution of this patch for one of the interested nights.

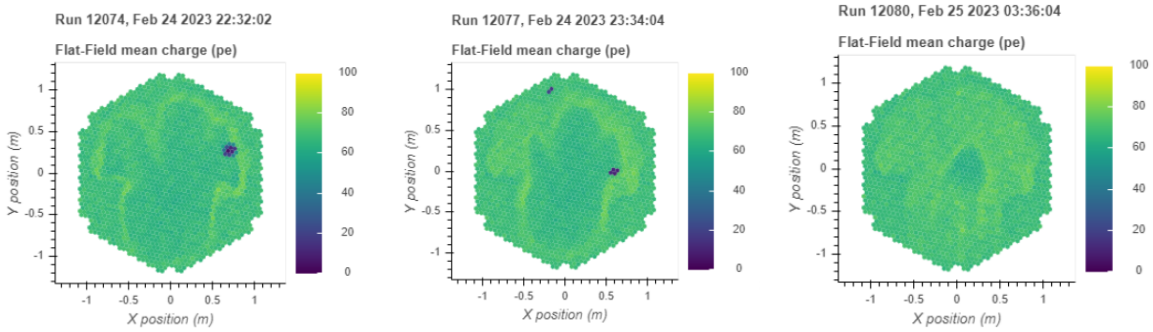

Figure 4.6: Evolution of the humidity patch during the night of the 24th February 2023. The color bar on the right represents the value of the mean charge for the flatfield events.

It was not possible to detect this issue while performing the quality selection because the telescope was correctly operating, thus the involved runs were excluded from the final list by hand, leaving a 21-hour data sample for the analysis.

4.1.2.2 Time mismatch

The second issue that affected the data and that was not possible to detect with the quality selection process was a time mismatch in the time column of the event list. This problem was caused by a power cut in the observatory at the beginning of March 2023 that generated a loss of synchronization between the telescope clocks that define the photon arrival times. The mismatch was solved at the beginning of April 2023 with a reboot of the White Rabbit device responsible for time synchronization, but all the affected data had to be corrected.

The mismatch was first noticed because of an unusual trend in the significance of the signal and the excess counts (computed as the difference between the observed counts and the level of background obtained from the OFF region) after the end of February. An example of the peculiar trend of the excess counts for the second peak of the phaseogram is depicted in Figure 4.7a: it is clear that, after ∼16 h, i.e. the number of hours observed until the 14th of February 2023, the trend is constant as if the telescope did not observe any signal. Because the origin of the unusual behaviour of the signal was unknown at the beginning of the analysis process, a first study using only the data until the 14th of February 2023, the last day when the humidity patch was not present, was performed. The total amount of hours of the data sample was 16.4 hours.

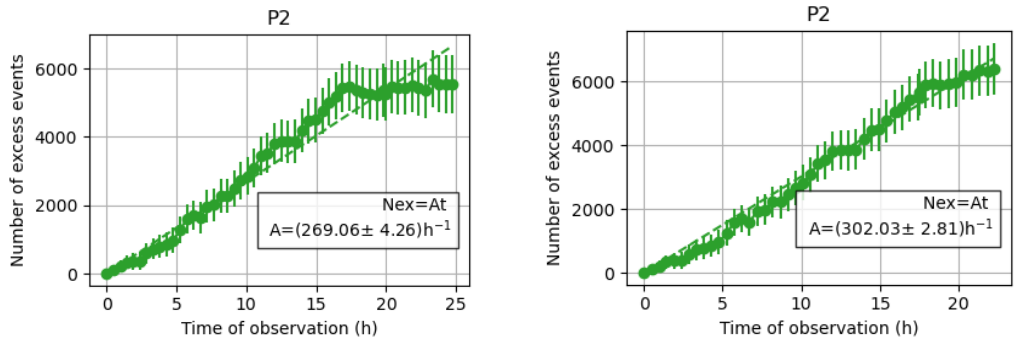

(a) **(b)**

Figure 4.7: Trend in time of the number of excesses for P2, before **(a)** and after **(b)** the correction for the time mismatch.

Once the nature of the problem was found and the mismatch was computed to be $\Delta\tau = -76.039$ ms, it was possible to correct the time column of the events and perform the analysis on the complete dataset. Figure 4.7b shows the same excess counts trend as a function of time for P2 as Fig. 4.7a but after applying the correction: the trend after 16 hours is not constant anymore and it follows the expected linear increase with time.

4.2 Low-level analysis

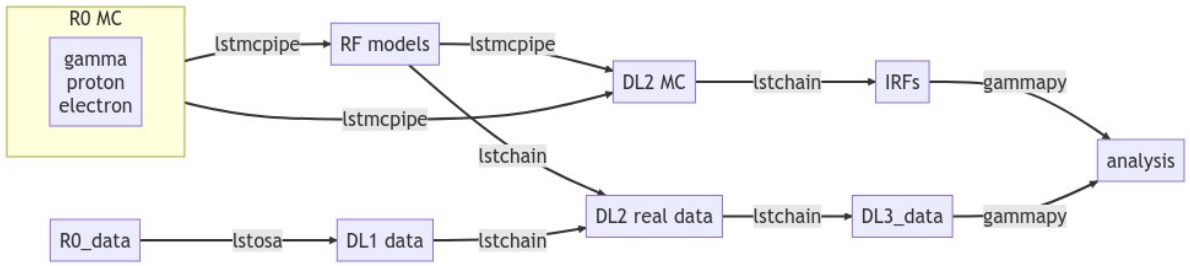

Figure 4.8: Pipeline for LST-1 low-level data reduction, along with the software used for the steps. All the stages until the DL2, for both real and simulated data, are performed by the LST On-Site Analysis `lstosa` [91]. Source: `https://cta-observatory.github.io/cta-lstchain/`

As anticipated in Section 2.4.1, each step of the data reduction chain is associated with a specific data level. The low-level chain (Figure 4.8) begins with the DL0 files, a calibrated and gain-selected reduced version of the data directly coming from the camera DAQ system, and it continues with the DL1 files. This data level is split into two sub-levels: DL1a and DL1b. The formers include the integrated charge and peak position of the waveform for each of the 1855 camera pixels, along with the estimated arrival time for the photons. Then, by applying a parametrization of the images inside DL1a files, one can obtain the final DL1b. The standard parametrization was formulated by Hillas [92]: the image of a γ-initiated shower can be represented as an ellipse and, from the study of the most important parameters of its shape, listed in Figure 4.9, one can reconstruct the direction and the energy of the primary γ ray.

To fully reconstruct the image, one needs to introduce an additional parameter called *gammaness*, representing the probability of an event to be γ-originated rather than of hadronic nature. The gammaness definition requires using Random Forest (RF) models on DL1 data, which must be trained and tested on Monte Carlo simulated data. Both simulated hadrons and γ rays are used to train the RF (MC Train chain), and then the trained models are applied to different simulated γ rays to test their performances (MC Test chain) and get the simulated DL2 files. The same RF models are applied to the DL1b files to derive the data DL2, including the reconstructed energy, direction and gammaness of each event and the DL1b image parameters. For LST-1 analysis, the trained models are provided by `lstMCpipe` [93].

To complete the DL1 to DL2 stage, one can choose between two different approaches:

a) **Source independent**

The real sky position of the source is not known, thus the parametrization will be based on the square of a parameter called ϑ that represents the angular distance

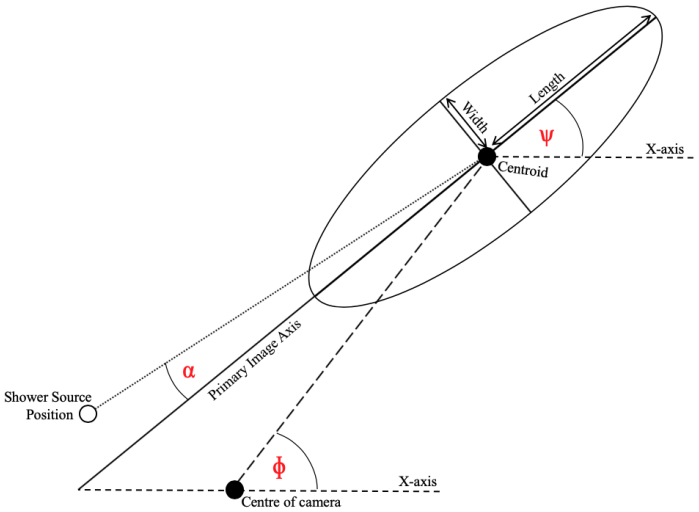

Figure 4.9: Basic image parameters. The ellipse is the fit of the γ-ray event, its width is a measure of the lateral development while its length is connected to the longitudinal development. The centroid (or Centre of Gravity, CoG) is the average centre position, Ψ is the rotation angle of the ellipse with respect to the x-axis, and Φ is the polar coordinate of the CoG. The parameter α is the angle between the assumed source position and the image axis. Source: `https://github.com/cta-observatory/descriptive-hillas`

between the reconstructed and the real positions of the source. This will be the standard approach for CTA analysis.

b) **Source dependent**

In this case, the parameter α, which is based on the assumption that the source position in the sky is known, is used. α is defined as the angle between the ellipse axis and the source position. This approach is usually adopted for point-like sources and it is the approach chosen for the analysis of Geminga.

The last step of the low-level analysis is the production of the event list of the γ-ray candidate events, i.e. the DL3 files. To this goal, one has to define some efficiency cuts based on the level of accuracy in discriminating between cosmic and γ rays that one wants. The same cuts are applied to the data DL2 to obtain the data DL3 and to the simulated DL2 to get the Instrument Response Functions (IRFs). They provide a mathematical description that links the measured quantities of an event to the physical quantities of the incident photon. IRFs include:

- **Point Spread Function**: it describes the probability of measuring a γ ray of a given true energy and true position at a certain reconstructed position;
- **Effective Area**: it is proportional to the γ ray efficiency of detection and it is computed as a function of the true energy and position;

- **Energy Dispersion Matrix**: it is the ratio of the reconstructed energy over the true energy as a function of the true energy (see § 4.3 for more information on the two energies).

The data DL3 together with the IRFs make up the final DL3 stage.

4.2.1 DL1 to DL2

Even though `lstosa` provides the DL2 files to the users, the low-level data reduction for Geminga started from the DL1 stage of the selected runs. As previously stated, it is necessary to rely on Monte Carlo (MC) simulated showers and RF models to obtain the final list of γ-like events. The RF models are trained on a particular declination line in the sky because all the sources sharing the same line have the same path in the sky. Then the contribution of the Night Sky Background is added by studying its effect on the emission of the observed source. For this study, the trained models were obtained for the declination line at 22.76°, with the NSB tuned on Geminga, and using a source-dependent configuration (production ID: `20230124_src6_dec2276_tuned`). After defining the RF models to apply to the DL1 files, the script to produce the DL2 files provided by `cta-lstchain` was used.

4.2.2 DL2 to DL3

This stage is divided into two parallel sub-steps: the first one is producing the Instrument Response Functions (IRFs) from the MC simulated DL2 data, then the IRFs are added to the data DL2 to obtain the DL3 stage.

4.2.2.1 DL2 to IRF

The simulated DL2 data coming from the MC Test chain, provided by `lstMCpipe` are obtained assuming particular telescope pointings, called *nodes*. The complete list of the nodes with their zenith and azimuth angles is reported in [94]. For the production of the IRFs, one has to take into account both the zenith and the azimuth of the telescope pointing because the shower parameters are influenced by the geomagnetic field of Earth (dependent on the azimuth angle) and by the airmass (a parameter that measures the amount of atmosphere crossed by the light and it is dependent on the cosine of the zenith angle). The nodes are commonly displayed in a plane where the y-axis is the cosine of the zenith angle and the x-axis is the sine of the parameter δ. The latter is defined as the angular separation between the magnetic field component at the telescope location and the position where the telescope is pointed; the magnetic field components for the Observatorio del Roque de los Muchachos were computed for the 29th of November 2021

Table 4.1: Zenith and azimuth angles for the nodes used in the analysis.

Node ID	Zenith (deg)	Azimuth (deg)
Node 1	10.0	102.2
Node 2	10.0	248.1
Node 3	14.98	175.2
Node 4	23.6	100.8
Node 5	23.6	259.3
Node 6	32.1	248.1

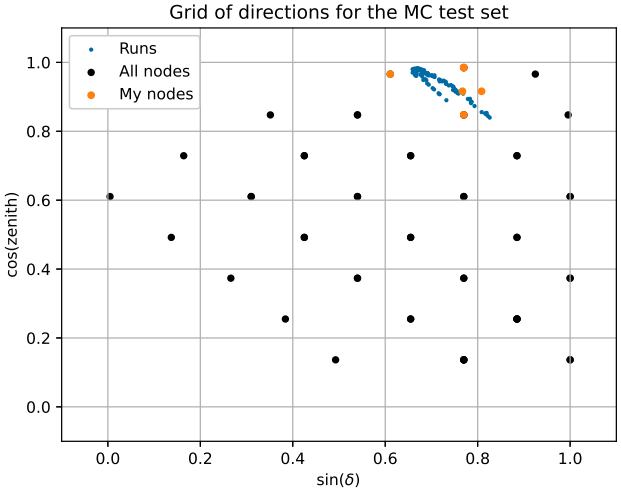

Figure 4.10: Distribution of all the available Monte Carlo nodes (with the ones used in the analysis highlighted in orange) and of the runs in the $\sin(\delta)$-$\cos(zd)$ plane. Only five out of six of them are visible because of a superposition in this plane of the first two nodes.

and at 10 km a.s.l. through an online calculator[3].

All the available nodes for LST-1 are shown in Figure 4.10 (black points) along with the ones selected for the analysis of Geminga (orange points) and the runs (blue points). In total, six nodes have been selected and their coordinates in zenith and azimuth are reported in Table 4.1.

Then, for each of the nodes, the dedicated `cta-lstchain` script for the production of IRFs was used, adopting a source-dependent approach and applying the following cuts:

- intensity cut above 50 p.e.: this was necessary to make the simulated data more realistic by considering some level of background signal;

[3] `https://www.ngdc.noaa.gov/geomag/calculators/magcalc.shtml`

- energy-dependent cuts applied to the angle between the ellipse axis and the source position (α in Figure 4.9) and gammaness based on a 70% cut in efficiency.

In particular, the cut in efficiency was obtained from the MC Test simulations and represents the fraction of the γ-like events that the Random Forest models are able to recognise. An x% efficiency means that x% of the simulated γ rays will be identified by the model as so. Given the definition, a reliability-versus-completeness issue is present: a lower efficiency implies that the RF will recognise more events, but the data will have lower quality (more contamination by hadronic events); a higher efficiency, instead, means fewer events will be identified but their quality will be higher. The value of 70% is always taken as the standard efficiency in γ-ray analysis, but different percentages can be adopted to test the systematics of the analysis.

4.2.2.2 DL2 to DL3

To obtain the final list of the γ-like events, the DL3 files, one has to apply to the DL2 files exactly the same cuts that have been used for the IRF production, so that the two will be compatible and the response of the instrument will be correctly included in the production of the final list.

In this regard, the runs have been divided into groups to match them with the right IRF. The chosen criterion for the division was the minimum distance in the $\sin(\delta) - \cos(zd)$ plane. For every run, the distance from each one of the six selected nodes has been computed and, afterwards, the minimum distance between the six was derived. At the end of the process, two of the nodes (nodes 1 and 5) have been discarded since none of the runs was at the minimum distance from them. In the end, the dedicated `cta-lstchain` has been used to produce the DL3 files according to the groups.

4.2.3 DL3 to DL3 pulsar

The last step of the low-level analysis for a pulsar study is to add the column containing the information on the rotation phase, defined as the number of turns completed by the neutron star since a particular reference time, to the DL3 files. To this goal, it is necessary to define a model for the pulsar rotation, i.e. the *pulsar ephemeris*.

The rotational frequency of the pulsar at a generic time t with respect to the initial time t_0 can be described with a Taylor expansion, considering the variation of the period in time:

$$\nu(t) = \nu_0 + \dot{\nu}_0(t - t_0) + \frac{1}{2}\ddot{\nu}_0(t - t_0)^2 + \frac{1}{6}\dddot{\nu}_0(t - t_0)^3 + ... \tag{4.1}$$

From this equation it is easy to derive the phase:

$$\Phi(t) = \int_{t_0}^{t} \nu(\tau)d\tau = \Phi_0 + \nu_0(t - t_0) + \frac{1}{2}\dot{\nu}_0(t - t_0)^2 + \frac{1}{6}\ddot{\nu}_0(t - t_0)^3 + ... \tag{4.2}$$

The pulsar ephemeris is then defined as a set of estimates of $(\nu_0, \dot{\nu}_0, \ddot{\nu}_0, ...)$ at an arbitrary reference time t_0. Some discrepancies between the model and the observations can be present if the pulsar experiences *glitches*[4], but Geminga, being a middle-aged pulsar, has a stable structure and the issue of glitches is not relevant. The parameters inside the ephemeris files can change from pulsar to pulsar, but the most important ones are the initial time t_0 in MJD, the frequency and its derivatives, the position of the pulsar in RA-DEC, and the reference time and frequency in order to have $\Phi_0 = 0$.

The ephemeris file employed for this analysis[5] was kindly provided by Dr. Giovanni Ceribella and it was derived using *Fermi*-LAT data, starting on the 6th of August 2008 and ending on the 30th of April 2023. The file includes the standard parameters of an ephemeris and the values of the second derivative of the frequency as a function of time. These values are usually included when one has to deal with glitches, but for Geminga it is used to reduce the high phase drift which affects the pulsar. Basically, to simplify the computations, "local" ephemerides relative to a time span of about 100 days are smoothly put together to build the total. A complete discussion on how the ephemeris was obtained can be found in Appendix A of [95].

After defining the ephemeris, the phase was computed and added to the DL3 file by using a script of the open-source Python package called `PulsarTimingAnalysis` [96], based on `gammapy` and `PINT`. The very last step of this stage was to build the index file for the final list of runs in order to run the following steps of the high-level analysis with `gammapy`.

4.3 High-level analysis

The high-level analysis (Figure 4.11) performed with the open-software Python package `gammapy` for γ-ray astronomy starts from the list of γ-ray candidate events, the DL3 files, along with their corresponding IRFs. Once a certain geometry for the region of interest in the sky has been chosen, one can extract the signal from that area and perform a reduction by binning the data in energy. To properly perform the binning, two energy axes must be introduced: the true energy E_{true} and the reconstructed energy E_{reco}. This is due to the fact that the instrument is not perfect and, when it measures a certain energy (E_{reco}), the value does not exactly correspond to the real one of the emitted photon (E_{true}). The two axes are also taken into consideration for the next step so that the discrepancies between the real and measured energy values are smoothed during the fit procedure. The binned data define the DL4 stage and the sub-package employed for the reduction is called *Makers*.

[4]Discontinuities in the $P - \dot{P}$ related to sudden decreases of the period. They are more common in young pulsars, where the structure is not fully stable. They can also be related to accretion.

[5]`https://www.mpp.mpg.de/~ceribell/geminga/index.php`

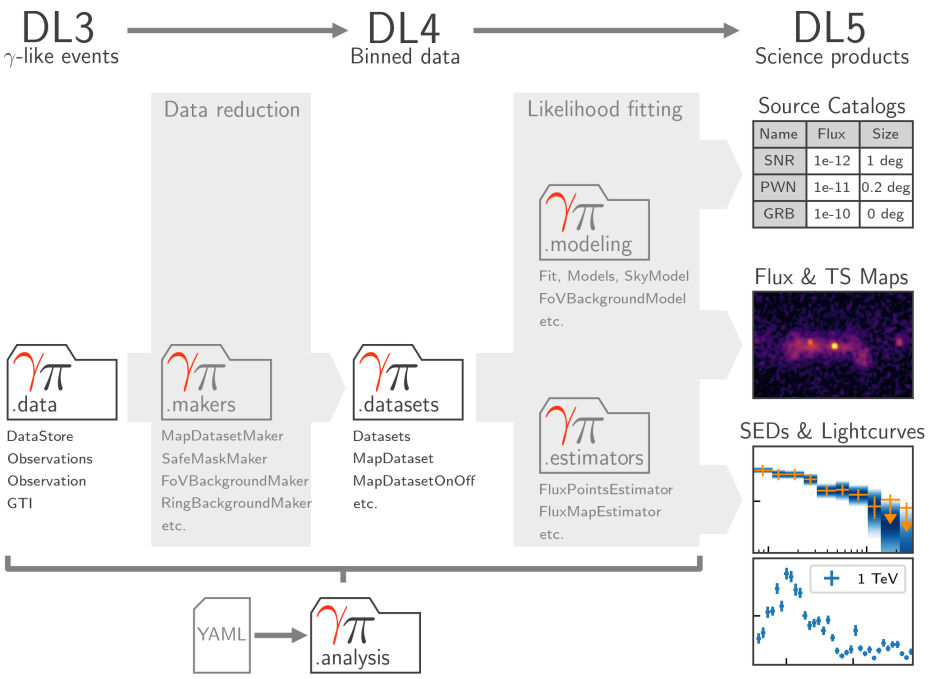

Figure 4.11: Analysis flow and corresponding sub-package (folder icon) structure of `gammapy`. Source: `https://gammapy.org/`.

The founding approach of the last stage (DL4 to DL5) of the high-level analysis is known as the *forward folding method*. It is based on the definition of a certain spectral model with several parameters, which is then convolved with the instrument response to obtain the so-called *folded model*, which can be interpreted as the initial model corrected by the response of the instrument. This is why the axes E_{reco} and E_{true} were defined. Then, the folded model is fitted to the data to obtain the best-fit values of the parameters and the relative correlation matrix. The fitting is based on a likelihood method, which for `gammapy` is the Li&Ma Likelihood (§ 4.3.1), and the sub-packages employed are *Modeling* and *Estimator*, where the last one can be used to estimate the spectral flux points (or their upper limits, if the signal is low) for every energy bin. The final products (DL5) are usually sky maps, Spectral Energy Distributions (SEDs) and light curves, and they can be further analysed with additional statistical tools.

4.3.1 Li&Ma likelihood

The forward fitting in `gammapy` is based on the likelihood ratio test method theorised by Li and Ma in 1983 [97], the so-called *Li&Ma likelihood*. The method is based on the hypotheses testing, for which Wilks's theorem [98] holds. Given an observed sample $X = (x_1, x_2, ..., x_n)$, a set of unknown parameters $\Theta = (E, T) = (\epsilon_1, \epsilon_2, ..., \epsilon_r, \tau_1, ..., \tau_s)$

and the statistical hypotheses $E = E_0 = (\epsilon_{10}, \epsilon_{20}, ..., \epsilon_{r0})$ (the "null hypothesis") and $E \neq E_0$ (alternative hypothesis), the *maximum likelihood ratio* between the two is defined as:

$$\lambda = \frac{L(X|E_0, \hat{T}_c)}{L(X|\hat{E}, \hat{T}_c)} = \frac{P_r(X|E_0, \hat{T}_c)}{P_r(X|\hat{E}, \hat{T}_c)} \tag{4.3}$$

where $L(X|\Theta')$ is the likelihood function of n observed values X given the parameters $\Theta = \Theta'$, i.e. the probability of experimental results X given $\Theta = \Theta'$; $\hat{E}$ and $\hat{T}$ are the maximum likelihood estimates of the parameters E and T, and $\hat{T}_c$ are the conditional maximum likelihood estimates for $E = E_0$ [98]. The theorem states that if $E = E_0$ is true, then the quantity $-2 \ln \lambda$ will follow a χ^2 distribution with r degrees of freedom.

For γ-ray astronomy, the instrument observes the source (ON region) for a certain time t_{on} detecting N_{on} photons, and observes the background (OFF region) for a time t_{off} counting N_{off} photons. One can define the estimate of the number of background counts N_B and the number of source counts N_S as:

$$N_B = \alpha N_{off} \qquad N_S = N_{on} - \alpha N_{off} \tag{4.4}$$

where $\alpha = t_{on}/t_{off}$ and is in general different from one. Then, the two tested hypotheses are the null hypothesis $< N_S >= 0$, i.e. all the observed photons are due to the background, and the actual presence of a signal from an astrophysical source $< N_S > \neq 0$. The maximum likelihood ratio defined in eq. 4.3 becomes:

$$\lambda = \frac{L(X|E_0, \hat{T}_c)}{L(X|\hat{E}, \hat{T})} = \left[\frac{\alpha}{\alpha + 1}\left(\frac{N_{on} + N_{off}}{N_{on}}\right)\right]^{N_{on}} \left[\frac{1}{1 + \alpha}\left(\frac{N_{on} + N_{off}}{N_{off}}\right)\right]^{N_{off}} \tag{4.5}$$

Then the significance of the detected signal can be estimated as:

$$S = \sqrt{-2 \ln \lambda} \tag{4.6}$$

The conventional value of the significance threshold for the detection of a signal in γ-ray astronomy is usually set at a 5σ level: $S > 5\sigma$.

Another application of the likelihood ratio test is to compare two different models to see if one is statistically favoured over the other. The only constraint for this test is that the two models must be nested, otherwise Wilks's theorem cannot be applied. Two nested models are, for example, the power law and the power law with exponential cutoff, since the former can be obtained by the latter by considering a cutoff energy tending to infinity.

4.3.2 DL3 to DL4

The DL4 stage is just an intermediate step from the initial to the final product and the basic task is a data reduction of the DL3 files to obtain binned data in x, y, and

energy. First, the *DataStore* object of `gammapy` was created. This consists of a list of the selected γ-ray events along with their arrival time, reconstructed energy and coordinates. To properly bin the list in energy, the ON region, usually a circular region around the source coordinates, from where to extract the source signal had to be defined. For Geminga a radius of 0.1° for the circular region was chosen.

The `gammapy` class performing the binning of the *DataStore* objects is called *Makers* and, as previously reported, it the true and reconstructed energy axes have to be defined. For the present work, they were chosen as follows:

1. E_{true}: [0.003, 50] TeV, n_{bin}=100;
2. E_{reco}: [0.01, 10] TeV, n_{bin}=40.

The values of the boundaries for both E_{true} and E_{reco} are arbitrary since the analysis should be independent of the chosen binning. The only attention is that the E_{true} axis should be chosen slightly larger than E_{reco}.

Then, an empty *Dataset* object was created based on the geometry of the ON region and the true energy axis, and was subsequently filled by using the methods of the *Makers* class to produce the final DL4, which comprises both the binned information on the source and from the background. In particular, for the background region, the usual practice is to define the OFF regions where to measure the signal, but for pulsars one can choose to follow a phase-resolved approach. If one chooses the latter, the class *PhaseBackgroundMaker* should be used to estimate the background signal in the same observed ON region as the source, but in the OFF-phase region (i.e. the phase interval where there is no signal from the pulses). This approach was used for Geminga and the phase regions were defined as

$$\text{P1} = [0.056;\ 0.161] \quad \text{P2} = [0.550;\ 0.642] \quad \text{OFF} = [0.700;\ 0.950]$$

same as MAGIC and *Fermi*-LAT Collaborations. Depending on which peak was studied, the ON region could be either P1 or P2.

4.3.3 DL4 to DL5

Following the forward folding fitting method, the first thing was to define the spectral model. For `gammapy`, the user can choose between a spectral, a spatial, a temporal model, or all of the three combined, but for the analysis of Geminga, only spectral components have been included. To obtain the final science products, two approaches are available for the analysis:

a) **Joint analysis**

Each *Dataset* object obtained at the end of the previous stage is handled singularly even for the likelihood fit procedure. The software applies the fit on the individual

Dataset and computes the associated likelihood, and only at the end the single objects are piled up together to compute the total fit statistic and the flux points.

b) **Stacked analysis**

After obtaining the *Dataset* object for every observation, they are stacked into a single object, a *SpectrumDatasetOnOff* including the information on both the ON and the OFF regions for all the observations piled up together. Then, the fit is applied to the stacked object and the likelihood is derived. Stacking can be useful to reduce computational time, but it should be applied only when the events come from the same instrument and have the same geometry.

For both the fits performed for the present work, the LST-1 only analysis and the joint one with *Fermi*-LAT and MAGIC data, the joint analysis method has been adopted. In the first case, the amount of data to be analysed was not too extended to require the use of the stacked analysis. Instead, in the case of the joint fit, a stacked analysis could not be carried out since data were not coming from the same instrument and were of different natures (MAGIC and *Fermi*-LAT data were directly in the form of flux points and, to perform a stacked fit, the correlation matrix of the data would have been needed).

The first analysis was the one on LST-1 data only. The model chosen for the fit was a power law, `PowerLawSpectralModel` in `gammapy`, defined as:

$$f(E) = f_0 \left(\frac{E}{E_0} \right)^{-\Gamma} \tag{4.7}$$

Before applying the likelihood fit, the method `stat_sum()` of `gammapy` was used to estimate the likelihood of the null hypothesis $\mathcal{L}_0$, i.e. the likelihood assuming that the signal is only due to background fluctuations. The same method has been run after the fitting procedure to estimate the likelihood of the fitted model $\mathcal{L}$. In addition, to be able to produce the final SED, the flux points were estimated using the *Estimator* sub-package.

Lastly, to carry out the joint fit, a *Datasets* had to be created. *Datasets* in `gammapy` are collections of *Dataset* objects, which can be different and can even come from different instruments. The one for this analysis was built by adding *Fermi*-LAT flux points, MAGIC flux points, and the *SpectrumDatasetOnOff* of LST-1 points, previously created by stacking the *Dataset* of LST-1 observations. The two tested models were a power law with an exponential cutoff and with a sub-exponential cutoff, both described by the `gammapy` model `ExpCutoffPowerLawSpectralModel`:

$$f(E) = f_0 \left(\frac{E}{E_0} \right)^{-\Gamma} \exp \left[- \left(\frac{E}{E_c} \right)^{\beta} \right] \tag{4.8}$$

where the β parameter is free to vary in the case of the sub-exponential and frozen to $\beta = 1$ for the exponential cutoff.

Both spectral shapes have been fitted to the *Datasets* object to obtain the value of the likelihood $\mathcal{L}$ that is used to perform the likelihood ratio test between the two models.

4.3.4 Production of the phaseogram

A phaseogram is a histogram of the observed events binned in phase and is commonly used for pulsar analysis since it provides information on the emission regions and the viewing geometry. The package `PulsarTimingAnalysis` has been employed again to obtain all the phaseograms of the present work. The package can also compute the Li&Ma statistic of the peaks and the results of other statistical tests (see § 4.3.5) and add them to the final phaseogram. To produce the plot, a configuration file was used to provide the values of all the parameters needed for the setup:

- Phase binning: [0, 2], $n_{bin} = 60$;
- Energy binning: [15, 75] GeV, $n_{bin} = 6$. This setting allowed the production of the phaseogram for different energy ranges. The width of the energy bins, as one will notice in the next Chapter, is not uniform because they are represented on a logarithmic scale;
- Evolution in time computed every half an hour.

As in the case of the energy axes for the DL4 production, all the binnings are arbitrary and this setup has been chosen only to optimize the appearance of the final plot.

4.3.5 Additional statistical tests

To assess the quality of the results, some additional statistical tests have been included in the analysis of the phaseogram. In particular:

- χ^2 **test**, which is a classical test used to statistically verify if the observed data is compatible with the expectations, taking into account the errors:

$$\chi^2 = \sum_{k=1}^{n} \frac{(O_k - E_k)^2}{\sigma_k^2} \tag{4.9}$$

  where O_k are the observed data, E_k the expected values, and σ_k the errors associated to the observations. For this analysis, the expected values are obtained assuming the null hypothesis is true.

- Z_m^2**-test**, developed by Buccheri et al in 1983 [99] for the study of pulsars and based on the sum of the Fourier powers of m harmonics. Given the phase value ϕ_j

in the interval [0,1], with $j = 1, ..., N_i$ and N_i the number of photons used in the case of the i^{th} pulsar, the Z^2_m statistic is defined as:

$$Z^2_m = \frac{2}{\dot{N}_i} \sum_{k=1}^{m} \left(\sum_{j=1}^{N_i} \cos k\phi_j \right)^2 + \left(\sum_{j=1}^{N_i} \sin k\phi_j \right)^2 \tag{4.10}$$

where m is the number of harmonics used to compute it. Z^2_m has the same probability density function of a χ^2 with $2m$ degrees of freedom. Usually, the value $m = 2$ is the one chosen for optimal performances, but a default value of $m = 10$ is adopted in the package `PulsarTimingAnalysis`.

- **H-test**, developed by de Jager et al in 1989 [100] and revised in 2010 [101], which aims at the detection of a periodic signal inside a data sample, even if the light curve shape is not known or variable in time. The fundamental statistic is the same as the Z^2_m test, but the value of m is usually chosen optimally based on the analysed data. The H statistics is defined s:

$$H = \max_{1 \leq m \leq 20} (Z^2_m - 4m + 4) = Z^2_M - 4M + 4 \tag{4.11}$$

where M is a particular value of m that minimizes an estimator of the mean integrated square error. The probability distribution of the test statistics is an exponential function with a parameter $\lambda = 0.398$:

$$\mathcal{P}(> H) = \exp(-\lambda H) = \exp(-0.398H) \tag{4.12}$$

For each one of the tests, the associated significance of the periodic signal detection has been computed by finding the p-value associated with χ^2, Z^2_m or H.

4.4 To sum up

In this Chapter, the complete analysis procedure of LST-1 data has been explained step by step. First, the low-level analysis of the data from the DL1 to the DL3 pulsar level has been treated, along with all the specific cuts and the nodes adopted in the analysis of Geminga data. Then, the high-level analysis from the DL3 pulsar files to the final science products has been discussed. All the steps have been applied to the Geminga dataset used for this thesis work in order to obtain the phaseogram and the spectrum of the second peak of the light curve. From the first, the significance of the signal and the FWHM of the peak profile of P2 have been derived. The spectrum, instead, was useful to study the emission mechanism generating the detected γ rays. All the results of the analysis are presented in the next Chapter, along with the final discussion.

Chapter 5

Results

In this Chapter, the final results of this thesis are discussed: first, the ones related to the analysis of the data until the 14th of February 2023, then the complete analysis and the following interpretation of the results will be treated.

5.1 Analysis of the data sample taken before the 14th of February 2023

Initially, the analysis started with a reduced data sample excluding those observations affected by the timing issue. The problem was solved just in a second moment: as explained before, it took a few weeks to identify and provide a solution to the problem. The ending date of the data sample was chosen to be the 14th of February, which is the last night before March when the problem of the humidity patch (see § 4.1.2.1) was not observed. For this dataset, consisting of 16.4 hours of observations, both the phaseogram of Geminga and the spectrum of P2 were derived.

5.1.1 Phaseogram

The phaseogram of Geminga, along with the results of the associated statistical tests (§ 4.3.5) and the trend of the excess counts and the significance with time, were obtained with the use of the software `PulsarTimingAnalysis`. In Figure 5.1 the phaseogram is shown, with the phase regions of P1, P2 and the OFF phase (a priori defined as reported in § 4.3.2) highlighted in different colours. The values of the significance of both peaks and the result of the statistical tests are also reported. The second peak, P2, was detected with a significance of 7.6σ, while the significance of P1 was below the 5σ threshold for detection, reaching only a value of 2.6σ, which makes it compatible with statistical fluctuations. These results, even though not obtained from the analysis of the complete sample, are already better in terms of significance than the ones obtained by

the MAGIC Collaboration that found 6.3σ for P2 and only 0.3σ for P1 with 80 hours of good-quality observations [84].

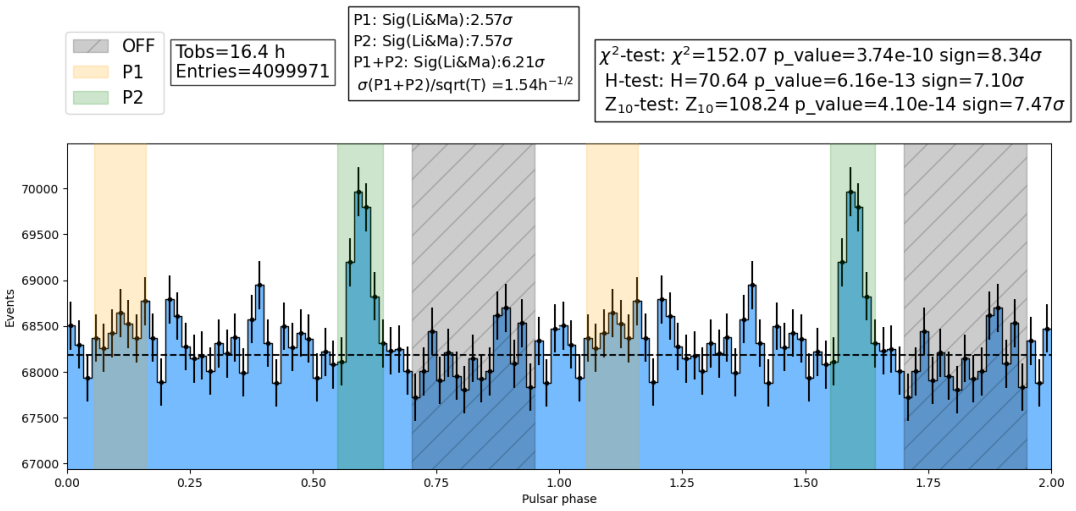

Figure 5.1: Geminga phaseogram of the data until the 14th of February 2023, along with the results of the statistical analysis (Li&Ma statistics and χ^2, Z_{10} and H tests statistics, see § 4.3.5). The ON phase regions of P1, P2 and the OFF phase region are highlighted in different colours and the horizontal line defines the averaged level of background counts extracted from the OFF phase region.

Figure 5.2 shows the trend of the excess counts with time for both of the peaks individually and together. The excesses, as mentioned in § 4.1.2.2, are computed as the difference between the observed and the background counts obtained from the OFF phase region. They are expected to follow a linear trend with time and this is verified for both P1 and P2 and also for P1+P2.

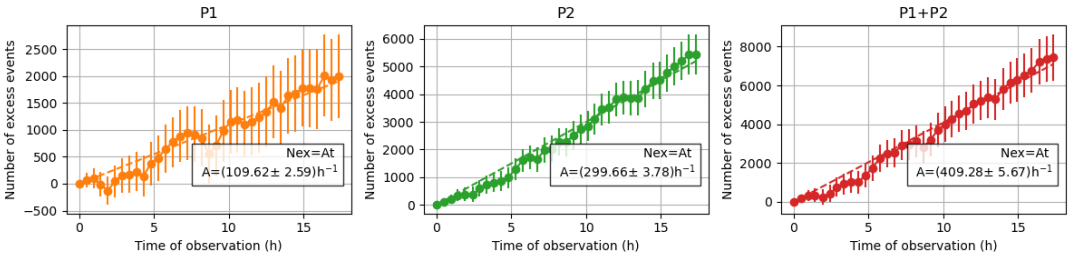

Figure 5.2: Trend of the excess counts of P1, P2 and P1+P2 as a function of time, for the data until 14th of February 2023. The best-fit results of the linear modelling are also reported.

Figure 5.3, instead, displays the trend of the significance σ of the signal, computed as the Li&Ma significance of the excess counts of the peak with respect to the level of

background, as a function of time. σ is expected to follow a $\sigma \propto \sqrt{t}$ trend with time and this is verified, on average, for both P1 and P2 and also for P1+P2. The signal of P1 does not reach the 5σ level and this is why the fluctuations are more evident in the trend.

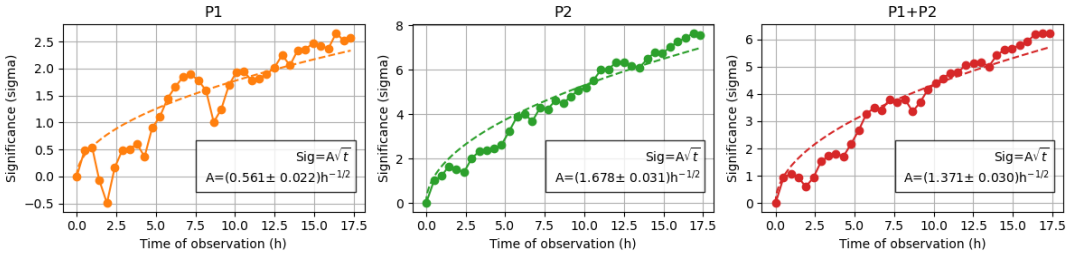

Figure 5.3: Trend of the significance of P1, P2 and P1+P2 as a function of time, for the data until 14th of February 2023. The best-fit results of the curves are also reported.

5.1.2 Spectrum of P2

After obtaining the phaseogram, the spectrum of P2 in the energy range [15, 75] GeV was derived. The upper boundary was chosen to be 75 GeV in order to extend the analysis to higher energies and compute an upper limit on the differential flux in the last energy bin. Indeed, as it is shown in the phaseograms per energy bin reported in § 5.2.1, the signal of P2 is detected up to ∼55 GeV: there is no detection in the last energy bin and only an upper limit on the differential flux can be obtained. On the other hand, the lower edge of 15 GeV was chosen after computing the energy threshold of the analysis. By studying the simulated MC data with a zenith angle of 10°, which is the lowest value between the ones of the nodes employed in the analysis, it was possible to derive an energy threshold of ∼10 GeV. The value increased for the other nodes at higher zenith. In order to be sure to be above the threshold, the lowest boundary of 15 GeV for the spectrum was chosen. The spectrum of P1 could not be derived because the significance of its signal was below the 5σ threshold.

The employed spectral model for the fitting was a power law spectral model (see eq. 4.7). The seed values for the fitting routine were taken from the MAGIC Collaboration (Table 5.1, first row). The free parameters of the model were the amplitude f_0 and the index Γ, while E_0, dubbed pivot or reference energy, was frozen to the same value as MAGIC. The results of the likelihood fit of LST-1 data are reported in Table 5.1. As one can see, the error on the amplitude f_0 is larger than the value itself. This is probably due to the low number of observation hours and it will be solved with the analysis of the complete dataset. For this reason, the error bar associated with the fit could not be properly plotted.

Table 5.1: Best-fit values of the power law spectral model for both MAGIC (reference model taken from [84]) and LST-1, with the associated statistical errors.

Model	f_0 **(cm^{-2} s^{-1} TeV^{-1})**	Γ	E_0 **(GeV)**
MAGIC	$(2.28 \pm 0.74) \cdot 10^{-9}$	5.62 ± 0.54	32.15
LST-1	$(1.9 \pm 2.0) \cdot 10^{-9}$	5.8 ± 1.3	32.15

5.2 Complete analysis of the data sample

After the time mismatch correction was accomplished, it was possible to obtain the analysis results of the complete sample, consisting of 21 hours of observations. As in the previous case, the final products of the analysis are the phaseogram and the spectrum of P2, but a Gaussian fit of P2 was also performed.

5.2.1 Phaseogram

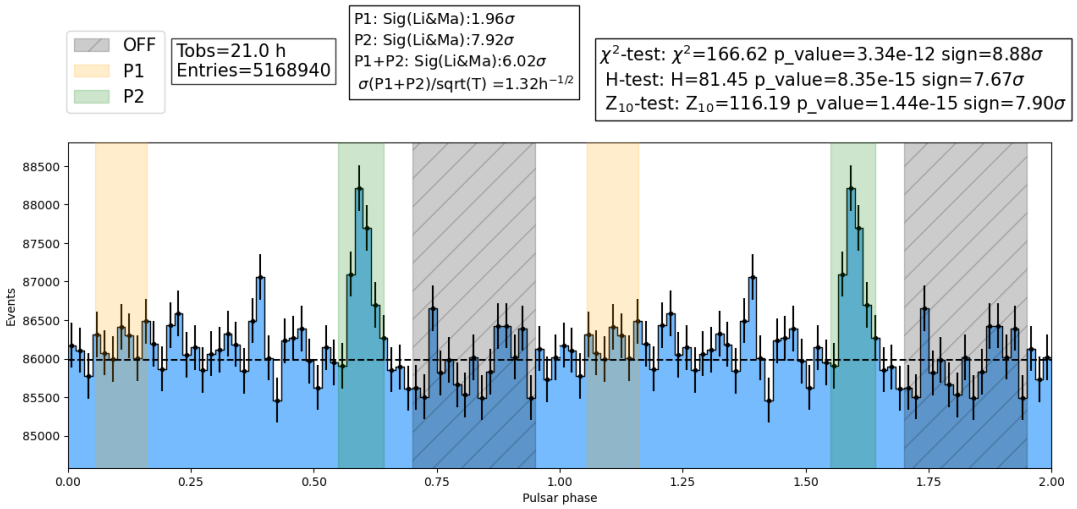

Figure 5.4: Final Geminga phaseogram, along with the results of the statistical analysis (Li&Ma statistics and χ^2, Z_{10} and H tests statistics, see § 4.3.5). The ON phase regions of P1, P2 and the OFF phase region are highlighted in different colours and the horizontal line defines the averaged level of background counts extracted from the OFF phase region.

Figure 5.4 depicts the final phaseogram of Geminga, obtained when analysing the complete data sample with `PulsarTimingAnalysis`. The significance of P2, thanks to the correction for the time mismatch and the higher observational time, increased to 7.9σ, which is close to the $\sim 7.7\sigma$ value predicted by the best-fit curve of the time evolution

of the significance in Figure 5.3. On the other hand, P1 still cannot be considered as detected since its signal reaches a significance of 2σ, compatible with statistical fluctuations. The phaseogram was also obtained for each of the six defined energy bins (see § 4.3.4). As one can see from Figure 5.5, there is still a robust detection of P2 until ∼55 GeV, while the signal drops in the last energy bin and becomes undetected.

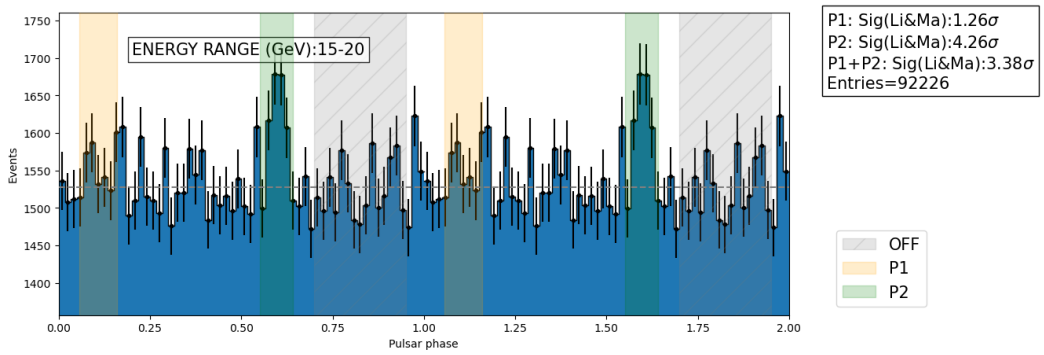

(a)

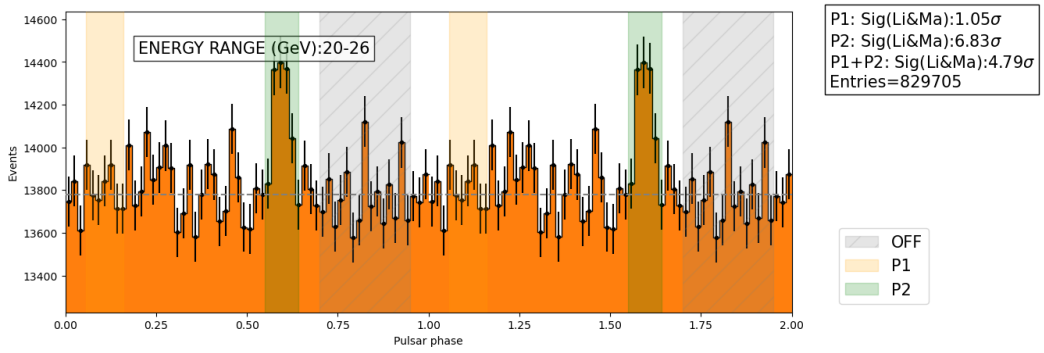

(b)

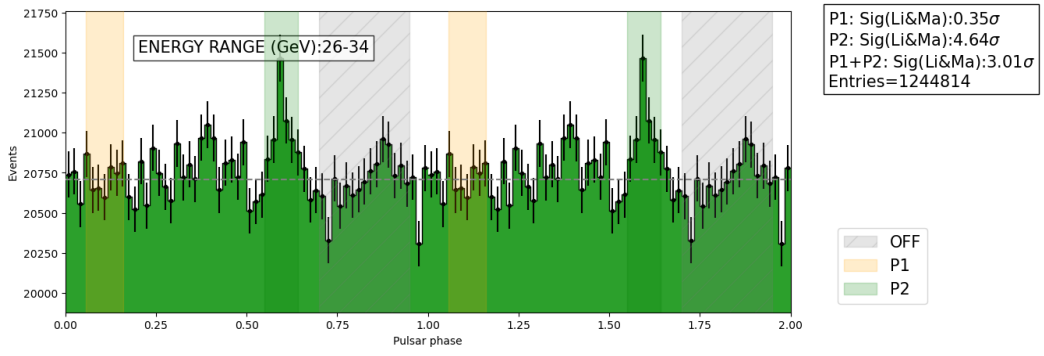

(c)

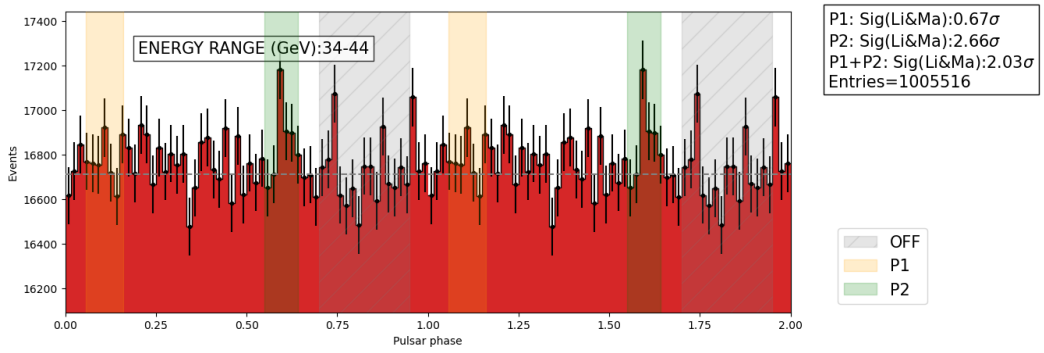

(d)

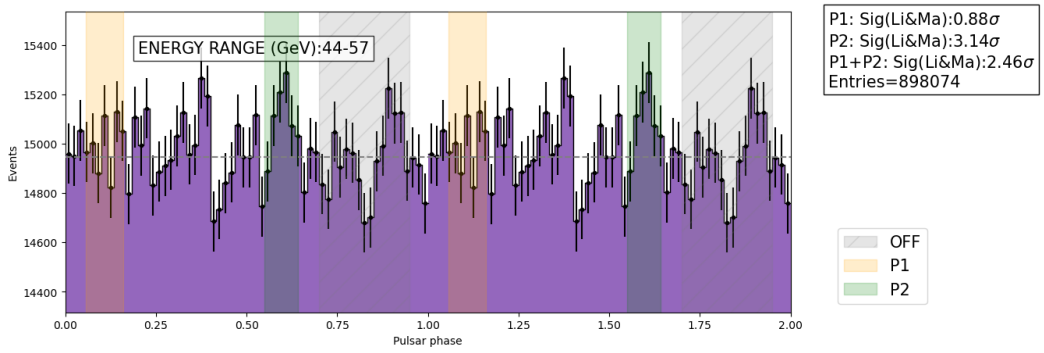

(e)

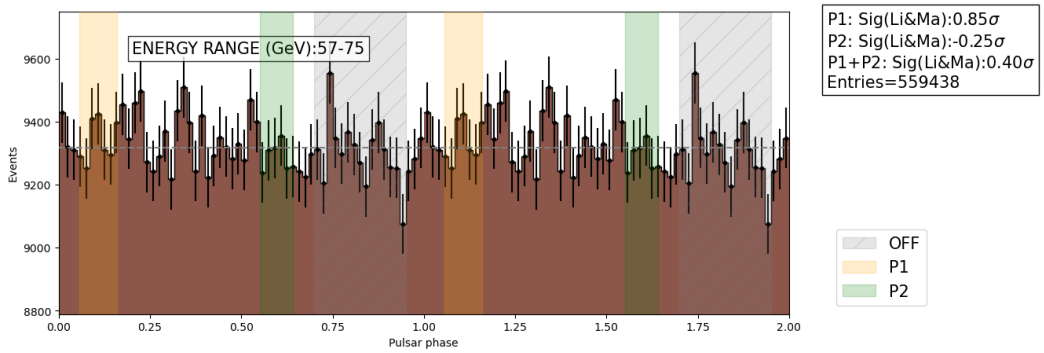

(f)

Figure 5.5: phaseograms for each of the chosen energy bins. In these plots, only the significance of the peaks is reported.

In Figure 5.6 the behaviour of the excess counts for P1, P2 and P1+P2 as a function of time is reported. From these plots, it is clear that the correction for the time issue was successful since the trend of P1, even though is still not properly linear, is compatible with the fit within the error bars. The non-linear behaviour of the last observational hours could be related to the increase of the mean zenith angle in March, other than to statistical fluctuations. Indeed, if one plots the time evolution of the excess counts for

the zenith range [0°, 15°], it is possible to see a proper linear trend also for P1 (see § 5.2.1.2 for more details).

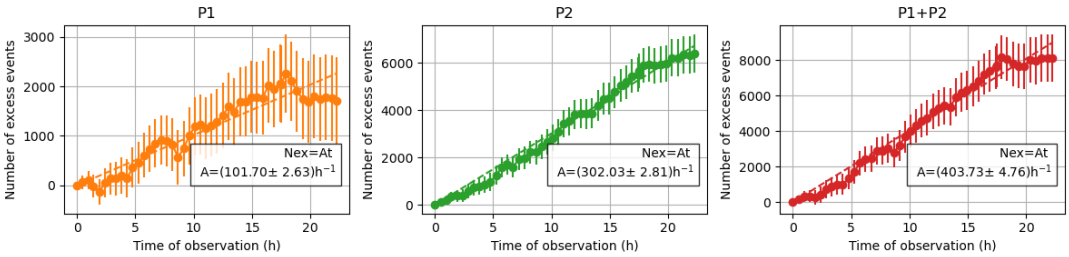

Figure 5.6: Trend of the excess counts of P1, P2 and P1+P2 as a function of time for the complete data sample. The best-fit results of the curves are also reported.

Figure 5.7 shows the time evolution of the significance of both peaks individually and together, along with the respective fit functions. As for the excess counts, the trend of P1 does not properly follow the expected $\sigma \propto \sqrt{t}$ behaviour, but the signal is compatible with statistical fluctuations so, on average, the expectations are satisfied.

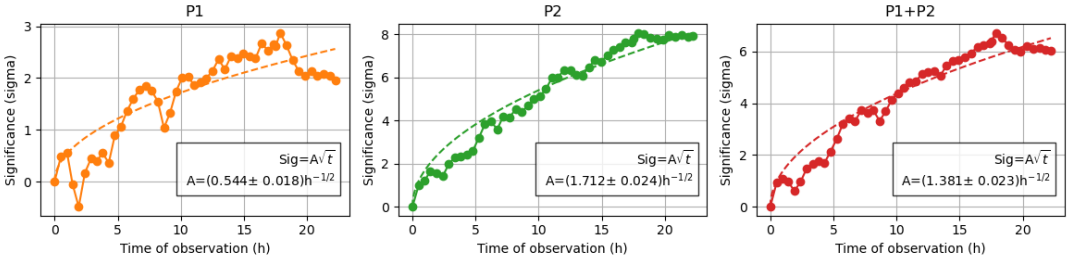

Figure 5.7: Trend of the significance of P1, P2 and P1+P2 as a function of time for the complete data sample. The best-fit results of the curves are also reported.

5.2.1.1 Gaussian fit of P2

Thanks to the higher statistical significance of the P2 signal with respect to MAGIC Collaboration, a study on the pulse shape could be performed for the first time at Very High Energies. The easiest curve describing the peak of the phaseogram is a symmetric Gaussian plus a constant that fits the background level; the study for this thesis started with such model. The available photon statistics, however, did not allow the use of more complicated functions. The fit has been performed in one energy bin from 15 GeV to 57 GeV, which corresponds to the whole energy range where P2 shows a signal not compatible with statistical fluctuations. The mean μ, the standard deviation σ, and the background level, which were considered free parameters of the fit, have been derived.

The final goal was to obtain the Full Width at Half Maximum (FWHM), defined as

$$FWHM = 2\sqrt{2\ln 2}\sigma \tag{5.1}$$

and cross-check its value with the results obtained at lower energies in order to have an idea of the location of the acceleration site of the particles. The fit results are reported in Table 5.2 and the best-fit curve is shown in Figure 5.8. The error on the FWHM has been derived by applying the error propagation rules on eq. 5.1.

Table 5.2: Results of the Gaussian fit on P2 in the energy range [15, 57] GeV, where the signal is above the detection threshold.

Mean	σ	FWHM	Background counts
0.597 ± 0.003	0.018 ± 0.003	0.042 ± 0.006	$(67.42 \pm 0.04) \cdot 10^3$

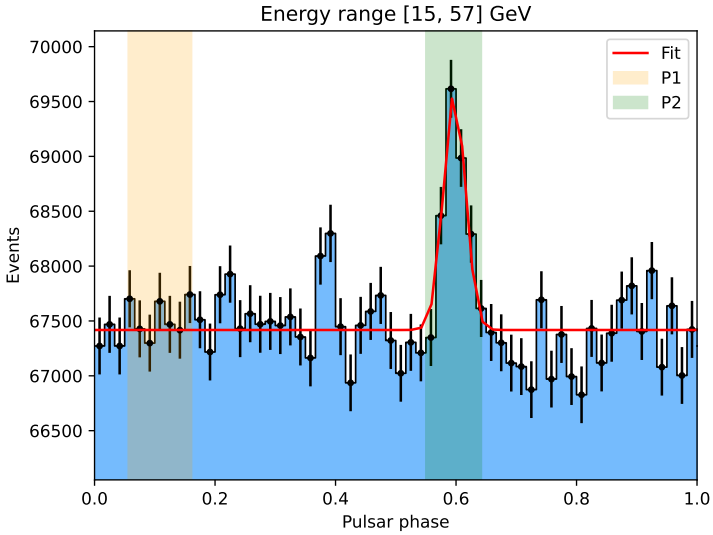

Figure 5.8: Gaussian fit of P2 in the energy range [15, 57] GeV, where the signal is detected. The phase regions of P1 and P2 are highlighted in different colours.

The modelling of the FWHM at these energies was never achieved before and previous *Fermi*-LAT results on the FWHM at MeV energies taken from [83] have been considered to study the global evolution of the FWHM with the energy; the results are shown in Figure 5.9. *Fermi*-LAT Collaboration already found a slightly decreasing trend with the energy, and the point added with the analysis of LST-1 observations is compatible with this trend, highlighting the fact that the peak gets narrower with increasing energy.

From the shift in the best-fit peak position of the *Fermi*-LAT and LST-1 data, it was possible to derive the time delay between the MeV-GeV and GeV-TeV emission by using the relation between the phase shift $\Delta\Phi$ and the time delay Δt:

$$\Delta\Phi(\text{deg}) = 360^\circ \cdot \frac{1}{P} \cdot \Delta t \tag{5.2}$$

Considering the best-fit value of the peak position of *Fermi*-LAT data $\mu = 0.638 \pm 0.003$, one finds $\Delta t = 27\mu$s. This value suggests a similar acceleration site for the two energy ranges, where absorption of TeV photons is unavoidable, but without the analysis of the systematics it is not possible to draw conclusions.

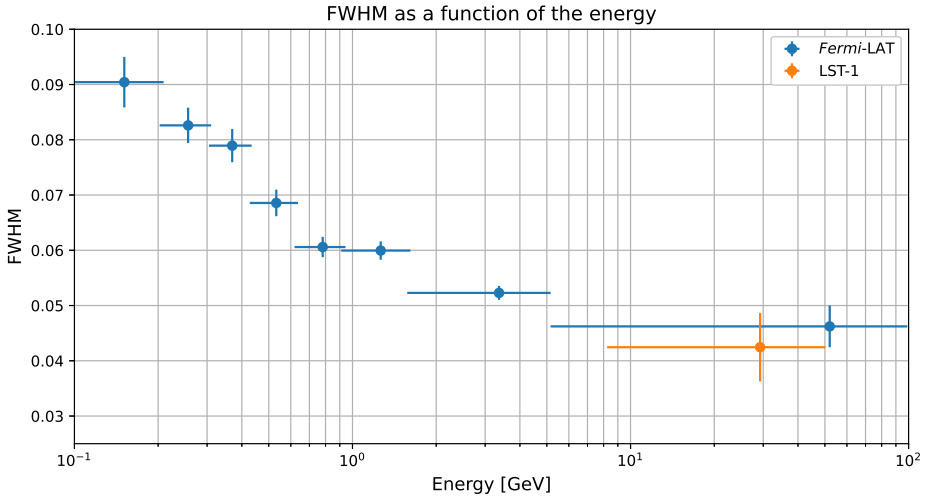

Figure 5.9: Evolution of the FWHM of P2 as a function of the energy, including *Fermi*-LAT points from [83].

5.2.1.2 Observational time for the detection of P1

The results of the analysis show that the first peak of the Geminga light curve, P1, was not detected by LST-1 since its significance is below the 5σ threshold. However, from the best-fit curve computed with the software, it is possible to derive an estimate of the number of hours needed to reach a 5σ detection. This exercise was done by considering only the fitting results of the 0°-15° zenith range that guarantees a lower energy threshold. It has been already observed that the time evolution of P1 significance does not exactly follow the expected behaviour due to the higher mean zenith angle of the latest observations, but if one focuses on the range [0°, 15°] the excesses, on average, increase linearly with time (Figure 5.10). The significance is expected to follow a trend proportional to $\sqrt{t}$ and, considering the fact that the signal is basically background noise,

the curve can be considered compatible with the expectations. In particular, the best-fit curve for σ can be reversed to estimate the number of hours to detect P1:

$$t_{P1} = \left(\frac{\sigma}{A}\right)^2 = \left(\frac{5}{A}\right)^2 \simeq 69\text{h} \tag{5.3}$$

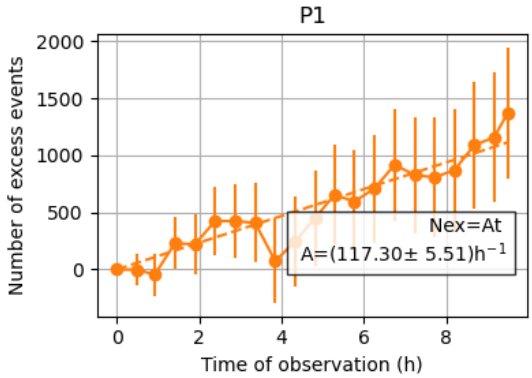

Figure 5.10: Excess counts for P1 in the zenith range [0°, 15°].

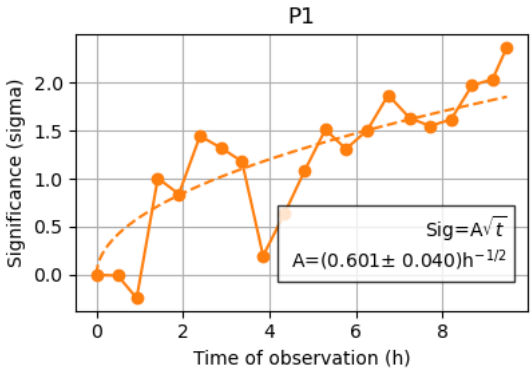

Figure 5.11: Significance of P1 for the zenith range [0°, 15°].

The same computation can be repeated using the best-fit result for the time evolution of the P1 significance extending the zenith range up to 25° (Figure 5.7) and the estimate would be $t_{P1} \simeq 84.5$h. This result is important because it shows that, with future observations and in a reasonable amount of hours, it could be possible to detect the first peak of the light curve for the first time at VHEs. The detection of P1 at these energies would allow the production of the spectrum for both peaks as well as the study of the pulse profiles and, in turn, to have a more complete picture of the emission of Geminga at VHEs.

5.2.2 Spectrum of P2

As for the previous case, despite the fact that no signal is detected above 55 GeV, the energy range for the spectral analysis was extended up to 75 GeV to be able to compute at least one upper limit on the differential flux above 55 GeV. The spectral model that has been tested is a power law with the MAGIC Collaboration best-fit results as reference values for the free parameters and with E_0 fixed to 32.15 GeV. The results are summarised in Table 5.3; it is clear that they are compatible, within the associated errors, with what MAGIC Collaboration obtained. The spectrum and its associated residuals are shown in Figure 5.12. The large errors associated with the parameters obtained with the LST-1 analysis could be related to the narrow energy range considered, which does not allow a

fit with high precision. The energies analysed are close to the threshold of the telescope and the energy resolution is not very accurate.

Table 5.3: Final best-fit values of the power law spectral model for both MAGIC (reference model) and LST-1, with the associated statistical errors.

Model	f_0 **(cm^{-2} s^{-1} TeV^{-1})**	Γ	E_0 **(GeV)**
MAGIC	$(2.28 \pm 0.74) \cdot 10^{-9}$	5.62 ± 0.54	32.15
LST-1	$(2.2 \pm 1.7) \cdot 10^{-9}$	5.5 ± 1.1	32.15

Due to a problem with its definition in `gammapy`, the error bar on the fitting function was defined by hand by considering the errors on f_0 and Γ. In particular, four combinations of the function have been defined:

$$\frac{dN}{dE} = (f_0 \pm \sigma_{f_0}) \left(\frac{E}{E_0} \right)^{-(\Gamma \pm \sigma_\Gamma)} \tag{5.4}$$

where σ_{f_0} and σ_Γ are the 1σ errors obtained with `gammapy`. Then, the fitting results were used to compute the flux points, which have been represented in a plot along with their TS profiles (Figure 5.13). The plot shows that the signal is significant up to $\sim$55 GeV, in agreement with what has been found when studying the phaseogram per energy bin. In the last energy bin, where the signal is not detected, an upper limit has been derived assuming the same spectral slope as the model. This is not constraining since the upper limit is still compatible with the extrapolation of the model up to 75 GeV, so it is not possible to understand if the power law is extended to higher energies or if a cutoff is present.

It is worth mentioning that the non-uniformity of the energy bins' length is related to how `gammapy` defines the energy binning: the software takes into account the excess events in each of the bins and the width will be inversely proportional to the value. So, if the excess counts in a certain energy range are low, the bin must be wider.

The obtained fitting parameters are correlated among them and the level of correlation is shown in Figure 5.14. In this thesis work the effect of the systematics was not treated and it is one of the main future improvements for the study of Geminga.

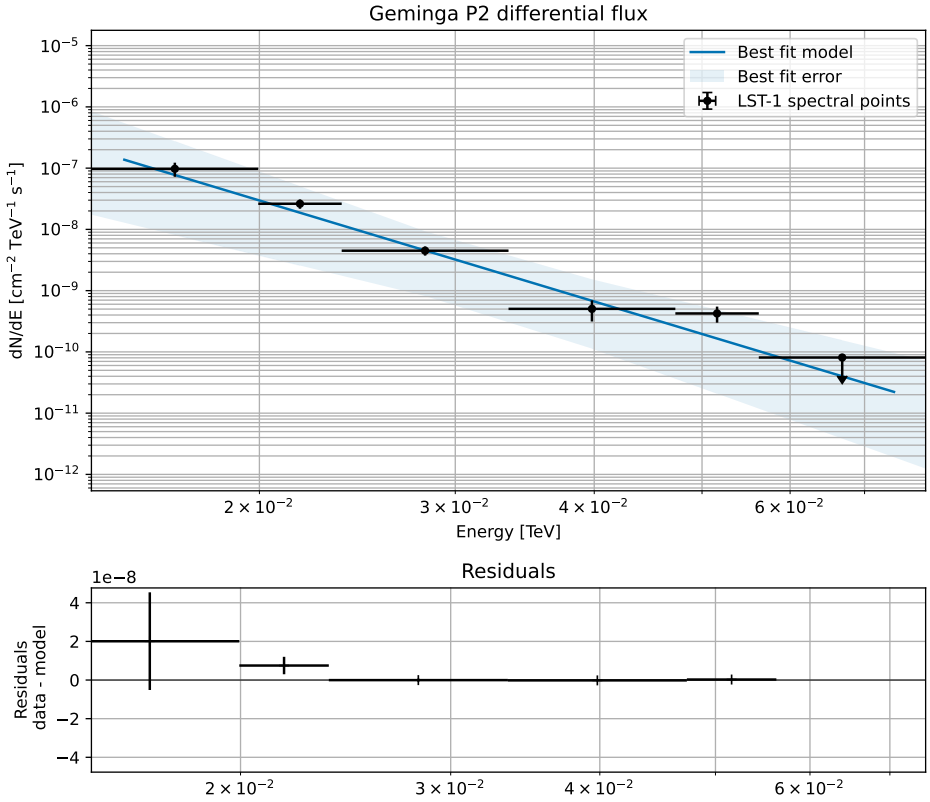

Figure 5.12: Differential flux of the second peak of Geminga, along with the best-fit curve and its error (upper panel), and its residuals (bottom panel).

Table 5.4: Flux points in dN/dE format, along with the associated statistical errors and the energy bins' lower (E_{low}) and upper (E_{up}) limits. The upper limit on the last energy bin is not reported in the table.

E_{ref} **(GeV)**	E_{low} **(GeV)**	E_{up} **(GeV)**	**dN/dE (TeV^{-1} · cm^{-2} · s^{-1})**
16.8	14.1	20.0	$(10 \pm 3) \cdot 10^{-8}$
21.8	20.0	23.7	$(2.6 \pm 0.5) \cdot 10^{-8}$
28.2	23.7	33.5	$(4.5 \pm 0.8) \cdot 10^{-9}$
39.8	33.5	47.3	$(5 \pm 2) \cdot 10^{-10}$
51.6	47.3	56.2	$(4.2 \pm 1.2) \cdot 10^{-10}$

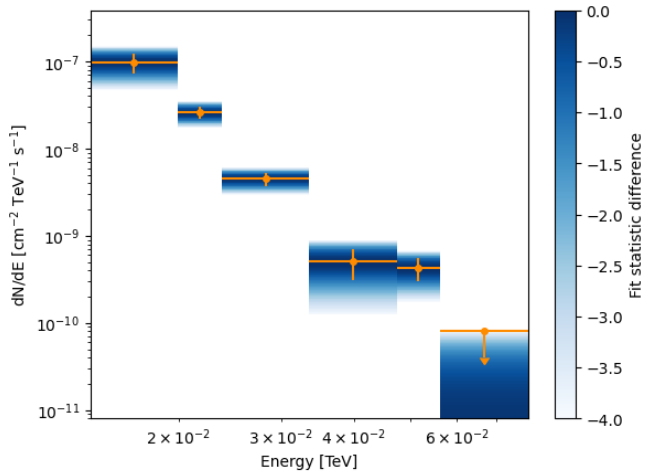

Figure 5.13: Flux points for the power law spectral model (orange points) with the respective Test Significance profile (blue area).

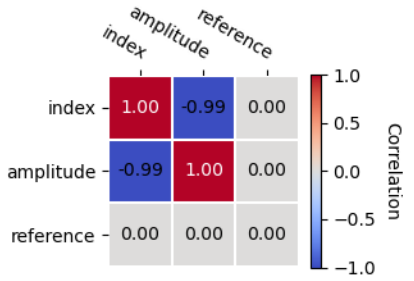

Figure 5.14: Correlation matrix of the power law parameters f_0, Γ, and E_0.

5.2.2.1 Different reference energies

From Table 5.3 it is clear that the error associated with LST-1 points is around a factor two higher than the one obtained by MAGIC, for both the amplitude f_0 and the index Γ. To further investigate this problem, as well as the high correlation between the two parameters, lower reference energies E_0 have been used in the fit.

Table 5.5: Best-fit results for different reference energies E_0. In the table, there is also the relative error on the amplitude f_0, the value of the likelihood ratio test, and the value of the correlation between Γ and f_0.

E_0 **(GeV)**	f_0 **(cm^{-2} s^{-1} TeV^{-1})**	$\Delta f_0/f_0$	Γ	**Correlation**
25.00	$(9 \pm 4) \cdot 10^{-9}$	44%	5.5 ± 1.0	-98%
20.00	$(3.0 \pm 0.8) \cdot 10^{-8}$	27%	5.5 ± 0.9	-92%
18.00	$(5.3 \pm 1.0) \cdot 10^{-8}$	19%	5.5 ± 0.9	-81%
15.00	$(1.4 \pm 0.1) \cdot 10^{-7}$	7%	5.5 ± 0.9	15%

The value of the decorrelation energy[1] was found to be 15.3 GeV: this is extremely close to the lower boundary of the energy range where the fit is applied and it is still not clear why. However, as expected, the reduction of the reference energy to values progressively close to the decorrelation energy lowers the correlation between the parameters and the relative error on the amplitude, even though the error on the index

[1]The energy at which the correlation between the parameters is zero.

is not affected. Both these issues, the low decorrelation energy and the error on the spectral index, will be investigated more in-depth in the future, also collaborating with the software developers.

5.3 Joint fit of P2 with MAGIC and *Fermi*-LAT data

In order to have a clearer picture of the mechanism at the basis of the γ-ray VHE emission, it is important to include *Fermi*-LAT data in the analysis to extend the γ-ray range to a lower edge at MeV energies. In particular, it is crucial to understand if the radiation in the VHE comes from the same region and if the emission mechanisms are the same as the one detected by *Fermi*. To reach this goal, a joint fit of *Fermi*-LAT and LST-1 points is performed. In addition to the above-mentioned datasets, MAGIC spectral points are considered in the fit and they are not expected to change the final results. The *Fermi*-LAT spectral points were provided by Dr. Marcos López-Moya and they were the result of the analysis of more than ten years of observations, starting from the 4th August 2008 and ending on the 16th January 2023; the MAGIC spectral points, instead, are the ones reported in [84]. Given the wider energy range of the joint analysis (from 100 MeV to 100 GeV) with respect to the fit of the VHE points only, two spectral models were tested, the power law with an exponential (dubbed PLEC) and with a sub-exponential cutoff (dubbed PLSEC), both described by the `gammapy` function `ExpCutoffPowerLawSpectralModel`, which is defined as:

$$f(E) = f_0 \left(\frac{E}{E_0} \right)^{-\Gamma} \exp[-(\lambda E)^{\beta}] \tag{5.5}$$

This form is slightly different than the usual definition of the power law with an exponential cutoff (eq. 4.8): the parameter $\lambda = 1/E_c$ is used instead of the cutoff energy E_c. For the power law with the exponential cutoff, the parameter β was frozen to 1 while, in the other case, it was free to vary. The seed values for the fitting were taken from the best-fit results of the joint fit performed in [84] (Table 5.6). The best-fit results of the joint fit with LST-1, MAGIC and *Fermi*-LAT, along with their statistical errors and the value of the likelihood after the fit, are reported in Table 5.7, and the plot is shown in Figure 5.15.

Table 5.6: Best-fit values of the joint likelihood fit of MAGIC and *Fermi*-LAT data for both the power law with the exponential (PLEC) and the sub-exponential (PLSEC) cutoff models. These values were taken from [84] and have been used as a reference for the fitting procedure.

Model	f_0 **(cm^{-2} s^{-1} TeV^{-1})**	E_0 **(GeV)**	Γ	E_c **(GeV)**	β	**-2**log($\mathcal{L}$)
PLEC	$(0.357 \pm 0.002) \cdot 10^{-3}$	1.00	1.089 ± 0.003	2.88 ± 0.02	1	388.2
PLSEC	$(0.552 \pm 0.019) \cdot 10^{-3}$	1.00	0.910 ± 0.013	1.44 ± 0.08	0.738 ± 0.013	51.6

Table 5.7: Best-fit values (with their statistical errors) of the joint likelihood fit of LST-1, MAGIC and *Fermi*-LAT data for both the power law with the exponential (PLEC) and the sub-exponential (PLSEC) cutoff models. `gammapy` uses λ as the spectral parameter, instead of the cutoff energy E_c and this is why both of them are reported in this table.

Model	f_0 **(cm^{-2} s^{-1} TeV^{-1})**	E_0 **(GeV)**	Γ	λ (GeV^{-1})	E_c **(GeV)**	β	**-2**log($\mathcal{L}$)
PLEC	$(3.50 \pm 0.01) \cdot 10^{-4}$	1.00	1.102 ± 0.003	0.341 ± 0.002	2.933 ± 0.002	1	506.8
PLSEC	$(5.09 \pm 0.03) \cdot 10^{-4}$	1.00	0.94 ± 0.01	0.62 ± 0.03	1.60 ± 0.03	0.76 ± 0.01	119.6

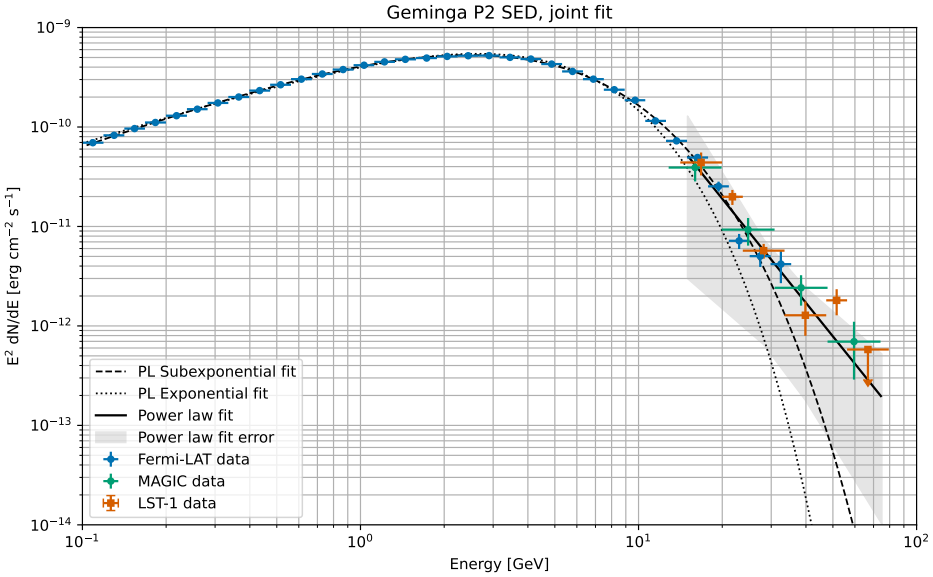

Figure 5.15: P2 SED from 100 MeV to 100 GeV including *Fermi*-LAT (blue), MAGIC (green) and LST-1 (orange) points. The points from LST-1 are fitted from 15 to 75 GeV with the power law spectral model (solid line) with its error bar (grey area). The dashed and dot-dashed lines represent the power law with exponential and sub-exponential spectral models.

The correlation matrix between the parameters of the two models has been derived

and is shown in Figure 5.16 for the power law with exponential cutoff and in Figure 5.17 for the power law with sub-exponential cutoff, respectively.

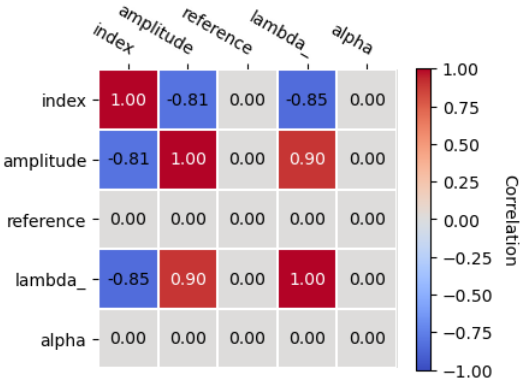

Figure 5.16: Correlation matrix of the parameters of the power law with the exponential cutoff model.

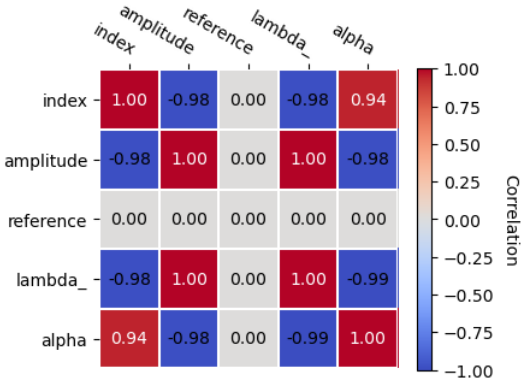

Figure 5.17: Correlation matrix of the parameters of the power law with the sub-exponential cutoff model.

A different parametrization for the power law with the sub-exponential cutoff has also been tested. The model function has been developed for *Fermi*-LAT analysis to improve the fit results of the usual models adopted for pulsar analysis and reduce the correlation between the parameters [102]. The function is defined as follows:

$$\begin{aligned} \frac{dN}{dE} &= K\left(\frac{E}{E_0}\right)^{\frac{a}{\gamma_2}-\Gamma_1} \exp\left[\frac{a}{\gamma_2^2}\left(1-\left(\frac{E}{E_0}\right)^{\gamma_2}\right)\right] \\ &= K\left(\frac{E}{E_0}\right)^{-\Gamma_1-\frac{a}{2}\ln\frac{E}{E_0}-\frac{a\gamma_2}{6}\ln^2\frac{E}{E_0}-\frac{a\gamma_2^2}{24}\ln^3\frac{E}{E_0}} \qquad \textbf{for} \quad \left|\gamma_2 \ln\frac{E}{E_0}\right| < 10^{-2} \end{aligned} \tag{5.6}$$

In `gammapy` it is known as `SuperExpCutoffPowerLaw4FGLDR3SpectralModel`.

The results are similar to the expected parameters and the function perfectly overlaps with the other parametrization of the power law with sub-exponential cutoff. The value of the likelihood test was also the same as for the other model. The main advantage of this more complex parametrization is that the correlation between the parameters is significantly reduced, as one can see from Figure 5.18.

Table 5.8: Reference values, which were provided without the associated statistical errors, and best-fit results for the joint fit using the Fermi parametrization of the power law with sub-exponential cutoff.

Model	K ($\mathbf{cm^{-2}\ s^{-1}\ MeV{-}1}$)	Γ_1	E_0 (MeV)	γ_2	a
Ref	$0.573 \cdot 10^{-10}$	2.24	1670	0.775	0.808
Results	$(1.12 \pm 0.03) \cdot 10^{-11}$	1.728 ± 0.003	1670	0.76 ± 0.01	0.599 ± 0.003

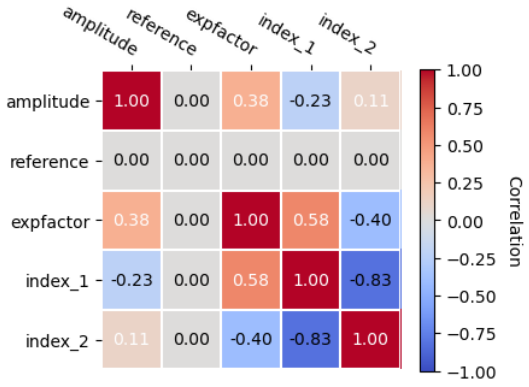

Figure 5.18: Correlation matrix for the power law with the sub-exponential cutoff using the *Fermi*-LAT parametrization.

The likelihood ratio test has been employed to compare the two models (PLEC and PLSEC) to see if one could be discarded in favour of the other. The test could be performed because the models are nested. In particular, the ratio was found to be ΔTS = 387.2 and it was possible to rule out the power law with exponential cutoff with a confidence level of 19.7σ. For what concerns the power law with a sub-exponential cutoff, it was not possible to exclude it using the tools available in `gammapy`.

To test if new emission mechanisms are in place other than the curvature radiation responsible for the *Fermi*-LAT emission and explained with the Outer Gap models, different models need to be fitted to the data. A possibility can be the PLSEC plus a power law, which would highlight the presence of an Inverse Compton tail after a certain value of energy. This kind of spectrum has not been tested for the present work, but it will be studied in the future.

5.3.1 Outer Gap modelling

The Outer Gap models are the most commonly adopted ones when trying to theoretically model the γ-ray emission from pulsars and they are based on the assumption that curvature radiation is responsible for the observed γ rays.

For the LST-1 observations of Geminga, the results of the analysis have been compared with a theoretical model produced by Hirotani [84], which consists of a modified version of the Outer Gap model (see § 3.2.1). This variation takes into account the viewing angle ζ of the pulsar from the Earth, the magnetic moment μ and the angle α between the rotation axis and the magnetic field. The three values can be changed to obtain a curve which is most compatible with the data. For the present work, the model using $\mu = 1.4\mu_d$ (where μ_d is the value of the magnetic moment assuming dipole radiation), $\alpha = 30°$, and $\zeta = 95°$ was found to be the most compatible one (Figure 5.19).

Concerning the energy range taken into account for LST-1 observations, i.e. [15, 75] GeV, the OG theoretical predictions lie inside the error bar of the power law. However, the model fails at reproducing the *Fermi*-LAT curve in the whole interval from 100 MeV to tens of GeV, highlighting the limitations of the Outer Gap model in explaining the VHE emission of Geminga.

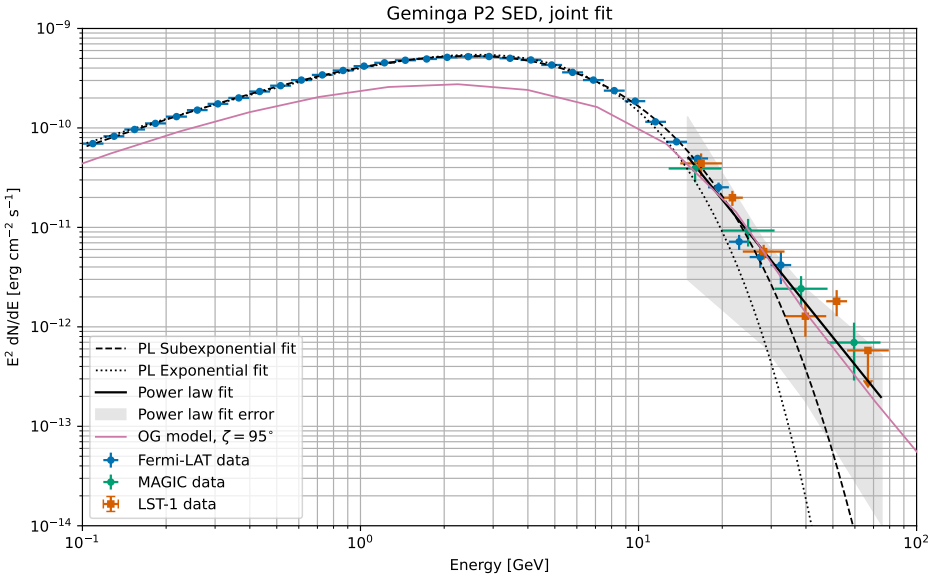

Figure 5.19: P2 SED from 100 MeV to 100 GeV including *Fermi*-LAT, MAGIC and LST-1 points (fitted with the power law from 15 to 75 GeV). The dashed and dot-dashed black lines represent the power law with exponential and sub-exponential spectral models, while the purple solid line is the theoretical prediction from the Outer Gap modelling assuming a viewing angle of $\zeta = 95°$.

5.4 Discussion of the results

This analysis resulted in the detection of the second peak of the Geminga phaseogram with a significance of about 8σ with 21 hours of good-quality observations. Both MAGIC and LST-1 observed Geminga at a zenith angle lower than 25° and using the so-called analogic sum trigger, which is able to lower the energy threshold of the analysis: the analogic signals are summed before being digitized and sent to the trigger system, so that even the smallest signals, thus the ones at the lowest energies, can survive the selection. Despite these similarities, the outcome of the analysis of LST-1 data is striking considering that the MAGIC Collaboration reached a significance of 6.3σ with a sample of 80 hours of observations obtained with an array of two telescopes. LST-1 is a single telescope and, with one-fourth of the MAGIC observational hours, the final significance of P2 was significantly higher. On the other hand, P1 was not detected either by MAGIC or LST-1, but under the assumption that P1 emits up to a few tens of GeV, the LST-1 will be able to detect it for the first time at VHEs with at least 60 hours of observations at a zenith distance smaller than 15°. Given the very stringent zenith range, this is achievable in one single observation period if the weather conditions are really favourable. If it is still not detected in 60 hours, then it can be possible to constrain the cutoff energy anyway.

The results of this thesis proved that the LST-1 has excellent capabilities in studying the very low boundary of the VHE band of γ rays with an energy threshold of the standard trigger which is as good as the analogic sum trigger of the MAGIC. This is a crucial point for the science verification of the LST-1 and, in turn, of the Northern Array of the CTAO.

The results of this thesis work confirm what the MAGIC Collaboration found in 2020: the VHE emission originates far from the neutron star surface, in the outer region of the magnetosphere, and the most probable acceleration mechanism for the particles emitting in the VHE is Inverse Compton scattering, which is responsible for the power law spectrum of P2. Not only the MAGIC results were confirmed, but it was also possible to fit the P2 pulse profile for the first time at these energies, thanks to the higher statistic of LST-1 observations. After fitting with a symmetric Gaussian, a model implying that the pulses have the same time when rising and descending, the FWHM of the peak was derived and the value was compared to the ones obtained by *Fermi*-LAT at lower energies. The decreasing trend of the FWHM with the energy that *Fermi*-LAT found was confirmed. This study also allowed the derivation of the time delay between the P2 emission at a few GeV and tens of GeV. It was found to be 27 μs, indicating a similar acceleration site for the particles emitting the observed γ rays at a few and tens of GeV energies.

From the joint fit with *Fermi*-LAT and MAGIC data, the power law with an exponential cutoff model was discarded and this is compatible with the previous results of

both MAGIC and *Fermi*-LAT. This means that the classic versions of Outer Gap models for sure is not able to explain the VHE emission of Geminga. The power law with sub-exponential cutoff, instead, could not be discarded yet. In the future, additional statistical tests for non-nested models, such as the PLSEC plus the power law, can be used to better understand what the dominant model is.

A qualitative comparison with the theoretical predictions of a modified Outer Gap model showed good compatibility with the data in the LST-1 energy range, but the *Fermi*-LAT flux is underpredicted by the model. This shows the limitations of the modified OG models to fully explain the γ-ray emission from Geminga from MeV to GeV energies.

This thesis was mainly aimed at the science verification of the instrument and, with respect to the MAGIC Collaboration results, only the analysis of the FWHM was added. In general, more observations are needed to increase the statistics of the study and only by combining a more refined analysis including a larger sample of hours with *Fermi*-LAT results then it will be possible to obtain better results. More hours of observations will allow for increasing the statistic of P2, improving the uncertainties on the spectral parameters and refining the upper limit on the last energy bin. The latter improvement is relevant because it would provide a better constraining of the spectral cutoff at higher energies. Determining if a cutoff at energies of $\sim$100 GeV is present would be a turning point: the extension of the emission at higher energies would highlight the presence of additional mechanisms inside the magnetosphere, such as the Inverse Compton scattering between the accelerated particles and the soft X-ray photons coming from the neutron star surface. Not only that, but more observational hours are essential for the detection of P1 at VHEs: this has not been done before and it would be important to derive a spectrum for the first peak to carry out a more complete study on the emission.

It is worth noticing that all the results shown in this thesis were obtained only considering the statistical errors and, for a full study, the systematics should be taken into account. They include all the possible variations in the measurements that do not vary randomly from one point to the others. Examples of systematic effects that should be investigated in this context are the mismatches between the MC simulated data and the real data, the different weather conditions, the flat fielding of the camera and the mispointings of the telescope. They cannot be reduced just by increasing the observing time; to limit their effect one should, for example, improve the matching between the MC and real data, or simulate different weather conditions to study the response of the instrument. Systematics can play a fundamental role in determining the final values of the associated errors with the parameters and their study will be completed in the future.

Conclusions

This thesis was developed in the context of Very-High Energy astrophysics, a field that has been gaining more importance in the last couple of decades and that can be considered as the crossroad between astronomy and particle physics.

The VHE domain of γ rays is typically assumed to start at around 50 GeV and end at around 100 TeV. The most relevant emission mechanisms producing photons at these energies are synchrotron and curvature radiation, the process linked to the emission of γ-ray pulsars, Inverse Compton scattering, commonly observed in Blazars, neutral pion decay, particularly relevant for the air showers, and, in some cases, bremsstrahlung. Unlike usual high-energy observations, the TeV band is mainly explored from the ground due to the strong limitations of space telescopes in observing such energetic photons. γ rays, when they enter Earth's atmosphere, interact through pair production with particles and generate electromagnetic showers of electrons, positrons and secondary photons travelling at a speed larger than that of light inside the atmosphere. As a consequence, the shower particles emit Cherenkov radiation that is observed as a nanoseconds-long beam of optical blue light. Ground-based facilities are able to indirectly detect γ-rays by studying the electromagnetic showers they produce since their features are strictly linked to the main characteristic of the γ ray that initiated them. Two main approaches can be used: either a direct detection of the particles or by studying the Cherenkov light produced by the shower in the atmosphere. In particular, the latter technique is at the basis of the functioning of Imaging Atmospheric Cherenkov Telescopes (IACTs). IACTs are made of one or more optical mirror dishes coupled with a pixelized camera, usually composed of Photomultiplier Tubes (PMTs) to guarantee a high temporal resolution to the instrument. Single Cherenkov telescopes are quite limited in reconstructing the image of an atmospheric shower and, for this reason, the stereoscopic technique has been developed. Following this method, several IACTs are placed together in an array so that they observe the same shower and the reconstruction is more accurate. The three currently operating IACT arrays, MAGIC, H.E.S.S. and VERITAS, proved the technique to be extremely useful in studying the VHE band, even though these instruments still have limited performances and can only reach energies up to a few tens of TeV. The upcoming facility for the ground-based detection of γ-rays is the Cherenkov Telescope Array Observatory (CTAO) and it is expected to boost the knowledge of the

VHE band thanks to its improved performances (see Chapter 2 for more details) and to the large energy coverage from 20 GeV to 300 TeV, a range never covered before by a single facility. To reach this goal, the two arrays (one in the Northern and the other in the Southern hemispheres) of CTAO will be composed of telescopes with three different designs and dimensions. The Large-Sized Telescope (LST) is the largest of the three, with a diameter of 23 meters, and it is the one optimised for the lowest energy range, between 20 GeV and 200 GeV. Moreover, it can be repointed in only 20 seconds from any alert coming from other worldwide facilities. For these reasons, it will be focused on extragalactic sources, transient, and pulsars. The first LST of the Northern Array, the so-called LST-1, has seen its first light in 2019 and already shows the potentialities of the future CTAO. This thesis contributed to the analysis of the LST-1 performance when working at the very lowest boundary of VHEs, in addition to the scientific aim of studying VHE pulsars.

The Very-High Energy sky is populated by more than 250 sources, half of them Galactic and the other half extragalactic. Among them, one can find pulsars, Pulsar Wind Nebulae, Supernova Remnants, Active Galactic Nuclei, and Gamma Ray Bursts. In particular, this thesis is focused on pulsars, which were discovered to be γ-ray emitters a few decades ago and at the moment around 300 neutron stars are known to show γ-ray pulses. Several models have been proposed to explain the detection of pulses in the γ rays, and the majority of them rely on the assumption of curvature radiation at the main emission mechanism. Observations with *Fermi*-LAT found that, in the vast majority of the cases, pulsars are characterised by a double-peaked light curve and a power law spectrum with an exponential cutoff at a few GeV. This led to the rejection of Polar Cap models, which predicted a spectrum characterized by a sharp super-exponential cutoff (see Chapter 3). Nowadays, the most accepted theory on the γ-ray emission of pulsars is the so-called Outer Gap model, which locates the acceleration site in the outer region of the magnetosphere and predicts a power law spectrum with an exponential cutoff. Concerning the VHE emission of γ-ray pulsars, a significant amount of uncertainties are in place: only three sources have been detected and none of the traditional models, not even the Outer Gap, seems to be able to fully explain the observations from MeV to TeV energies. Additional mechanisms, such as the Inverse Compton scattering, could contribute at energies higher than a few tens of GeV, but additional studies with more advanced instruments are needed to prove it.

The object of study of this thesis is Geminga, a middle-aged ($\tau_c \sim 3 \cdot 10^5$ yr) γ-ray pulsar discovered for the first time in 1972. It was detected thanks to its high energy emission, both in the γ rays and in the X-ray band, due to the absence of radio pulses (recent results at a frequency of 11 MHz returned an upper limit to the average flux density of 0.4-4 mJy) and it is between the most studied γ-ray pulsars. Its high-energy emission is characterised by different pulse shapes depending on the energy, reflecting the different emission mechanisms at play: the light curve changes from a single broad pulse in the soft X-rays (thermal emission from the neutron star) to a double-peaked curve in

the hard X-rays and γ-rays (non-thermal synchrotron). In 2020, Geminga became the third γ-ray pulsar ever detected at VHE, thanks to the results of the MAGIC Collaboration; it is also the second pulsar detected by the LST-1 after the Crab. The telescope detected it in December 2022 and regular observations followed in 2023. Understanding more about the VHE emission of Geminga is relevant due to the fact that it is one of the only three pulsars known to emit at these energies. Since the mechanisms responsible for the detection of VHE pulses are not well understood, the more studies carried out on the topic the more knowledge can be derived. Not only that, but Geminga is also a middle-aged pulsar, much older than the Crab and the Vela pulsars, and by studying its VHE emission and comparing it to the results for the other two one could try to see if and how the radiation in the γ rays evolves with the age of the neutron star.

The dataset analysed in this work consists of 21 hours of good-quality data with a zenith cut at 25°, a value chosen to guarantee the lowest possible analysis energy threshold. Indeed, when a shower is observed closer to the zenith, the layer of atmosphere that it must cross is smaller; as a consequence, the photon density of the Cherenkov pool on the ground becomes higher and the energy threshold is lower when compared to a shower observed closer to the horizon. The analysis of the data resulted in the computation of both the phaseogram, the histogram of the phases, and the spectrum of the second peak of the light curve (P2). The study of the peaks and their geometry is relevant in order to have an idea of the acceleration site of the particles emitting the radiation and to see if there are differences with respect to the other electromagnetic bands. Instead, the spectral analysis of the peaks allows the identification of the emission mechanism generating the radiation and the discrimination between the different theoretical models.

The analysis of the phaseogram allowed the estimation of the detection significance of the signal: P2 was detected at an 8σ significance, while the first peak P1, with a significance of 2σ, remained undetected. The MAGIC Collaboration previously detected P2 with a 6.3σ significance analysing 80 hours of data cut at 25° zenith angle [84]. The result of this thesis is striking and it represents evidence of the excellent performance of the LST-1 when working at the lowest edge of the VHE band: with one-fourth of the hours and using just one telescope, the significance of P2 was higher than that obtained by MAGIC. Thanks to the high significance of the P2 signal, it was also possible to fit the pulse profile to derive the FWHM for the first time at VHE. Obtaining the value of the FWHM was a significant step ahead because, when compared to the same result at different energies, one can have a better idea of the acceleration site of the particles. The comparison of the FWHM of the LST-1 analysis with previous *Fermi*-LAT data at lower energies returned a very small value of the delay $\Delta\tau$, suggesting similar acceleration sites for the particles emitting γ rays at a few GeV (*Fermi*-LAT) and at tens of GeV (LST-1).

The spectral analysis of P2 showed that the best model to fit the LST-1 data is a power law with a spectral index $\Gamma = 5.5 \pm 1.1$, compatible with what the MAGIC Collaboration found. A joint fit with *Fermi*-LAT and MAGIC data was performed to better understand the mechanism at the basis of the emission; the power law with an

exponential cutoff (PLEC) spectral model was excluded at the 19.7σ level in favour of a power law with a sub-exponential cutoff (PLSEC), hence excluding the classical Outer Gap models in favour of more complicated modified versions of this theory which imply that the acceleration sites are even farther away from the neutron star surface. The low energies at play made it not possible to draw conclusions on the emission mechanism responsible for the detected VHE emission; additional statistical tests for non-nested models will be used in the future to understand if the PLSEC model or others, such as the PLSEC plus a power law, can explain the observed emission. These new tests will be crucial since the presence of a power law tail would suggest the need for a new mechanism, probably Inverse Compton scattering, emerging above a certain value of energy.

This thesis has several future prospects to improve the study of Geminga at VHEs. First of all, additional observations will be of crucial importance for the analysis. By increasing the number of observational hours, the statistics of the study will improve: this will lower the statistical errors associated with the parameters of the tested spectral models[2] and will increase the significance of both P1 and P2. An improved significance of P2 implies that more complicated curves can be tested in the fit of the pulse profile; one example could be an asymmetric Gaussian highlighting different times during the rise and the descending of the pulse. As previously shown, in $\sim$70 hours of observations with the mean zenith angle lower than 15°, P1 could be detected for the first time at these energies and this would allow a more complete picture of the emission at VHEs since the same study performed on P2 could be repeated on P1 to derive the spectrum and the FWHM of the pulse profile. Not only, but additional hours can help to understand if the upper limit on the spectrum that was obtained with the current analysis is constraining: by increasing the observing time, the upper limit can become a proper flux point and, in this way, it will be possible to see if there is a cutoff around $\sim$100 GeV or if Geminga can be observed at even higher energies.

Another essential point is to investigate the effect of systematics on the dataset. This could not be carried out for this thesis because of the short time available, but the study of systematics must be included to have a clear and complete picture of the uncertainties in the analysis. It will be done in the future when more observations will be performed, for example by applying different cuts in efficiency during the data reduction procedure. When the systematics are analysed, a better comparison with the MAGIC Collaboration results, which included the effect of systematic uncertainties, can be performed.

Some of the results of this thesis were presented at the 38th International Cosmic Ray Conference in August 2023 and are included in the proceedings paper *"First results of pulsar observations with the LST-1"* [103], along with the analysis of the Crab pulsar

[2]For now, it is not possible to estimate how much the error will improve because several factors, such as the migration matrix describing the relation between E_{true} and E_{reco}, can influence the statistical errors.

data. Moreover, Mr. A. Mas-Aguilar completed an independent analysis on the same dataset as this thesis, obtaining consistent results with the ones presented here within the errors. Both analyses will be used to cross-check the results for the internal review by the CTA-LST Collaboration. After the data analysis including the future observations, a paper including the complete study of Geminga will be published.

The field of VHE pulsars is still in development and more studies are needed to understand if the mechanisms powering the emission at VHE are the same generating the γ rays at lower energies or if additional processes are responsible for the radiation in the TeV domain. With the advent of CTAO, in particular of the Northern Array that will include 4 LSTs, more VHE pulsars are expected to be detected, but the number of hours needed for the detection could change from object to object.

In conclusion, this first study of the VHE γ-ray emission of the Geminga pulsar reinforced the previous MAGIC results and improved them, thanks to the better performance of the LST-1 at low energies with respect to the MAGIC array. The usual Outer Gap models, even when modified, are not able to fully explain the observed spectrum from MeV to GeV energies and the low energies at play do not allow a clear distinction between the available theoretical models. The incapability of OG models to explain the spectrum points toward the presence of a new emission mechanism, most likely the Inverse Compton scattering between the soft X-ray photons coming from the neutron star surface and the relativistic particles accelerated inside the magnetosphere, but the systematic uncertainty study and non-nested joint fit are needed to make such a claim. Geminga is an intriguing γ-ray pulsar, emitting in the VHE despite its middle age and without any significant radio emission, and deeper studies are required to shed more light on the radiation processes producing the observed γ rays. The LST-1 brought significant improvements when compared to its predecessors, and CTAO, in particular its Northern Array, will be of fundamental importance in the next decades to increase the number of known VHE γ-ray pulsars and finally understand the physics behind their emission.

Bibliography

[1] T.C. Weekes et al. "Observation of TeV Gamma Rays from the Crab Nebula Using the Atmospheric Cerenkov Imaging Technique". In: *The Astrophysical Journal* 342 (July 1989), pp. 379–395. DOI: 10.1086/167599.

[2] M. S. Longair. *High Energy Astrophysics*. Third. Cambridge University Press, 2011. DOI: 10.1017/CBO9780511778346.

[3] R. M. Wagner. "Measurement of Very High Energy Gamma-Ray Emission from Four Blazars Using the MAGIC Telescope and a Comparative Blazar Study". PhD thesis. Technische Universität München, 2006.

[4] D. Heck et al. *CORSIKA: a Monte Carlo code to simulate extensive air showers*. Feb. 1998.

[5] J. Matthews. "A Heitler model of extensive air showers". In: *Astroparticle Physics* 22.5 (Jan. 2005), pp. 387–397. DOI: 10.1016/j.astropartphys.2004.09.003.

[6] R. Engel, D. Heck, and T. Pierog. "Extensive Air Showers and Hadronic Interactions at High Energy". In: *Annual Review of Nuclear and Particle Science* 61.1 (Nov. 2011), pp. 467–489. DOI: 10.1146/annurev.nucl.012809.104544.

[7] G. Moliere. "Theorie der Streuung schneller geladener Teilchen II Mehrfach-und Vielfachstreuung". In: *Zeitschrift für Naturforschung A* 3.2 (Feb. 1948), pp. 78–97. DOI: 10.1515/zna-1948-0203.

[8] P. A. Cherenkov. "Visible luminescence of pure liquids under the influence of γ-radiation". In: *Dokl. Akad. Nauk SSSR* 2.8 (May 1934), pp. 451–454. DOI: 10.3367/UFNr.0093.196710n.0385.

[9] J. V. Jelley. "Cherenkov radiation and its applications". In: *British Journal of Applied Physics* 6.7 (July 1955), pp. 227–232. DOI: 10.1088/0508-3443/6/7/301.

[10] J. V. Jelley. "The Atmospheric Cherenkov Technique in γ -ray Astronomy: The Early Days". In: *Philosophical Transactions of the Royal Society of London. Series A, Mathematical and Physical Sciences* 301.1462 (June 1981), pp. 611–614. URL: http://www.jstor.org/stable/37066.

[11] W.-M. Yao et al. "Review of Particle Physics". In: *Journal of Physics G: Nuclear and Particle Physics* 33.1 (July 2006). DOI: 10.1088/0954-3899/33/1/001.

[12] W. Bednarek and M. Bartosik. "Gamma-rays from the pulsar wind nebulae". In: *Astronomy & Astrophysics* 405.2 (June 2003), pp. 689–702. DOI: 10.1051/0004-6361:20030593.

[13] S. Funk. "VHE Gamma-ray supernova remnants". In: *Advances in Space Research* 41 (Jan. 2008), pp. 464–472. DOI: 10.1016/j.asr.2007.04.076.

[14] H.E.S.S. Collaboration, F. Aharonian, et al. "First detection of a VHE gamma-ray spectral maximum from a cosmic source: HESS discovery of the Vela X nebula". In: *Astronomy & Astrophysics* 448.2 (Mar. 2006), pp. L43–L47. DOI: 10.1051/0004-6361:200600014.

[15] F. Aharonian et al. "Evidence for TeV gamma-ray emission from Cassiopeia A". In: *Astronomy & Astrophysics* 370.1 (Apr. 2001), pp. 112–120. DOI: 10.1051/0004-6361:20010243.

[16] C. B. Adams et al. "Observation of the Gamma-Ray Binary HESS J0632+057 with the H.E.S.S., MAGIC, and VERITAS Telescopes". In: *The Astrophysics Journal* 923.2 (Dec. 2021), p. 241. DOI: 10.3847/1538-4357/ac29b7.

[17] The Fermi-LAT Collaboration, A. A. Abdo, et al. "Gamma-Ray Emission Concurrent with the Nova in the Symbiotic Binary V407 Cygni". In: *Science* 329.5993 (Aug. 2010), pp. 817–821. DOI: 10.1126/science.1192537.

[18] V. A. Acciari et al. "Proton acceleration in thermonuclear nova explosions revealed by gamma rays". In: *Nature Astronomy* 6.6 (Apr. 2022), pp. 689–697. DOI: 10.1038/s41550-022-01640-z.

[19] H.E.S.S. Collaboration, F. Aharonian, et al. "Time-resolved hadronic particle acceleration in the recurrent nova RS Ophiuchi". In: *Science* 376.6588 (Mar. 2022), pp. 77–80. DOI: 10.1126/science.abn0567.

[20] MAGIC Collaboration, J. Albert, et al. "Observation of Gamma Rays from the Galactic Center with the MAGIC Telescope". In: *The Astrophysical Journal Letters* 638.2 (Jan. 2006), pp. L101–L104. DOI: 10.1086/501164.

[21] H.E.S.S. Collaboration, A. Abramowski, et al. "Acceleration of Petaelectronvolt protons in the Galactic Centre". In: *Nature* 531 (Mar. 2016), pp. 476–479. DOI: 10.1038/nature17147.

[22] C. M. Urry and P. Padovani. "Unified Schemes for Radio-Loud Active Galactic Nuclei". In: *Publications of the Astronomical Society of the Pacific* 107.715 (Sept. 1995), pp. 803–845. DOI: 10.1086/133630.

[23] C. E. Fichtel. "High-Energy Gamma-Ray Observations of Active Galaxies". In: *The Astrophysical Journal Supplement Series* 90 (Feb. 1994), pp. 917–922. DOI: 10.1086/191925.

[24] MAGIC collaboration, J. Aleksić, et al. "Discovery of VHE s from the blazar 1ES 1215+303 with the MAGIC telescopes and simultaneous multi-wavelength observations". In: *Astronomy & Astrophysics* 544 (Aug. 2012), A142. DOI: 10.1051/0004-6361/201219133.

[25] VERITAS Collaboration, V. A. Acciari, et al. "A connection between star formation activity and cosmic rays in the starburst galaxy M82". In: *Nature* 462.7274 (Dec. 2009), pp. 770–772. DOI: 10.1038/nature08557.

[26] H.E.S.S. Collaboration, F. Acero, et al. "Detection of Gamma Rays from a Starburst Galaxy". In: *Science* 326.5956 (Nov. 2009), pp. 1080–1082. DOI: 10.1126/science.1178826.

[27] C. Kouveliotou et al. "Identification of Two Classes of Gamma-Ray Bursts". In: *The Astrophysical Journal Letters* 413 (Aug. 1993), pp. L101–L104. DOI: 10.1086/186969.

[28] A. Levan et al. "Gamma-Ray Burst Progenitors". In: *Space Science Reviews* 202.1-4 (Nov. 2016), pp. 33–78. DOI: 10.1007/s11214-016-0312-x.

[29] MAGIC Collaboration, V. A. Acciari, et al. "Teraelectronvolt emission from the γ-ray burst GRB 190114C". In: *Nature* 575.7783 (Nov. 2019), pp. 455–458. DOI: 10.1038/s41586-019-1750-x.

[30] J. Sitarek. "TeV Instrumentation: Current and Future". In: *Galaxies* 10.1 (Jan. 2022), p. 21. DOI: 10.3390/galaxies10010021.

[31] HAWC Collaboration, A. U. Abeysekara, et al. "The HAWC Gamma-Ray Observatory: Design, Calibration, and Operation". In: *arXiv e-prints* (Sept. 2013), arXiv:1310.0074. DOI: 10.48550/arXiv.1310.0074. eprint: 1310.0074.

[32] X.-H. Ma et al. "Chapter 1 LHAASO Instruments and Detector technology". In: *Chinese Physics C* 46.3 (Mar. 2022), p. 030001. DOI: 10.1088/1674-1137/ac3fa6.

[33] J. A. Hinton. "The status of the H.E.S.S. project". In: *New Astronomy Reviews* 48.5-6 (Apr. 2004), pp. 331–337. DOI: 10.1016/j.newar.2003.12.004.

[34] J. Aleksić et al. "The major upgrade of the MAGIC telescopes, Part I: The hardware improvements and the commissioning of the system". In: *Astroparticle Physics* 72 (Jan. 2016), pp. 61–75. DOI: 10.1016/j.astropartphys.2015.04.004.

[35] J. Aleksić et al. "The major upgrade of the MAGIC telescopes, Part II: A performance study using observations of the Crab Nebula". In: *Astroparticle Physics* 72 (Jan. 2016), pp. 76–94. DOI: 10.1016/j.astropartphys.2015.02.005.

[36] J. Holder et al. "The first VERITAS telescope". In: *Astroparticle Physics* 25.6 (July 2006), pp. 391–401. DOI: 10.1016/j.astropartphys.2006.04.002.

[37] D. Mazin et al for the CTA LST Project. "Status and results of the prototype LST of CTA". In: *Proceedings of 37th International Cosmic Ray Conference — PoS(ICRC2021)*. July 2021. DOI: 10.22323/1.395.0872.

[38] J. Cortina for the CTA LST project. "Status of the Large Size Telescopes of the Cherenkov Telescope Array". In: *Proceedings of the 36th International Cosmic Ray Conference - PoS (ICRC2019)*. 2019. eprint: 1907.10146.

[39] Y. Kobayashi et al for the CTA LST project. "Camera Calibration of the CTA-LST prototype". In: *Proceedings of 37th International Cosmic Ray Conference — PoS(ICRC2021)*. July 2021. DOI: 10.22323/1.395.0720.

[40] M. Heller et al for the CTA LST Project. "Development of an advanced SiPM camera for the Large Size Telescope of the Cherenkov Telescope Array Observatory". In: *Proceedings of 37th International Cosmic Ray Conference — PoS(ICRC2021)*. Vol. 395. July 2021, p. 889. DOI: 10.22323/1.395.0889.

[41] J. L. Contreras et al. "Data model issues in the Cherenkov Telescope Array project ". In: *Proceedings of The 34th International Cosmic Ray Conference - PoS(ICRC2015)*. Vol. 236. 2016, p. 960. DOI: 10.22323/1.236.0960.

[42] R. López-Coto et al. "`lstchain`: An Analysis Pipeline for LST-1, the First Prototype Large-Sized Telescope of CTA". In: *Astronomical Society of the Pacific Conference Series*. Vol. 532. July 2022, p. 357.

[43] C. Deil, R. Zanin, J. Lefaucheur, et al. *Gammapy - A prototype for the CTA science tools*. 2017. arXiv: 1709.01751 [astro-ph.IM].

[44] A. Hewish et al. "Observation of a Rapidly Pulsating Radio Source". In: *Nature* 217.5130 (Feb. 1968), pp. 709–713. DOI: 10.1038/217709a0.

[45] F. Pacini. "Rotating Neutron Stars, Pulsars and Supernova Remnants". In: *Nature* 219.5150 (July 1968), pp. 145–146. DOI: 10.1038/219145a0.

[46] D. H. Staelin and E. C. Reifenstein. "Pulsating Radio Sources near the Crab Nebula". In: *Science* 162.3861 (Dec. 1968), pp. 1481–1483. DOI: 10.1126/science.162.3861.1481.

[47] R. Browning, D. Ramsden, and P. J. Wright. "Detection of Pulsed Gamma Radiation from the Crab Nebula". In: *Nature Physical Science* 232.31 (Aug. 1971), pp. 99–101. DOI: 10.1038/physci232099a0.

[48] A. K. Harding. "The neutron star zoo". In: *Frontiers of Physics* 8.6 (Dec. 2013), pp. 679–692. DOI: 10.1007/s11467-013-0285-0.

[49] T. Gold. "Rotating neutron stars as the origin of the pulsating radio sources". In: *Nature* 218 (May 1968), pp. 731–732. DOI: 10.1038/218731a0.

[50] B. M. Gaensler and P. O. Slane. "The Evolution and Structure of Pulsar Wind Nebulae". In: *Annual Review of Astronomy and Astrophysics* 44.1 (Sept. 2006), pp. 17–47. DOI: 10.1146/annurev.astro.44.051905.092528.

[51] J. P. Ostriker and J. E. Gunn. "On the Nature of Pulsars. I. Theory". In: *The Astrophysics Journal* 157 (Sept. 1969), pp. 1395–1417. DOI: 10.1086/150160.

[52] P. Goldreich and W. H. Julian. "Pulsar Electrodynamics". In: *The Astrophysical Journal* 157 (Aug. 1969), pp. 869–880. DOI: 10.1086/150119.

[53] D. A. Kniffen et al. "Gamma radiation from the Crab Nebula above 35 MeV". In: *Nature* 251.5474 (Oct. 1974), pp. 397–399. DOI: 10.1038/251397a0.

[54] D. J. Thompson et al. "SAS-2 high-energy gamma-ray observations of the Vela pulsar." In: *The Astrophysical Journal Letters* 200 (Sept. 1975), pp. L79–L82. DOI: 10.1086/181902.

[55] C. E. Fichtel et al. "High-energy gamma-ray results from the second Small Astronomy Satellite." In: *The Astrophysical Journal* 198 (May 1975), pp. 163–182. DOI: 10.1086/153590.

[56] A. A. Abdo et al. "THE SECOND FERMI LARGE AREA TELESCOPE CATALOG OF GAMMA-RAY PULSARS". In: *The Astrophysical Journal Supplement Series* 208.2 (Sept. 2013), pp. 17–75. DOI: 10.1088/0067-0049/208/2/17.

[57] P. A. Caraveo. "Gamma-Ray Pulsar Revolution". In: *Annual Review of Astronomy and Astrophysics* 52.1 (Aug. 2014), pp. 211–250. DOI: 10.1146/annurev-astro-081913-035948.

[58] K. Hirotani. "High Energy Emission from Rotation-Powered Pulsars: Outer-gap vs. Slot-gap Models". In: *ArXiv e-prints* (2008). arXiv: 0809.1283 [astro-ph].

[59] P. A. Sturrock. "A Model of pulsars". In: *The Astrophysical Journal* 164 (Mar. 1971), pp. 529–556. DOI: 10.1086/150865.

[60] MAGIC Collaboration. "Observation of Pulsed γ-Rays Above 25 GeV from the Crab Pulsar with MAGIC". In: *Science* 322.5905 (2008), pp. 1221–1224. DOI: 10.1126/science.1164718.

[61] J. Arons. "Pair creation above pulsar polar caps: geometrical structure and energetics of slot gaps." In: *The Astrophysical Journal* 266 (Mar. 1983), pp. 215–241. DOI: 10.1086/160771.

[62] E. T. Scharlemann, J. Arons, and W. M. Fawley. "Potential drops above pulsar polar caps: ultrarelativistic particle acceleration along the curved magnetic field." In: *The Astrophysical Journal* 222 (May 1978), pp. 297–316. DOI: 10.1086/156144.

[63] K. S. Cheng, C. Ho, and Malvin A. Ruderman. "Energetic Radiation from Rapidly Spinning Pulsars. 1. Outer Magnetosphere Gaps. 2. Vela and Crab". In: *The Astrophysical Journal* 300 (Jan. 1986), pp. 500–539. DOI: 10.1086/163829.

[64] Isabelle A. Grenier and Alice K. Harding. "Gamma-ray pulsars: A gold mine". In: *Comptes Rendus Physique* 16.6 (2015), pp. 641–660. DOI: 10.1016/j.crhy.2015.08.013.

[65] F. A. Aharonian, S. V. Bogovalov, and D. Khangulyan. "Abrupt acceleration of a 'cold' ultrarelativistic wind from the Crab pulsar". In: *Nature* 482 (Feb. 2012), pp. 507–509. DOI: 10.1038/nature10793.

[66] P. A. Caraveo et al. "Parallax Observations with the Hubble Space Telescope Yield the Distance to Geminga". In: *The Astrophysical Journal Letters* 461 (Apr. 1996), pp. L91–L94. DOI: 10.1086/310012.

[67] J. Faherty, F. M. Walter, and J. Anderson. "The trigonometric parallax of the neutron star Geminga". In: *Astrophysics and Space Science* 308.1-4 (Apr. 2007), pp. 225–230. DOI: 10.1007/s10509-007-9368-0.

[68] D. J. Thompson et al. "Final SAS-2 gamma-ray results on sources in the galactic anticenter region." In: *The Astrophysical Journal* 213 (Apr. 1977), pp. 252–262. DOI: 10.1086/155152.

[69] J. L. Masnou et al. "Search for Gamma-Ray Time Variability of Cygnus X-3 and CG 195+4". In: *Recent Advances in Gamma-Ray Astronomy*. Vol. 124. ESA Special Publication. July 1977, p. 33.

[70] R. C. Lamb and D. M. Worrall. "X-ray emission from the region of gamma 195 + 5". In: *The Astrophysical Journal Letters* 231 (Aug. 1979), pp. L121–L124. DOI: 10.1086/183017.

[71] G. F. Bignami, P. A. Caraveo, and R. C. Lamb. "An identification for "GEMINGA" (2CG 195+04) 1E 0630+178: a unique object in the error box of the high-energy gamma-ray source." In: *The Astrophysical Journal Letters* 272 (Sept. 1983), pp. L9–L13. DOI: 10.1086/184107.

[72] J. P. Halpern and D. Tytler. "The Geminga X-Ray Counterpart and a Blue Optical Identification". In: *The Astrophysical Journal* 330 (July 1988), pp. 201–217. DOI: 10.1086/166467.

[73] J. P. Halpern and S. Holt. "Discovery of soft X-ray pulsations from the γ-ray source Geminga". In: *Nature* 357 (May 1992), pp. 222–224. DOI: 10.1038/357222a0.

[74] D. Bertsch et al. "Pulsed high-energy γ-radiation from Geminga (1E0630+178)". In: *Nature* 357 (May 1992), pp. 306–307. DOI: 10.1038/357306a0.

[75] Kaya Mori et al. "A BROADBAND X-RAY STUDY OF THE GEMINGA PULSAR WITH NuSTAR AND XMM-NEWTON". In: *The Astrophysical Journal* 793.2 (Sept. 2014), p. 88. DOI: 10.1088/0004-637X/793/2/88.

[76] E. Aliu et al. "A SEARCH FOR PULSATIONS FROM GEMINGA ABOVE 100 GeV WITH VERITAS". In: *The Astrophysical Journal* 800.1 (Feb. 2015), pp. 61–67. DOI: 10.1088/0004-637x/800/1/61.

[77] M. L. Ahnen et al. "Search for VHE gamma-ray emission from Geminga pulsar and nebula with the MAGIC telescopes". In: *Astronomy & Astrophysics* 591 (July 2016), A138. DOI: 10.1051/0004-6361/201527722.

[78] A. U. Abeysekara et al. "Extended gamma-ray sources around pulsars constrain the origin of the positron flux at Earth". In: *Science* 358.6365 (Nov. 2017), pp. 911–914. DOI: 10.1126/science.aan4880.

[79] M. Spir-Jacob et al for H.E.S.S. Collaboration. "Detection of sub-100 GeV γ-ray pulsations from PSR B1706-44 with H.E.S.S". In: *Proceedings of the 36th International Cosmic Ray Conference - PoS(ICRC2019)*. Aug. 2019. arXiv: 1908.06464.

[80] A. A. Ershov. "On the Radio Emission of the Geminga Pulsar and RBS 1223 at the Frequency of 111 MHz". In: *Bulletin of the Lebedev Physics Institute* 48.4 (June 2021), pp. 114–118. DOI: 10.3103/S1068335621040023.

[81] G. F. Bignami and P. A. Caraveo. "GEMINGA: Its Phenomenology, Its Fraternity, and Its Physics". In: *Annual Review of Astronomy and Astrophysics* 34.1 (Sept. 1996), pp. 331–381. DOI: 10.1146/annurev.astro.34.1.331.

[82] J. M. Fierro et al. "Phase-resolved Studies of the High-Energy Gamma-Ray Emission from the Crab, Geminga, and Vela Pulsars". In: *The Astrophysical Journal* 494.2 (Feb. 1998), pp. 734–746. DOI: 10.1086/305219.

[83] Fermi-LAT Collaboration, A. A. Abdo, et al. "FERMI-LAT OBSERVATIONS OF THE GEMINGA PULSAR". In: *The Astrophysical Journal* 720.1 (Aug. 2010), pp. 272–283. DOI: 10.1088/0004-637x/720/1/272.

[84] MAGIC Collaboration, V. A. Acciari, et al. "Detection of the Geminga pulsar with MAGIC hints at a power-law tail emission beyond 15 GeV". In: *Astronomy & Astrophysics* 643 (Nov. 2020), p. L14. DOI: 10.1051/0004-6361/202039131.

[85] R. López-Coto et al. *cta-observatory/cta-lstchain: v 0.9.13 - 2022-01-24*. Version v0.9.13. Jan. 2023. DOI: 10.5281/zenodo.7565826.

[86] A. Donath et al. *Gammapy: Python toolbox for gamma-ray astronomy*. Version v 0.20. This research made use of Gammapy, a community-developed core Python package for gamma-ray astronomy. `https://ui.adsabs.harvard.edu/abs/2017ICRC...35..766D/abstract`. May 2022. DOI: 10.5281/zenodo.6552377.

[87] J. Luo et al. "PINT: A Modern Software Package for Pulsar Timing". In: *The Astrophysical Journal* 911.1 (Apr. 2021), p. 45. DOI: 10.3847/1538-4357/abe62f.

[88] V.P. Fomin et al. "New methods of atmospheric Cherenkov imaging for gamma-ray astronomy. I. The false source method". In: *Astroparticle Physics* 2.2 (May 1994), pp. 137–150. DOI: 10.1016/0927-6505(94)90036-1.

[89] R. Zanin. "Observations of the Crab pulsar wind nebula and microquasar candidates with MAGIC". Available at `http://hdl.handle.net/10803/51492`. PhD thesis. Universitat Autonoma de Barcelona, 2011.

[90] A. M. Hillas and J. R. Patterson. "Characteristics and brightness of Cerenkov shower images for gamma-ray astronomy near 1 TeV". In: *Journal of Physics G Nuclear Physics* 16.8 (Aug. 1990), pp. 1271–1281. DOI: 10.1088/0954-3899/16/8/022.

[91] J. E. Ruiz et al. *`LSTOSA`: Onsite processing pipeline for the CTA Larged-Sized Telescope prototype*. 2021. arXiv: 2101.09690.

[92] A. M. Hillas. "Cerenkov Light Images of EAS Produced by Primary Gamma Rays and by Nuclei". In: *Proceedings of the 19th International Cosmic Ray Conference (ICRC19)*. Vol. 3. Aug. 1985, pp. 445–448.

[93] E. Garcia, T. Vuillaume, and L. Nickel. *The `lstMCpipe` library*. 2022. arXiv: 2212.00120 [astro-ph.IM].

[94] A. Moralejo. *Grid of directions for the MC test set*. `https://github.com/cta-observatory/lst-sim-config/issues/2`.

[95] G. Ceribella. "Insights into the 10-100 GeV gamma-ray emission of pulsars from extensive observations of MAGIC". Available at `https://mediatum.ub.tum.de/?id=1617483`. PhD thesis. Technische Universität München, 2021.

[96] Á. Mas-Aguilar. *PulsarTimingAnalysis*. Version v0.2. `https://github.com/alvmas/PulsarTimingAnalysis`.

[97] T. P. Li and Y. Q. Ma. "Analysis methods for results in gamma-ray astronomy." In: *The Astrophysical Journal* 272 (Sept. 1983), pp. 317–324. DOI: 10.1086/161295.

[98] S. S. Wilks. *Mathematical Statistics*. John Wiley & Sons, 1962.

[99] R. Buccheri et al. "Search for pulsed γ-ray emission from radio pulsars in the COS-B data." In: *Astronomy and Astrophysics* 128 (Dec. 1983), pp. 245–251.

[100] O. C. de Jager, B. C. Raubenheimer, and J. W. H. Swanepoel. "A powerful test for weak periodic signals with unknown light curve shape in sparse data." In: *Astronomy and Astrophysics* 221 (Aug. 1989), pp. 180–190.

[101] O. C. de Jager and I. Büsching. "The H-test probability distribution revisited: improved sensitivity". In: *Astronomy and Astrophysics Letters* 517 (July 2010), p. L9. DOI: 10.1051/0004-6361/201014362.

[102] S. Abdollahi, F. Acero, et al. "Incremental Fermi Large Area Telescope Fourth Source Catalog". In: *The Astrophysical Journal Supplement Series* 260.2 (June 2022), p. 53. DOI: 10.3847/1538-4365/ac6751.

[103] A. Mas-Aguilar, G. Brunelli, G. Ceribella, M. López Moya, R. López-Coto for the CTA-LST project. "First results of pulsar observations with the LST-1". In: *Proceedings of 38th International Cosmic Ray Conference — PoS(ICRC2023)*. Vol. 444. 2023, p. 569. DOI: 10.22323/1.444.0569.

[104] R. López-Coto. "Very-high-energy γ-ray observations of pulsar wind nebulae and cataclysmic variable stars with MAGIC and development of trigger systems for IACTs". Available at `https://link.springer.com/book/10.1007/978-3-319-44751-3`. PhD thesis. Universitat Autonoma de Barcelona, 2015.

Acknowledgements

What a journey this thesis was. If I told the September 2022 version of me about all the emotions she would experience after crossing thousands of kilometres from Bologna to Granada she would not believe me at all. If I told her she would dance to Spanish music for six hours straight at the Feria, probably she'd say "Over my dead body". Well, she was wrong.

During the months I spent at the Instituto de Astrofísica de Andalucía, I met amazing people who always made me feel welcome. I enjoyed every moment of it, even when I was cursing my notebooks for not working or when my skin was melting because of the summer heat. I will never forget how happy I felt when coming home from the Feria or the midnight swim on San Juan watching the fireworks and the pyre being lighted up. I will never forget all the smiles and nice words people offered me, making even my bad days a little bit better. I hope I can come back soon to the IAA.

So, the first, huge thanks goes to the VHEGA people: Rubén, Alba, Iván, Juan, Jorge, Daniel and Till. Thanks for including me in the group as I've always been part of it. Thanks for all the tapas Fridays to celebrate every single occasion or just to have fun at the end of the week. Thanks for the hikes and all the other experiences you've invited me to, you really are the best and funniest group of the IAA. I promise I will speak better Spanish the next time you'll see me.

Thanks to the people of office A343, Teresa, Julio and Miguel, for being the best colleagues I could ever get during my stay as a visitor. Together we took ~~very long~~ breaks during the daily work, discussing everything our minds came up with. I really longed for these moments after a day of work. I was honoured to get a special mention in your "out of context quotes" board.

The other two people who made my months in Granada unforgettable are Kat and Maëlle, my roomies of piso 6B. We had so much fun together trying new restaurants and walking around the city in our free time, all while speaking our best Spanglish. Being alone for two weeks after you left was a bit sad, the house felt so silent and empty without you. I wish you the best in your lives and careers and I hope to see you again in Spain, or wherever you want to meet the next time.

Durante questi mesi ho avuto la possibilità di entrare a far parte di CTA e ringrazio Roberta e Rubén per questa opportunità e per avermi permesso di crescere all'interno

del progetto. Non avrei mai pensato di arrivare fin qua, quindi grazie per tutto l'aiuto che mi avete dato e per tutte le cose che mi avete fatto scoprire. Ringrazio anche il prof. Vignali per la disponibilità e l'aiuto per la scrittura della tesi.

For all the work you did to help me, I thank Álvaro Mas Aguilar and Giovanni Ceribella. You introduced me to the VHE pulsars world and you were always available to spare some of your time for me when I needed help. This thesis wouldn't be here without you.

Grazie agli amici di sempre, nati tra le sezioni H e C del Copernico (e con estensioni nella bassa): Laura, Sara, Jack, Nico, Scanna, Cris, Reny e Dani. Ne è passato di tempo dalle prime serate di giochi di società a casa di Laura, quando ancora non avevamo imparato che il tavolo era di vetro e l'unica preoccupazione era essere a scuola il lunedì mattina alle otto. Grazie di tutte le serate passate insieme, dei viaggi e le partite infinite a Bang che nove volte su dieci rischiano di finire in rissa. Ricordate che la vostra babysitter Giulia è sempre pronta a starvi dietro durante le serate per non farvi volare nell'iperspazio.

Grazie ai fisici più Stroboscopici di via Irnerio 46: Sara, Eleonora, Cheps, Ste, Barbo, Tromba ed Elena. Non avendovi ringraziati per la triennale, devo farlo il doppio per la magistrale. Ci siamo incontrati tra le panche spaccaschiena dell'aula magna di fisica, dove abbiamo pianto sangue per gli esami e disegnato pallini, e abbiamo superato la triennale nonostante il covid e tutte le altre difficoltà del percorso. Quando ho iniziato la magistrale ho pensato spesso a quanto fosse strano non essere più tutti insieme a lezione, ma nonostante tutto siamo ancora qua. Grazie delle uscite, delle grigliate e di tutti i momenti passati insieme, sono stati fondamentali per superare questi cinque anni.

Grazie ai compagni di magistrale, con cui ho passato un anno e mezzo faticoso ma soddisfacente. Menzione speciale per Beppe, Giulia, Luca, Enrico, Matteo e Maicol, compagni di film e cene fuori. I momenti passati con voi sono stati parte integrante del percorso di studi e sono felice di avervi incontrati.

Ringrazio tutta la mia famiglia, mamma, papà, Mutti, i nonni e lo zio, sempre in prima linea a supportare le mie scelte di vita. Visto che il non avere un piano B a parte fare fisica all'università ha avuto il suo successo?

L'ultimo grazie va a te, Giacomo, che sei rimasto con me fino ad oggi, sopportandomi per tutti questi anni. Ne abbiamo superate tante insieme e non sempre è stato facile. Grazie per essere sempre rimasto al mio fianco, per accettarmi così come sono, tra pare mentali e tutto il resto, grazie per essere sempre paziente con me, anche quando divento insopportabile. Spero di continuare ad essere la tua *part-time soulmate and full-time problem* ancora per molto.